ENGINEERED DISSIPATION IN OPEN QUANTUM ACOUSTIC SYSTEMS

By

Joseph M. Kitzman

A DISSERTATION

Submitted to
Michigan State University
in partial fulfillment of the requirements
for the degree of

Physics—Doctor of Philosophy

2023

ABSTRACT

ENGINEERED DISSIPATION IN
OPEN QUANTUM ACOUSTIC SYSTEMS

By

Joseph M. Kitzman

Quantum acoustic systems, in which superconducting qubits are coupled to quantized mechanical degrees of freedom, offer a unique paradigm for the investigation of the fundamental properties of phonons as well as the development of quantum technologies based on phonons. This thesis presents several experiments that demonstrate the interaction between a superconducting transmon qubit and a high-frequency surface acoustic wave (SAW) resonator. We use classical modeling techniques to design the electrical conductance of the SAW resonator, which encode the spectral properties of the phononic modes hosted by the SAW device. These spectral features are then investigated by leveraging the extreme sensitivity of the qubit to its local environment, and highlight the complex mode structure of surface phonons in our experiments. Furthermore, by considering the full phononic density of states, we identify interference effects between resonant and lossy phonon modes, which act as the primary source of decoherence for the qubit. These phonons that are not confined within the SAW cavity act as an engineered dissipation channel which we use advantageously as a mechanism for the dynamical quantum state preparation and stabilization of high purity qubit states. The results of this thesis highlight the versatility of quantum acoustics systems in both the strong and weak coupling regimes, and emphasize the ability to engineer phononic interference and dissipation in the quantum regime.

ACKNOWLEDGMENTS

Throughout the course of graduate school, I have had the opportunity to work with many wonderful people. First and foremost, I would like to thank my advisor Johannes Pollanen for the vital role he has played in my scientific career. Johannes is a great scientist and has been an absolutely fantastic mentor, and I'm grateful to have had the opportunity to learn from him. Much of what I know about experimental physics can be attributed to the tremendous environment Johannes has worked to create at MSU. I'll remember our time working together very fondly. I would like to thank the remaining members of my committee: Mark Dykman, Morten Hjorth-Jensen, Shannon Nicley, and Jaideep Singh for their continued guidance and insight. Each of my committee meetings was a wonderful learning experience with many thought-provoking discussions.

I am also greatly appreciative of Dr. Justin Lane, who taught me the day-to-day skills I needed to be a scientist. Our times figuring stuff out in the lab, moving ladders around, and carefully soldering on the fridge are memories I will always treasure. Throughout the process of my Ph.D., I needed a lot of help from some really great colleagues. I would like to thank Dr. Heejun Byeon, Dr. Liangji Zhang, and Dr. Kostyantyn Nasyedkin for welcoming me into the group and helping me out whenever I had silly questions, which was pretty often. I would also like to thank the current members of our lab: Camille Mikolas, Austin Schleusner, Camryn Undershute, Jingyu Zhang, and Dr. Pranaya Rath, all of whom I am very lucky to call both friends and colleagues. Thank you to Dr. Niyaz Beysengulov for his friendship and guidance the entirety of my time as a graduate student. I'm lucky to have overlapped with some other great people in the physics department. To Eric Goodwin, Michael Gottschalk, Jacob Watkins, and many others- thanks for the great discussions over the years. You all

made graduate school an awesome experience. I also owe a special thanks to Kim Crosslan for keeping me sane when I needed a break from work and needed to chat, it was always much appreciated!

I have been extremely fortunate to collaborate with some excellent scientists outside of MSU. In particular, I owe a great deal of thanks to Prof. Kater Murch at Washington University in St. Louis. Kater is an expert in all things regarding superconducting qubits, and his willingness to answer any and all questions I could come up with really helped push forward the open quantum systems experiments in my thesis. Additionally, I would like to thank Dr. Patrick Harrington and Max Drimmer for helping me out when I had many questions about simulations.

I am thankful for the support of my parents Mark and Sandy Kitzman. None of this would have been possible without their encouragement to dream big. I'm grateful for everything that you guys have done for me for the past five (and more realistically 27) years. To Dawn and Darrell Slag, I will always be appreciative of your kind words and interest regarding my work.

Finally, I owe a great deal of thanks to my wife Dezi. Your unwavering encouragement and optimism regarding my research over the last five years has meant the world to me. From late night trips into the lab to check on the fridge, to listening to (*really* rough) first versions of all of my talks, I'm eternally grateful you have been by my side through it all. I truly couldn't have completed this long journey without your support. Thank you.

The projects described in this thesis were partially supported by the National Science Foundation via grant number ECCS-2142846 (CAREER) and the Cowen Family Endowment at MSU.

TABLE OF CONTENTS

Chapter 1

Applied and Fundamental Quantum Phononics with Superconducting Qubits

1.1 Introduction

Vibrational excitations are often first introduced via one-dimensional (1D) toy models of masses connected by springs [1]. These toy models are often presented in an entirely classical context and do not offer insight into the world of quantum mechanics. When treated quantum mechanically, many mechanical oscillations have a harmonic response, meaning that they can be mapped onto a simple quantum harmonic oscillator. However, experimental implementation of simple harmonic oscillators typically does not allow for the study of highly quantum mechanical states of the oscillator such as squeezed states or states with negative Wigner functions [2–4]. Since all the transitions in a harmonic oscillator have the same energy (frequency), classical drive signals to the system simultaneously drive every transition within the oscillator, leading to a coherent state [5]. In order to truly access the quantum nature of a mechanical system, it is often useful to introduce the concept of a *hybrid system*, in which two (or more) quantum systems are coupled together [6, 7]. In this

thesis, we show that by engineering the interaction between a quantum two level system (in our case a superconducting qubit) and a mechanical harmonic oscillator in a framework often called *quantum acoustics* [8, 9], it is possible to investigate mechanical excitations in the quantum limit. Quantum acoustics largely borrows from the field of circuit quantum electrodynamics (cQED) [10, 11] to engineer strong coupling between the qubit and bosonic modes of the mechanical oscillator [12], as well as infer properties of the mechanical oscillator via measurements of the qubit [13] (see Fig. 1.1). In particular, this thesis focuses

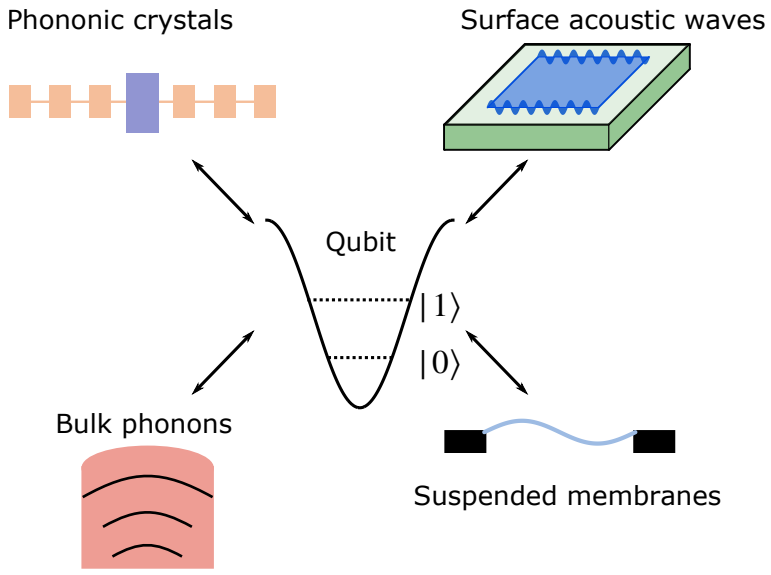

Figure 1.1: Schematic of various quantum acoustics architectures. As described in the main text, a superconducting qubit (center) is used as a tool for investigating the quantum mechanical behavior of phononic systems such as surface acoustic waves, bulk phonons, phononic crystal resonators, and suspended membranes, just to name a few.

on quantum acoustics systems based on elastic waves propagating along the surface of a piezoelectric crystal, called surface acoustic waves (SAWs), which have many exciting applications within quantum acoustics [14–16] and beyond [17–19]. This chapter will focus on introducing quantum acoustic systems with a broad broad perspective on the potential applications involving the integration of phonons with quantum information systems as well as

fundamental physics results within the field of quantum acoustics. The chapters that follow will introduce the necessary background information for cQED systems and qubits (chapters 2 and 3), SAWs (chapter 4), and open quantum systems (chapter 5) before presenting the main experimental results on engineered open quantum acoustics systems (chapter 6) [15] as well as measurement of the interference of surface phonons via the absorption spectrum of a superconducting qubit (chapter 7) [16].

1.2 Transduction and transmission of quantum information with mechanical excitations

Mechanical excitations can potentially be used in quantum memory schemes [20, 21], quantum information can be imprinted on the phononic transmission of a SAW resonator [22, 23], itinerant phonons can be used to communicate between spatially dislocated qubits [24–26], and phononic resonators are a vital part of many proposed microwave-to-optical transduction protocols [27]. In this section, the latter two examples associated with quantum communication using phonons will be described in detail.

Phonons can be leveraged as a useful means to store or transduce quantum information in several different ways. In order to use phonons as a direct means of quantum communication, it is important to engineer quantum circuits to create single-phonon excitations to maintain the quantum nature of a given qubit state. If one were to create a qubit state with a well-defined phase (i.e. a superposition state), the conversion of this quantum state to a classical mechanical state would destroy the relevant phase information of the qubit. The continued advancement of superconducting circuits has enabled the development of quantum

acoustics systems to experimentally realize a single phonon Fock state [4,28] able to preserve this phase information. By engineering a quantum acoustics system in which single surface phonons can be realized, these itinerant excitations can carry quantum information from one point to another. In fact, phase information of the state of a superconducting qubit can be transmitted via these tinerant surface phonons, and has been shown to enable to the creation of two-qubit Bell states mediated by SAW phonons [24]. Furthermore, the interference of quantum information encoded in these phonons can be leveraged to implement quantum erasure experiments and perform "which path" measurements using phonons [29]. By further optimizing the phononic communication channel, the excitations can be unidirectionally excited and used to preform interferometric measurements of superconducting qubits [25, 30]. Additionally, phononic beamsplitters have recently been introduced into multi-qubit experiments and allows quantum acoustics architectures with direct comparisons to linear optical quantum computing protocols [26]. Although experimental progress using itinerant phonons as carriers of quantum information has been successful thus far, it remains to be seen if acoustic losses can be sufficiently reduced to scale linear quantum acoustics-based processors to large qubit number.

Even if phonons are not used as direct carriers of quantum information, they are still useful in other potential quantum computing applications by enabling certain microwave to optical transduction schemes. Quantum state transduction is important for a multitude of reasons, including protecting quantum signals from thermal noise, as well as the inclusion of low-loss optical fibers to preserve the integrity of the transmitted quantum signal over kilometer scale distances [31]. For example, nanomechanical transducers and resonators have been implemented to couple optical photons and microwave signals via piezoelectric optomechanical crystals, achieving coherent signal transfer between microwave and optical fields [32–34].

It has been shown that integrating optomechanical systems thermally cooled to near their quantum ground state allows for bi-directional transduction with minimal added noise to the quantum signal [35,36]. Even when the mechanical system of interest is not cooled to near its ground state, it is still possible to engineer highly efficient transduction schemes (near 47% conversion efficiency) while maintaining minimal optomechanical backaction [27,37–39]. The integration of optical-based readout and state transfer with superconducting circuits represents an important milestone for integrated quantum networks, with further experimental implementation of multi-qubit processors interconnected via optical signals as the next important step.

1.3 Generation of non-classical phononic states

Mechanical systems are often physically macroscopic and able to host a large number of excitations opening the door for potential applications in quantum information processing, high-precision sensing, and metrology. By coupling these macroscopic phononic systems to superconducting circuits in the quantum regime, it is possible to investigate their quantum mechanical properties and attempt to realize these potential applications. Typically, mechanical oscillators are linear in nature, making them difficult to operate with a well-defined number of excitations. However, other linear systems, such as electromagnetic resonators, have been successfully operated in the so-called "quantum regime", where quantum mechanical states of these resonators have been initialized and measured by introducing a Josephson junction as an effective non-linear circuit element [40, 41]. In face, these efforts were an important step to understanding the quantum mechanical properties of microwave photons. This section aims to outline recent progress toward creating truly quantum mechanical states

of vibrational excitations in analogy to the progress made using microwave photons.

The first step for the quantum operation of a mechanical resonator is to prepare a known oscillator state. The simplest well-known state we can imagine making is the quantum ground state of the oscillator. If the energy required to excite the oscillator is much higher than the ambient thermal energy of the local environment, the oscillator will be passively cooled to near its quantum ground state by the shear fact that it is in thermal equilibrium with its environment. In particular, it has been shown that under these conditions it is possible to passively cool a mechanical resonator to low excitation number and measure the quantum mechanical depolarization and decoherence times of a single phonon by interfacing the resonator with a superconducting qubit [42]. In contrast to these high-frequency oscillators, mechanical resonators with a transition energy compared to the thermal energy of their local environment can also be initialized to well-defined quantum states via protocols such as laser cooling [43], sideband cooling [44], and thermal cooling enabled by quantum reservoirs [45]. Additionally, linear low-frequency optomechanical systems have also been cooled passively using nuclear demagnetization [46].

Oftentimes, engineering the coupling of these mechanical degrees of freedom with other quantum systems provides additional experimental tools with which to control the phononic system. In particular, quantum control of phonons has been shown by coupling a mechanical harmonic oscillator to optical cavity modes [47,48] as well as superconducting qubits [4,28], which is the hybrid system of interest for the remainder of this section. These optimized hybrid systems open up the possibility of resolving and characterizing quantized phononic states that can be leveraged for the full quantum control of mechanical systems. When the hybrid system enters the regime where the coupling rate between the qubit and the oscillator exceeds the decoherence rate of either system (the so-called *strong coupling regime*), quan-

tum states can be coherently transferred between the qubit and the mechanical oscillator. Since superconducting qubits are sensitive to electrical excitations, hybrid quantum acoustics systems often rely on piezoelectric materials, which enable to conversion from electrical energy to vibrational energy, and vice versa. Using hybrid systems based on piezoelectric materials, single phonon Fock states can be prepared and measured in phononic resonators based on bulk phonons [3,28], mechanical waves on the surface of piezoelectric materials [4], and engineered phononic crystals [49, 50].

Recently, quantum phenomena such as entangled states of mechanical oscillators and Schrödinger cat states of motion in relatively massive mechanical oscillators have been of great interest, due to their potential applications in quantum information processing. By using a superconducting qubit that is simultaneously coupled to two separate phononic crystal resonators the qubit can be used as a tool to create a Bell state between the two mechanical resonators [50]. This operation opens the door for bosonic quantum computing using phononic degrees of freedom [51]. Via tomographic reconstruction of the joint phonon distribution between the mechanical oscillators, it can be shown that the inclusion of superconducting qubits in mechanical system enables deterministic control of multiple bosonic degrees of freedom in potential quantum processors [50].

In quantum acoustics architectures based on *bulk* phonons, it has been shown that it is possible to create superpositions of phononic coherent states with definite phase difference [52]. Physically, this type of quantum state corresponds to atomic lattice oscillations within the bulk of the material having opposite phases. In order to engineer precise phase and amplitude control over these Schrödinger cat states it is necessary to couple the phonon modes of interest to a superconducting qubit and leverage the resonant regime of the Jaynes-Cummings Hamiltonian [53, 54], in contrast to most systems that are typically operated in

dispersive regime [10, 11]. The generation of phononic cat states represents a massive advance in the fundamental understanding of phononic modes at the quantum level as well as important potential applications in quantum information processing, for example using these bosonic modes themselves as a qubit [55].

1.4 Phononic sensing

A key ingredient in the previous section was the use of qubit measurement to gain information about the state of the mechanical oscillator, which was made possible due to a designed interaction between a qubit and the mechanics. In contrast, the aim of this section is to focus on using information about the oscillator state to gain information about the local phononic environment. In order to provide context for the interaction between the qubit and mechanics, we will discuss the *dispersive interaction* between the two modes [10, 11]. When the frequency difference (Δ) between the qubit frequency and mechanical resonator frequency is large relative to their coupling ($g \ll \Delta$), the Jaynes-Cummings Hamiltonian takes dispersive the form:

$$H \approx \omega_m \hat{m}^\dagger \hat{m} + (\omega_{01} + 2\chi)\hat{\sigma}_z/2, \tag{1.1}$$

where ω_m is the frequency of the mechanical oscillator, with creation (annihilation) operator $\hat{m}^\dagger$ ($\hat{m}$), and ω_{01} is the qubit frequency, which acquires a dispersive shift of 2χ for each occupied level of the mechanical resonator. This dispersive shift is due to the ac-Stark effect and has been widely observed in cQED systems [56], where the qubit acquires a frequency shift that depends on the number of photons in a microwave resonator. More recently, this

effect has been observed in cQAD systems [3, 16, 28, 49, 57], as the population of phononic modes modifies the qubit absorption spectrum in accordance with Eqn. 1.1.

In the strong dispersive regime, the frequency shift imparted on the qubit per excitation is larger than both the qubit and resonator's decay rate. This allows for the precise determination of the resonator's state, i.e. its statistical distribution over the phononic Fock basis. An important feature of this dispersive readout technique is that the measurement Hamiltonian commutes with the resonator's operators, allowing for quantum non-demolition (QND) measurements of the mechanical resonator. Not only are QND measurements interesting from a fundamental physics perspective, as they allows one to gain information about a quantum state without destroying it, but QND measurements are also essential to most quantum error correction (QEC) schemes [58].

Since the first experimental demonstration of the strong dispersive regime in cQAD [49, 57], dispersive readout has proven to be a powerful experimental tool to sense the phononic environment coupled to the qubit. Dispersive readout techniques have been combined with classical drives for quantum phononic state preparation techniques (as discussed in the last section of this chapter) to perform Wigner tomography of a mechanical resonator [3, 50, 59]. In other experiments, a superconducting qubit was tuned to simultaneously be in the strong dispersive regime with two mechanical resonators. This allowed for the qubit to act as a sensor for both resonators simultaneously and was recently demonstrated to dispersively readout entanglement between the two mechanical oscillators [50]. Even in the situation where the qubit or mechanical resonator decoherence is larger than the dispersive shift (the *weak* dispersive regime), we can still rely on the qubit to sense its phononic environment. For instance, this was recently leveraged to measure a phononic Fano resonance [60, 61], where a single, strongly resonant mode of a phononic resonator interferes with a continuum of lossier

phononic modes of the same resonator resulting in a characteristically asymmetric phonon spectrum [16]. The latter results are discussed in chapter 7 of this thesis.

Two-level systems (TLSs) introduce an additional source of environmental decoherence for qubits and mechanical resonators [62, 63]. Like any resonant system coupled to its surroundings, a TLS can decay into the larger environment via phononic channels. While TLSs can in some cases have longer coherence times than that of a qubit or mechanical system [64, 65], a lack of control over TLS properties limits easy investigation of TLSs in an experimental setting [66, 67]. Nevertheless, a more complete understanding of the emergence and decay of TLSs can provide insight into minimizing decoherence of future resonant systems and remains a topic of active research. Specifically, integrating superconducting qubits with mechanical resonators has been shown to provide a promising means for investigating the decay of phonons into a bath of resonant, or near resonant TLSs [68].

1.5 Quantum simulation with open quantum acoustics

Physical quantum systems that are capable of simulating complicated phenomena dictated by quantum mechanics are referred to as *quantum simulators* [69, 70]. Advances in the scaling of quantum devices and engineered systems has produced significant growth in the development of quantum simulators, based on a wide variety of different quantum systems [71]. Quantum acoustic devices are a novel platform for quantum simulation, particularly in the simulation of non-Markovian and open quantum systems, which are never truly isolated from their environments. Oftentimes, the environment or "bath" is an unwanted source of decoherence for the quantum system of interest. In simple cases, open quantum systems can be modeled via the Markovian master equation [72], however, if the system exhibits finite memory effects,

a modified non-Markovian master equation is needed to model the system dynamics [73, 74]. These types of memory effects have been both predicted and observed in cQED systems [75–77] and are now under investigation in cQAD systems. Because phonons travel significantly slower than photons (approximately 5 orders of magnitude slower at the same frequency), quantum acoustics systems are an ideal platform for studying open quantum systems with memory effects. By coupling a mechanical system to a superconducting qubit over relatively large distances, it has been predicted, and verified experimentally, that non-Markovian effects can dominate the evolution of a superconducting qubit [78, 79]. Extensions of experiments that couple superconducting qubits to mechanical resonators in a regime in which the finite memory effects of the bath are a dominant effect open the door to non-Markovian bath engineering. By engineering the Hamiltonian in such a way, it could be possible to fully investigate the impact of phonon transit time and interference, at the level of single phonons, on qubit dynamics. The flexibility of quantum acoustics systems in this regard offer a very exciting avenue for the fundamental investigation of non-Markovian systems.

In addition to the ability to tailor the Hamiltonian of quantum acoustics systems, hybrid quantum phononic systems also offer the ability to control the dissipation of a superconducting qubit with a high level of precision using the spectral properties of the phononic resonator [4, 15]. Well developed cQED theories about noise, amplification, and measurement [80] have allowed for breakthroughs in dissipation engineering with superconducting qubits coupled to their electromagnetic environment. It has been shown that coupling a transmon qubit to a frequency dependent impedance allows for the control of the dissipation experienced by the qubit [81]. Designed dissipation engineering in the field of cQED has proven to elucidate the understanding of the light-matter interaction in superconducting circuits [82–90]. By leveraging controlled dissipation, it has been shown that it is possible

to create systems in which effective non-Hermiatian systems can be simulated using cQED architectures [91–94].

By coupling a superconducting qubit to an effective electrical impedance produced by a mechanical resonator, it is possible to implement an effective frequency dependent loss channel that dictates the decay of a transmon qubit [95]. This enables experiments utilizing engineered *phononic* dissipation channels to simulate open quantum acoustics systems to produce dissipative state preparation and dynamical state stabilization [15], as will be discussed in chapter 6. By continuing to optimize the designed dissipation experienced by the qubit via its coupling to a phononic bath, future experiments could be used to control the dissipation of higher transmon levels. By implementing a system in which different qubit levels have vastly different loss rates, it could be possible to create an effective two-level system with decay out of the qubit manifold, allowing for the simulation of an effective non-Hermitian [96] open quantum acoustics system. Combining the ability to design both the loss spectrum and the Hamiltonian to a high degree of precision in quantum acoustics systems makes these qubit-phonon hybrid systems an ideal playground for understanding both superconducting circuits and vibrational excitations in the quantum regime.

1.6 Conclusion

This chapter has served as a broad introduction on the current state of play in the field of quantum acoustics. Engineered phononic degrees of freedom can be used to transit quantum information via itinerant phonons, or phonons can be used as an intermediary to enable microwave-to-optical transduction schemes. When coupled to nonlinear elements such as superconducting qubits, the phononic degrees of freedom can be controlled at the level of

single phonons. This quantum control can be used to generate highly non-classical phononic states including Fock states, entangled states, and Schrödinger cat states. Additionally, the coupling to the qubit can be designed such that the oscillator's excitation spectrum can be imparted onto the qubit, allowing for the sensing of phononic decay or interference. Finally, due to the ability to fine-tune the interaction between the qubit and the mechanical modes as well as the phononic excitation spectra, the field of quantum acoustics is an ideal candidate for quantum simulation of both non-Markovian and open quantum systems, and the results presented in this thesis break the foundational ground in this effort.

Chapter 2

Superconducting Quantum Circuits

Interfacing high-frequency mechanical resonators cooled to their quantum ground state with quantum circuits offers an exciting platform for quantum memory applications [20], linear quantum computing [26], as well as quantum communication enabled via phonons [24, 25]. In order to operate these phononic modes in the quantum regime, we rely on the framework of circuit quantum acoustodynamics (cQAD) [8], an analogue of circuit quantum electrodynamics (cQED) [10, 11]. Furthermore, cQED also provides a means with which to both manipulate and measure the state of our qubits. This chapter aims to develop the necessary theoretical background for cQED systems, with important analogues to cQAD systems. The topics discussed in this chapter provide the background knowledge for engineering the interaction between quantum two-level systems and bosonic degrees of freedom (either *photonic* or *phononic* depending on the experiment).

2.1 Quantization of the LC oscillator

A quantum two-level system, or *qubit*, is an integral component for the results of this thesis. In this chapter, we will build an understanding of how we can experimentally realize such a quantum system and how we can manipulate and measure the state of this system. Additionally, analogs of these techniques will become increasingly important for the experiments described in chapters 6 and 7 when we consider a qubit strongly coupled to various types of

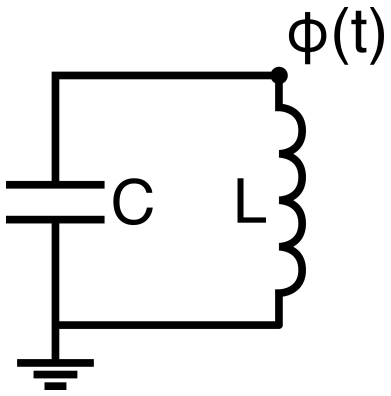

Figure 2.1: A parallel LC circuit. The node flux $\phi(t)$ is defined relative to ground. In this simple circuit, the energy oscillates between the electric and magnetic fields.

mechanical excitations.

A simple resonating electrical circuit one can imagine constructing in a laboratory consists of a parallel LC circuit where the stored energy in the circuit oscillates between charge imbalance across the capacitor and currents passing through the inductor. An example of a circuit can be seen in Fig. 2.1. In order to investigate how energy is stored in the circuit, we begin by constructing the Lagrangian of the circuit as defined by the node fluxes in the system as shown in Fig. 2.1.

$$\phi(t) = \int_{-\infty}^{t} V(t')dt' \tag{2.1}$$

In Eq. 2.1, $V(t')$ represents the voltage relative to ground at the node at time t'. We can use fundamental circuit relations to see that the voltage across the inductor is given by $V = L\dot{I}$, which allows us to write the node flux as a function of the current through the inductor, $\phi = LI$. The energy stored in the inductor can then be written in terms of the node flux rather than in terms of the current:

$$E_L = \frac{1}{2}LI^2 = \frac{\phi^2}{2L}. \tag{2.2}$$

Similarly, by expressing the voltage across the capacitor in terms of the time derivative of the node flux ($V = \dot{\phi}$), we can write the energy stored across the capacitor plates as:

$$E_C = \frac{1}{2}CV^2 = \frac{1}{2}C\dot{\phi}^2. \tag{2.3}$$

Having expressed the energy stored in each component of the circuit, we can identify the node flux as an effective coordinate in a Lagrangian treatment of the problem. In this framework, we can think of the energy stored in the inductor as an effective *potential* energy (the energy only depends on the effective coordinate ϕ), and the energy stored across the capacitor pads as an effective *kinetic* energy (this energy depends on the time derivative of the coordinate, and therefore resembles a velocity!). With this analogue in mind, we can construct the Lagrangian $\mathcal{L}$ for the circuit:

$$\mathcal{L} = E_C - E_L = \frac{1}{2}C\dot{\phi}^2 - \frac{\phi^2}{2L}. \tag{2.4}$$

In order to investigate the energy spectrum of this system, it is necessary to carry out a Legendre transformation of Eq. 2.4 to obtain the Hamiltonian. It is then important to recall that the Lagrangian is a function of both position and velocity ($\mathcal{L} = \mathcal{L}(q, \dot{q})$), while the Hamiltonian is a function of coordinate and momentum ($\mathcal{H} = \mathcal{H}(q, p)$). The conjugate momentum to the coordinate ϕ is then calculated as

$$p = \frac{\partial \mathcal{L}}{\partial \dot{\phi}} = C\dot{\phi} = CV, \tag{2.5}$$

where we immediately recognize the conjugate momentum as just the charge stored across the capacitor pads $Q = CV$. As such, we will refer to this stored charge across the capacitor pads

interchangeably with the momentum for this particular circuit. Having correctly determined the conjugate momentum for the LC oscillator, we can now calculate the Hamiltonian:

$$\mathcal{H} = \dot{\phi}\frac{\partial \mathcal{L}}{\partial \dot{\phi}} - \mathcal{L} = \frac{1}{2}C\dot{\phi}^2 + \frac{\phi^2}{2L}. \tag{2.6}$$

Remembering to express the Hamiltonian as a function of the momentum Q rather than the "velocity" $\dot{\phi}$, we arrive at our final expression for the classical Hamiltonian of the LC oscillator:

$$\mathcal{H} = \frac{Q^2}{2C} + \frac{\phi^2}{2L}. \tag{2.7}$$

Importantly, Eq. 2.7 is quadratic in both the momentum and coordinate. As such, it is reasonable to expect a response from the system resembling that of a harmonic oscillator. Recalling that the resonant frequency for a simple LC oscillator is given by $\omega = 1/\sqrt{LC}$, we can re-express Eq. 2.7 as

$$\mathcal{H} = \frac{Q^2}{2C} + \frac{1}{2}C\omega^2\phi^2. \tag{2.8}$$

As seen above, this Hamiltonian is reminiscent of a standard harmonic oscillator, with the capacitance serving as a substitute for the mass.

2.2 Quantum mechanical circuits

Since our experiments ultimately require quantum mechanical circuits, an important extension of the analysis involves promoting the variables representing charge and flux in the previous section to quantum operators rather than classical variables. Since the charge was found to be the conjugate momentum to the "position" ϕ, once the continuous variables are promoted to quantum mechanical operators, they will inherit the canonical commutation

relation $[\hat{\phi}, \hat{Q}] = i\hbar$. Because we found that the classical LC oscillator exhibited harmonic response, it is natural to express the quantum mechanical operators as linear combination of harmonic oscillator ladder operators $\hat{a}$ and $\hat{a}^\dagger$. Including prefactors that represent the quantum mechanical fluctuations of both charge and phase, the operators become:

$$\begin{aligned} \hat{\phi} &= \phi_{\text{ZPF}} \left(\hat{a} + \hat{a}^\dagger \right) \\ \hat{Q} &= -iQ_{\text{ZPF}} \left(\hat{a} - \hat{a}^\dagger \right) ., \end{aligned} \tag{2.9}$$

where the ladder operators maintain the fundamental commutation relation $[\hat{a}^\dagger, \hat{a}] = 1$. Furthermore, we can express the quantized Hamiltonian in terms of these new ladder operators as

$$\hat{\mathcal{H}} = \hbar\omega \left(\hat{a}^\dagger \hat{a} + \frac{1}{2} \right). \tag{2.10}$$

Additionally, we assume that the zero point fluctuations of both charge and phase are given by the expressions which depend on the characteristic impedance of the oscillator $Z_0 = \sqrt{L/C}$:

$$\begin{aligned} \phi_{\text{ZPF}} &= \sqrt{\frac{\hbar Z_0}{2}} \\ Q_{\text{ZPF}} &= \sqrt{\frac{\hbar}{2Z_0}}. \end{aligned} \tag{2.11}$$

What does all of this analysis tell us? Although we have carried out an thorough investigation of a simple electromagnetic resonator, this system does *not* function as a two-level system, but rather it is a system with infinitely many evenly spaced energy levels $\Delta E = \hbar\omega$, where $\omega = 1/\sqrt{LC}$. However, this analysis has allowed us to learn how to quantize simple circuits (a detailed description of more complex circuits can be found in Ref. [97]). The following

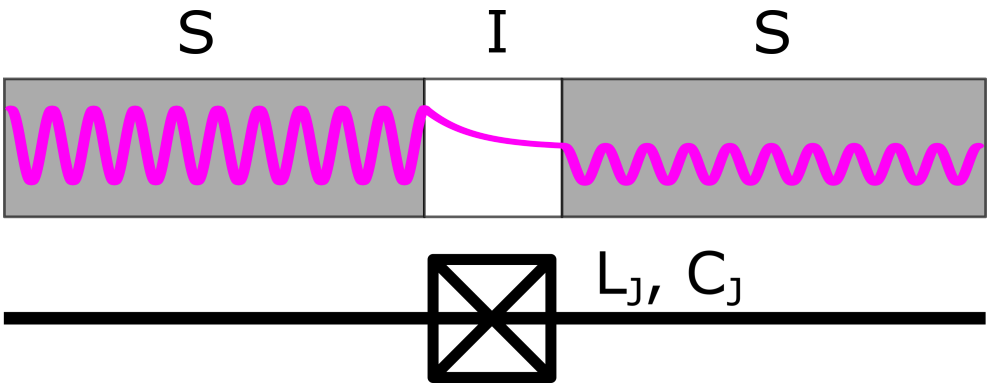

Figure 2.2: Top: Schematic of a Josephson junction. Two superconducting islands (grey; S) are separated by a thin insulating layer (white; I). Cooper pairs can tunnel across the junction through the insulator. Bottom: Circuit representation of a Josephson junction. The junction responds as a nonlinear inductor with inductance L_J. There is some intrinsic capacitance C_J associated with the insulating layer that is represented by the box surrounding the cross.

section will introduce a modification to the circuit described above and will introduce the necessary non-linearity needed to create a well-defined quantum two-level system, which turns out to be relatively straightforward to implement experimentally.

2.3 Superconducting qubits

In order to create the required non-linearity into our circuits so that we can independently address any two individual energy levels, we require the incorporation of a *Josephson junction* [98, 99]. As will be shown in this section, for the experiments relevant to this thesis, a Josephson junction can be effectively thought of as an inductor with a non-linear voltage response to a time-varying current. This non-linearity will be a key building block necessary in our experiments. A Josephson junction consists of two superconducting islands that are separated by a thin insulating layer as shown in Fig. 2.2. The superconducting charge carriers (called *Cooper pairs*) can tunnel across this thin layer, weakly connecting the two superconducting islands. The superconducting state at any position $\vec{r}$ in the material can

be described by an order parameter $\psi(\vec{r}) = \sqrt{n_p}\,\exp[i\phi(\vec{r})]$. The density of Cooper pairs is represented by n_p, and the phase of the order parameter is $\phi(\vec{r})$. In a Josephson junction, the superconducting order parameter will have phases ϕ_L and ϕ_R in the left and right superconductors, respectively, as shown in Fig. 2.2. The famous result of Josephson [98] relates the difference in phase ($\phi \equiv \phi_L - \phi_R$) between the two superconductors to the current flowing through the junction:

$$I = I_c \sin\phi, \tag{2.12}$$

where I_c is the *critical current* of the junction, which is defined as the maximum superconducting current the junction can support before the superconducting state is destroyed. If a constant voltage is applied across the junction, the phase difference takes on a time dependence given by:

$$\frac{d\phi}{dt} = \frac{2eV}{\hbar}. \tag{2.13}$$

Together, Eqns. 2.12 and 2.13, form the so-called *Josephson relations*. Up to this point, the Josephson junction was promised to be important due to its nonlinear inductance, which we can obtain from these equations. We can calculate the inductance of a Josephson junction by taking the time derivative of Eqn. 2.12:

$$\dot{I} = \dot{\phi} I_c \cos\phi, \tag{2.14}$$

which can then be related to the voltage across the junction via $V = L\dot{I}$. Combining Eqns. 2.13 and Eqns. 2.14 allows us to solve for the phase-dependent inductance

$$L(\phi) = \frac{L_J}{\cos\phi}, \tag{2.15}$$

where we have introduced the magnetic flux quantum $\Phi_0 = \frac{\hbar}{2e}$ and the characteristic Josephson inductance $L_J = \frac{\Phi_0}{2\pi I_c}$. Eqn. 2.15 has a nonlinear dependence on the phase difference across the junction (and therefore the current flowing through the junction). Often, we operate devices consisting of two Josephson junctions in parallel. This particular device geometry is referred to as a DC Superconducting QUantum Interference Device (SQUID). If the two junctions have the same critical current I_c, the effective critical current of the entire loop is found to be [100]:

$$I_{c,\text{loop}} = 2I_c \cos \frac{\pi \Phi_{\text{ext}}}{\Phi_0}, \tag{2.16}$$

where Φ_{ext} is the applied external magnetic flux threading the loop (see Fig. 2.3). As we will see in the following sections, this means that by applying an external flux through a SQUID loop will allow us to tune the resonant frequency of our qubits. If the SQUID loop consists of two junctions whose critical currents are not identical (as is typically the case in realistic devices), the effective critical current of the loop is:

$$I_{c,\text{loop}} = (I_1 + I_2) \cos \frac{\pi \Phi_{\text{ext}}}{\Phi_0} \sqrt{1 + a^2 \left(\tan \frac{\pi \Phi_{\text{ext}}}{\Phi_0} \right)^2}, \tag{2.17}$$

where I_1 and I_2 are the critical currents of each junction in the loop, and $a = \frac{I_1 - I_2}{I_1 + I_2}$ is the parameter that quantifies the asymmetry in the critical currents between the junctions in the loop.

At this point, it will be extremely useful to consider what kind of Hamiltonian will describe a Josephson junction. As the phase ϕ across the junction changes in time, the change in the junction energy is given by the integral of the electrical power dissipated in

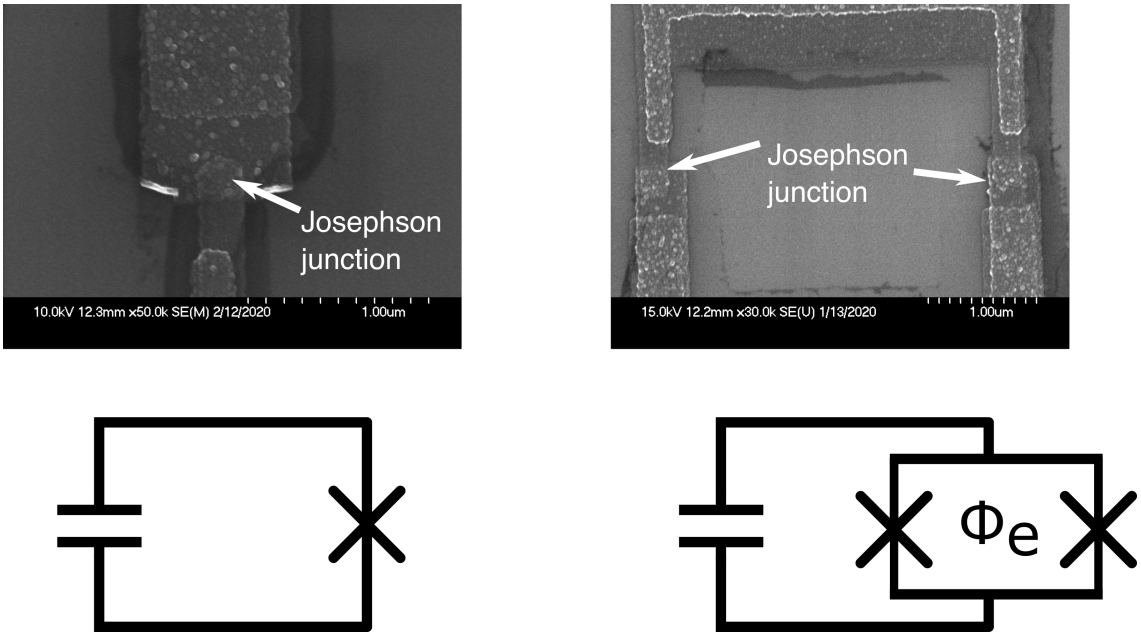

Figure 2.3: Top left: Transmon qubit with a single Josephson junction. The equivalent circuit is pictured below. As we will describe later in this thesis, much of the capacitance is comes from the large dipole antennae attached to our qubits. Top right: Transmon qubit in a SQUID geometry. The area of this particular loop is 16 μm^2. An external magnetic field can thread the loop and vary the effective critical current of the device. The equivalent circuit is pictured below.

the junction over time [100]:

$$\Delta E = \int I(t)V(t)\mathrm{dt}, \tag{2.18}$$

Where the current flowing through the junction is I and the voltage across the junction is V. The integrand of Eqn. 2.18 may be related to the flux Φ by the relation $Vdt = d\Phi$, and the flux may be related to the phase ϕ by $\Phi = \frac{\phi}{2\pi}\Phi_0$. By substituting these relations into Eqn. 2.18, and using the Josephson relation for the current (Eqn. 2.12), the junction energy

can be determined as follows:

$$\begin{aligned}\Delta E &= \int I_c \sin\phi \ \mathrm{d}\left(\Phi_0 \frac{\phi}{2\pi}\right) \\ &= \frac{I_c \Phi_0}{2\pi} \int \sin\phi \ \mathrm{d}\phi \\ &= -\frac{I_c \Phi_0}{2\pi} \ \cos\phi.\end{aligned} \tag{2.19}$$

In order to simplify the expression for ΔE, we introduce the Josephson energy, $E_J = \frac{I_c \Phi_0}{2\pi}$, which depends on the critical current of the junction, and is therefore tunable with an external flux in the case of a SQUID loop. This allows us to express the change in the junction energy as a function of phase:

$$E(\phi) = -E_J \ \cos\phi. \tag{2.20}$$

In addition to the tunneling of Cooper pairs through the junction, a full description of the system also involves taking into account the electrostatic potential energy due to the imbalance of Cooper pairs on either superconducting island, which is given by n. This electrostatic energy can be written in terms of the Cooper pair number operator $\hat{n}$ [101]:

$$\hat{U}_{ES} = 4E_c \left(\hat{n} - n_g\right)^2, \tag{2.21}$$

where the total capactive charging energy E_c depends on the intrinsic capacitance of the junction C_J as well as an external shunting capacitance C_S as $E_c = \frac{e^2}{2C_T}$, and the total capacitance is $C_T = C_S + C_J$. The parameter n_g represents the effect of an electric field bias to the system, and can be used to tune the parameters of the system via an external

gate. Alternatively, n_g can represent spurious coupling to the local electrostatic environment near (or within) the junction. Putting Eqns. 2.20 and 2.21 together, we arrive at the total Hamiltonian for the system as:

$$\hat{\mathcal{H}} = 4E_c \left(\hat{n} - n_g\right)^2 - E_J \cos\hat{\phi}. \tag{2.22}$$

Equation 2.22 describes a circuit known as the *Cooper pair box*. Early generation qubit devices were based on the Cooper pair box in a parameter regime where $E_J \sim E_c$. However, in this regime unwanted fluctuations in the offset charge n_g lead to significant fluctuation in the energy spectrum of the system, making these circuits somewhat difficult to work with experimentally [12, 56, 102]. To avoid these issues, a seminal theoretical work in the field of superconducting qubits explored the parameter range $E_J \gg E_c$, and found that this parameter regime largely protects the energy spectrum of the qubit from fluctuations in n_g [103]. This range of device parameters is referred to as the *transmon regime* and devices within this parameter range of E_J and E_c are called transmon qubits. The transmon qubit is the workhorse of the results of this thesis and is currently one of the most promising qubits for modern superconducting qubit architectures [104–108].

2.3.1 Aside: alternative derivation of Josephson energy

In this subsection, we present an alternative derivation of the Josephson energy that does not use the Josephson relations, but rather begins with a phenomenological Hamiltonian describing the tunneling of Cooper pairs through the junction, leading to the same result as Eqn. 2.20. This derivation is presented in full detail in Ref. [109].

Consider a Josephson junction as in Fig. 2.2. If the left superconductor has n_L Cooper

pairs and the right superconductor was n_R Cooper pairs, we can consider the *difference* $n \equiv n_L - n_R$ in Cooper pair number across the junction. Rather than associating the state of the system with a definite number of Cooper pairs on either superconducting island, we can think of a state $|n\rangle$ that only depends on the Cooper pair difference n. The number operator for this state can then be written as:

$$\hat{n} = \sum_{n=-\infty}^{n=\infty} n \left|n\right\rangle \left\langle n\right|, \tag{2.23}$$

which acts on number states as $\hat{n}\left|m\right\rangle = m\left|m\right\rangle$. Then, if a Cooper pair tunnels from the right side of the junction to left, the state $|n-1\rangle$ becomes $|n\rangle$, since n_L has increased by one. The inverse process (tunneling left to right) similarly brings the state $|n\rangle$ to $|n-1\rangle$. If both tunneling events occur with the same probability, we can write down the Hamiltonian for these processes as:

$$\hat{\mathcal{H}} = -\frac{E_J}{2} \sum_{n=-\infty}^{n=\infty} \left(\left|n-1\right\rangle \left\langle n\right| + \left|n\right\rangle \left\langle n-1\right|\right), \tag{2.24}$$

where the energetic cost for a tunneling event to occur is the Josephson energy E_J. We note that Eqn. 2.24 resembles a nearest-neighbor hopping interaction between the states $|n\rangle$ and $|n-1\rangle$.

Alternatively, rather than working with the Hamiltonian in the charge basis (consisting of the states $|n\rangle$), it is useful to introduce a new basis of states (the so-called *phase basis*). States in this basis are related to the states $|n\rangle$ by:

$$\left|\phi\right\rangle = \sum_{n=-\infty}^{n=\infty} e^{in\phi} \left|n\right\rangle. \tag{2.25}$$

Conversely, the charge basis states are related to the phase basis states via the continuous Fourier transform:

$$|n\rangle = \frac{1}{2\pi}\int_0^{2\pi} \mathrm{d}\phi e^{-in\phi}\,|\phi\rangle\,. \tag{2.26}$$

Inserting Eqn. 2.26 into Eqn. 2.24 and identifying the integral representation of the Kroneker delta function: $\delta_{\theta,\theta'} = \frac{1}{2\pi}\int_0^{2\pi}\exp[i(\theta-\theta')x]\mathrm{d}x$, we can express Eqn. 2.24 in the phase basis:

$$\hat{\mathcal{H}} = -\frac{E_J}{2}\frac{1}{2\pi}\int_0^{2\pi}\mathrm{d}\phi\left(e^{i\phi}+e^{-i\phi}\right)|\phi\rangle\langle\phi|\,. \tag{2.27}$$

In order to simplify Eqn. 2.27, we introduce the following operator:

$$e^{i\hat{\phi}} = \frac{1}{2\pi}\int_0^{2\pi}\mathrm{d}\phi\; e^{i\phi}\,|\phi\rangle\langle\phi|\,, \tag{2.28}$$

and by recast Eqn. 2.27 in terms of this operator, and combining the resulting exponential terms, we are left with a simplified version of Eqn. 2.24 in the phase basis:

$$\hat{\mathcal{H}} = -E_J\cos\hat{\phi}, \tag{2.29}$$

exactly as we had in Eqn. 2.20. Note that this model allows us to think of creating systems in which pairs of Cooper pairs can tunnel across the junction (then the model would connect the states $|n\rangle$ and $|n-2\rangle$), allowing for further protection of the system from certain types of decoherence [110, 111].

2.3.2 Making a two-level system

In the transmon regime, since the offset charge n_g does not impact the energy spectrum of the system, we often write the Hamiltonian of Eqn. 2.22 neglecting the offset charge. In order to transform Eqn. 2.22 into something that resembles a two-level system, we Taylor expand the cosine in Eqn. 2.22 to fourth order:

$$\hat{\mathcal{H}} = 4E_c\hat{n}^2 - E_J\left(1 - \frac{1}{2}\hat{\phi}^2 + \frac{1}{4!}\hat{\phi}^2 + \cdots\right), \tag{2.30}$$

where we have assumed that we are in the transmon regime by neglecting n_g. Furthermore, we rewrite the number and phase operators in terms of bosonic raising and lowering operators:

$$\hat{\phi} = \left(\frac{2E_c}{E_J}\right)^{1/4}\left(\hat{a}^\dagger + \hat{a}\right) \tag{2.31}$$

$$\hat{n} = \frac{i}{2}\left(\frac{E_J}{2E_c}\right)^{1/4}\left(\hat{a}^\dagger - \hat{a}\right). \tag{2.32}$$

As seen in Eqn. 2.31, the prefactor of the phase operator is related to the zero point fluctuations of that phase. These zero point fluctuations decrease with increasing E_J/E_c, justifying the use of the Taylor expansion of the cosine term. Substituting Eqns. 2.31 and 2.32 into Eqn. 2.30, we can rewrite the transmon Hamiltonian in terms of raising and lowering operators [11]:

$$\hat{\mathcal{H}} = \omega_q\hat{a}^\dagger\hat{a} - \frac{E_c}{2}\hat{a}^\dagger\hat{a}^\dagger\hat{a}\hat{a}, \tag{2.33}$$

where the qubit frequency $\omega_q = \sqrt{8E_JE_c} - E_c$ has been introduced in terms of the Josephson energy and the capactive charging energy. Recalling the derivation of Eqn. 2.19, the Josephson energy E_J depends linearly on the junction critical current I_c, which, in the case

of a SQUID loop, depends on the external flux. This allows us to dynamically tune the Josephson energy E_J and therefore the qubit transtion frequency ω_q.

Additionally, we can verify that Eqn. 2.33 does in fact give us two individual energy levels that we can address experimentally. We compute the first and second transition frequencies of the transmon as:

$$\begin{aligned} \omega_{01} &= \langle 1| \hat{\mathcal{H}} |1\rangle - \langle 0| \hat{\mathcal{H}} |0\rangle = \omega_q \\ \omega_{12} &= \langle 2| \hat{\mathcal{H}} |2\rangle - \langle 1| \hat{\mathcal{H}} |1\rangle = \omega_q - E_c. \end{aligned} \tag{2.34}$$

From Eqn. 2.34 we can see $\omega_{01} \neq \omega_{12}$, which allows us to isolate the lowest two energy levels of the transmon as a qubit. Of course, there are additional energy levels (see Fig. 2.4), but each these levels are anharmonically spaced due to the nonlinearity of the Josephson junction. Furthermore, the anharmonicity in the transmon limit is simply given by the capactive charging energy E_C, which is a geometric property of the qubit that can be controlled at the level of the device design.

2.4 Jaynes-Cummings Hamiltonian

Now that we have seen how to create a physical circuit in which we can isolate any two energy levels, how do we interact with this system? Borrowing from the framework of cavity quantum electrodynamics, in which an atomic transition is coupled to the light field in an optical cavity [112], we couple the qubit (which has a microwave frequency transition frequency) to an electromagnetic cavity having a fundamental frequency also in the microwave regime. How do these two objects interact? The transmon, which we can think of as an artificial

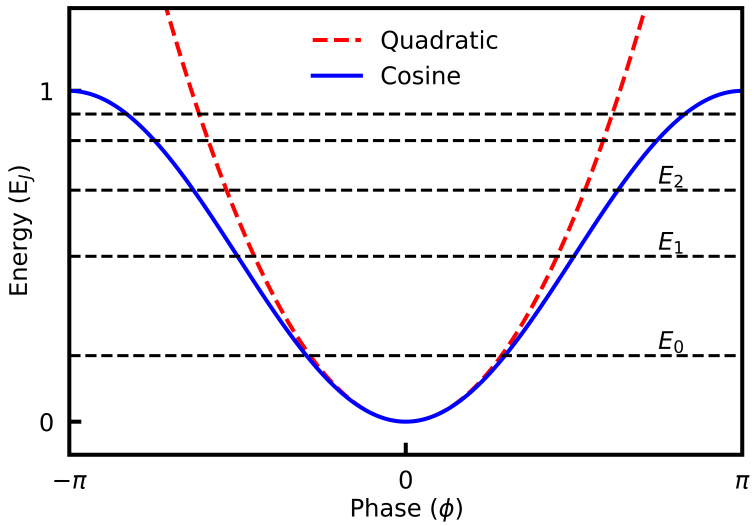

Figure 2.4: Effective potential energy versus phase difference provided for a Josephson junction. The cosine term deviates from the quadratic potential, and produces eigenvalues with non-equal spacing as indicated by the black dashed lines. For visual clarity, only the lowest three energy levels have been labeled.

atom, has a dipole moment that can be described in terms of a vector $\vec{d}_{01}$ coupled to the Pauli raising and lowering operators $\hat{\sigma}_+$ and $\hat{\sigma}_-$ as $\vec{d} = \vec{d}_{01}\left(\hat{\sigma}_+ + \hat{\sigma}_-\right)$. The quantized zero point electric field in the cavity $\vec{E}_{\mathrm{ZPF}}$ is coupled to photon raising and lowering operators $\hat{a}$ and $\hat{a}^\dagger$ as $\vec{E} = \vec{E}_{\mathrm{ZPF}}\left(\hat{a} + \hat{a}^\dagger\right)$ for a single cavity mode. The interaction between the qubits dipole moment and the cavity field can be written as in classical electrodynamics:

$$\hat{\mathcal{H}}_{\mathrm{int}} = -\vec{d}\cdot\vec{E} \tag{2.35}$$

By inserting the functional form for the dipole moment and the electric field, we can describe the qubit-photon interaction in terms of the Pauli operators for the qubit and the electric field raising and lowering operators, and rewriting the prefactors as the coupling strength g between the qubit and photons:

$$\hat{\mathcal{H}}_{\mathrm{int}}/\hbar = g\left(\hat{a}\hat{\sigma}_+ + \hat{a}^\dagger\hat{\sigma}_+ + \hat{a}\hat{\sigma}_- + \hat{a}^\dagger\hat{\sigma}_-\right). \tag{2.36}$$

The Hamiltonian of the non-interacting system can easily be described as just the Hamiltonian of the qubit plus the Hamiltonian of the cavity:

$$\hat{\mathcal{H}}_0/\hbar = \frac{1}{2}\omega_q\hat{\sigma}_z + \omega_c\hat{a}^\dagger\hat{a}, \tag{2.37}$$

where the first term represents the energy of the quantum two-level system and the second term represents the energy in the cavity, and we have neglected the zero point fluctuations of the cavity. In order to simplify the description of the composite system, it is useful to move to the *interaction picture*, where the operators evolve via their free time evolution: $\hat{\sigma}_+(t) = \hat{\sigma}_+(0)e^{i\omega_q t}$ and $\hat{a}^\dagger(t) = \hat{a}^\dagger(0)e^{i\omega_c t}$ and similarly for their Hermitian conjugates. By looking at the time evolution of each term in Eqn. 2.36 we identify "fast oscillating" terms, which oscillate at a frequency of $\omega_q + \omega_c$, as well as slowly varying terms, which oscillate at a frequency of $\omega_q - \omega_c$. In time, the quickly oscillating terms will average to zero, and thus we can often neglect them when considering the slower dynamics of tghe qubit-cavity system. This is an example of the *rotating wave approximation*, a standard tool in quantum optics [5]. After making the rotating wave approximation, the full Hamiltonian can then be written as the famous *Jaynes-Cummings Hamiltonian* [53, 54]:

$$\mathcal{H}/\hbar = \frac{1}{2}\omega_q\hat{\sigma}_z + \omega_c\hat{a}^\dagger\hat{a} + g\left(\hat{\sigma}_+\hat{a} + \hat{\sigma}_-\hat{a}^\dagger\right). \tag{2.38}$$

Eqn. 2.38 is a central building block vital for understanding the experiments in this thesis. As we will see, the interaction between the qubit and the cavity will allow for control and measurement of the qubit state via transmission through the microwave cavity. Additionally, an analogue of Eqn. 2.38 will be used in chapter 6 to measure the properties of phononic

coherent states coupled to a qubit.

In order to investigate the structure of Eqn. 2.38, it is useful to look at the energy spectrum of this Hamiltonian. How large is the Hilbert space of this system? Well, the qubit can have either zero or one excitations, and the cavity can host many photons. Solving this problem seems rather daunting, however the interaction term conserves the total number of excitations shared between the qubit and the cavity. Intuitively, we can think of the term $\hat{\sigma}_+\hat{a}$ as converting a cavity photon into a qubit excitation and the term $\hat{\sigma}_-\hat{a}^\dagger$ as doing the exact opposite process (converting a qubit excitation into a cavity photon). Because of this fact, the Hamiltonian is block-diagonal and we can write down the a 2×2 matrix that describes the energy exchange between the states $|n, e\rangle$ and $|n-1, g\rangle$, where n is the number of cavity photons and e (g) represents the excited (ground) state of the qubit. In this framework, the 2×2 Hamiltonian is

$$\hat{\mathcal{H}}/\hbar = \begin{pmatrix} (n-1)\omega_c + \frac{\omega_q}{2} & g\sqrt{n} \\ g\sqrt{n} & n\omega_c - \frac{\omega_q}{2} \end{pmatrix}. \tag{2.39}$$

Diagonalization of this Hamiltonian can be performed by introducing the mixing angle θ_n for each subspace with n excitations

$$\tan 2\theta_n = \frac{2\sqrt{n}g}{\Delta}, \tag{2.40}$$

where $\Delta = \omega_q - \omega_c$ is the detuning between the qubit and cavity frequencies. The eigenstates of the system represent the hybridization of the qubit and cavity modes, and can be written as

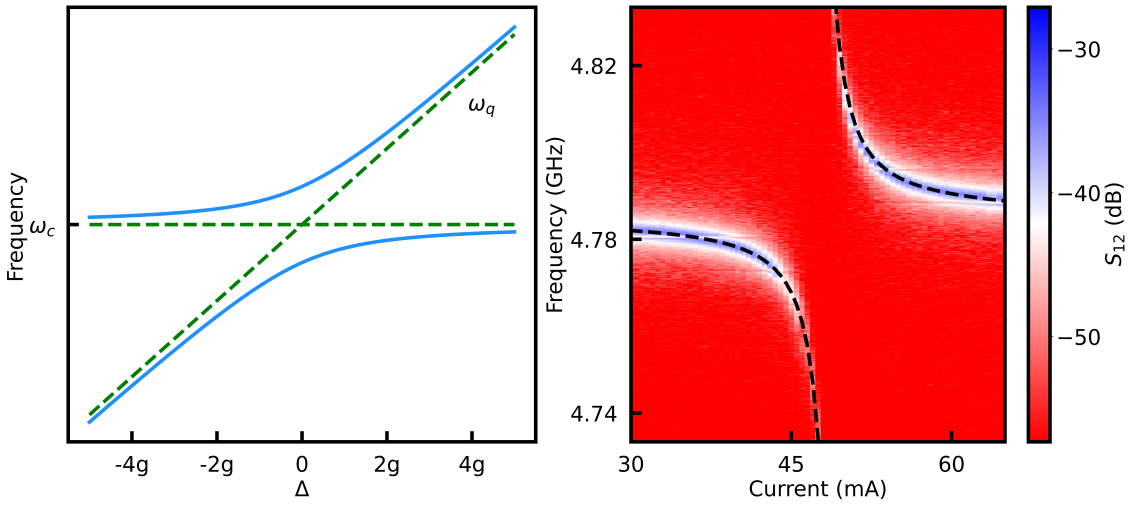

Figure 2.5: Left: energy eigenvalues of the Jaynes-Cummings Hamiltonian with a single excitation ($n = 1$). When the qubit and cavity modes are tuned near resonance ($\Delta = 0$), they hybridize and an anticrossing appears. Right: Spectroscopic measurement of a coupled qubit-cavity system as the resonant frequency of the qubit is tuned through the bare cavity frequency using an external flux created by supplying an a current to a small solenoid. The dashed black lines are a fit to the Jaynes-Cummings Hamiltonian. In this particular measurement, we extract a coupling strength of $g/(2\pi) \approx 75$ MHz.

$$|n,+\rangle = \sin\theta_n \,|n,g\rangle + \cos\theta_n \,|n-1,e\rangle \tag{2.41}$$

$$|n,-\rangle = \cos\theta_n \,|n,g\rangle - \sin\theta_n \,|n-1,e\rangle \,.$$

In Eqn. 2.41, the label $+(-)$ refers to the state with higher (lower) energy. The energy eigenvalues of the Hamiltonian in Eqn. 2.38 can be computed to be:

$$\epsilon_{n,\pm} = \omega_c \left(n - \frac{1}{2}\right) \pm \sqrt{ng^2 + \left(\frac{\Delta}{2}\right)^2}, \tag{2.42}$$

with corresponding ground state energy $\epsilon_0 = -\omega_q/2$.

As introduced in Section 2.3, we often use a flux-tunable transmon qubit. In this case, we can actually tune the resonant frequency of the qubit through the frequency of the cavity, and use this measurement to extract the coupling between the two systems. As shown in

Fig. 2.5 this is predicted by the energy spectrum of the Jaynes-Cummings Hamiltonian and a representative measurement of the qubit-cavity system confirms this coupling.

2.4.1 Resonant regime

When the frequencies of the qubit and the cavity are nearly degenerate, i.e. $\omega_q \simeq \omega_c$, the mixing angle between the eigenstates of the Jaynes-Cummings Hamiltonian approaches the limit $\theta_n \to \pm\frac{\pi}{4}$ (depending on the sign of Δ). In this limit, the two system eigenstates in Eqn. 2.41 approach equally weighted superposition states of qubit and cavity modes. By setting $\Delta = 0$ in Eqn. 2.42, we see that these two energy levels are split by $2\sqrt{n}g$, which implies that energy is "traded" back and forth between qubit and cavity excitations at a rate g. Of course, in order for the two systems of interest to exchange quanta in this coherent fashion, the coupling rate g must be the dominant rate in the system and significantly exceed the decay rate of both the qubit and the cavity modes. Since both components of the hybrid system are equally important in this resonant regime, the decay of the hybridized modes are given by $(\gamma + \kappa)/2$, where γ is the decay of the bare qubit mode and κ is the decay of the bare cavity mode.

2.4.2 Dispersive regime

In order to leverage the cavity as a tool for measuring the qubit state, we focus on the so-called "dispersive regime" of circuit quantum electrodynamics [10, 11, 103, 113]. In this regime, the detuning between the qubit and the cavity is relatively large ($g/|\Delta| \ll 1$). Rather than directly diagonalize Eqn. 2.38, one can use perturbation theory to find corrections to the energy to second order in Eqn. 2.38. Several excellent derivations of this procedure can

be found in Refs. [10, 114, 115]. By expanding Eqn. 2.38 in this fashion, we arrive at the *dispersive* Jaynes-Cummings Hamiltonian:

$$\hat{\mathcal{H}}/\hbar = \left(\omega_c + \frac{g^2}{\Delta}\hat{\sigma}_z\right)\hat{a}^\dagger\hat{a} + \frac{\omega_q}{2}\hat{\sigma}_z. \tag{2.43}$$

Importantly, we see that the effective frequency of the cavity has picked up an additional term that depends on $\hat{\sigma}_z$, meaning that the resonant frequency of the cavity will change by an amount $2\chi \equiv 2\frac{g^2}{\Delta}$ when the qubit is driven from its ground to excited state (or vice-versa). The parameter χ is called the *dispersive shift*. This qubit state-dependent cavity frequency shift is a tool that we will exploit experimentally in order to **determine the state of the qubit via measurement of the cavity transmission**. Since Eqn. 2.43 is vital to the experiments presented in this thesis, it is useful to gain some intuition regarding how the interaction between the cavity and qubit can be recast this way. Earlier, we mentioned that this Hamiltonian comes about via perturbation theory, so it is instructive to look at the energy shifts in second order perturbation theory, which are given by:

$$E^{(2)}_{n,p} = \sum_{n\neq n'}\sum_{p\neq p'} \frac{\left|\left\langle n', p'\right| g\left(\hat{\sigma}_+\hat{a} + \hat{\sigma}_-\hat{a}^\dagger\right)\left|n, p\right\rangle\right|^2}{E^{(0)}_{n,p} - E^{(0)}_{n',p'}}. \tag{2.44}$$

In Eqn 2.44, the indices n and n' represent the cavity photon excitation number, and the indices p and p' take on the values ± 1, representing the qubit "parity" (physically, this is just the ground or excited state of the qubit). The numerator in Eqn. 2.44 represents the interaction strength between unperturbed states of the system and the denominator is equal to the energetic differences of the unperturbed states that are interacting. Because the Jaynes-Cummings Hamiltonian can be represented as a block-diagonal matrix, we

would only expect coupling between the levels $|n, g\rangle$ and $|n-1, e\rangle$. As seen in Eqn. 2.39, the coupling elements are simply given by the off diagonal elements $g\sqrt{n}$. Therefore for either possibility of the qubit state $\hat{\sigma}_z$, the magnitude of the numerator of Eqn. 2.44 simply becomes ng^2. The denominator, depending on the state of interest, takes the value of $\pm\Delta$. For example, if the unperturbed state is $|n, g\rangle$, the denominator simply becomes $E_{n,1} - E_{n-1,-1} = \big(n\omega_c - \omega_q/2\big) - \big((n-1)\omega_c + \omega_q/2)\big) = -\Delta$, and vice versa for the state $|n-1, e\rangle$. As such, we can write the perturbing Hamiltonian in second order as [116]:

$$\hat{\mathcal{H}}^{(2)} = 2\chi\hat{a}^\dagger\hat{a}\hat{\sigma}_z. \tag{2.45}$$

This perturbation can be grouped with terms in the free Hamiltonian (Eqn. 2.37) to express the frequency of the cavity as "*dressed*" by the state of the qubit. The effect on both the cavity amplitude and its phase response can be seen in Fig. 2.6. However, in practice, the transmon qubit is not a simple two level system. Additional bound states within the confining potential are also present and slightly modify the dispersive shift χ. To illustrate this we follow Ref. [103] and define the total dispersive shift χ as having contributions from two partial dispersive shifts caused by the interaction between neighboring transmon levels:

$$\chi = \chi_{01} - \frac{\chi_{12}}{2}, \tag{2.46}$$

where $\chi_{ij} = g_{ij}^2/(\omega_{ij} - \omega_c)$, and the coupling strengths between the cavity field and the transmon levels scale according to $g_{n,n+1} \approx g\sqrt{n+1}$ [113], where g is the coupling rate from the Jaynes-Cummings Hamiltonian. Simplifying Eqn. 2.46 under these assumptions yields the expression for χ applicable to transmon-based circuit quantum electrodynamics

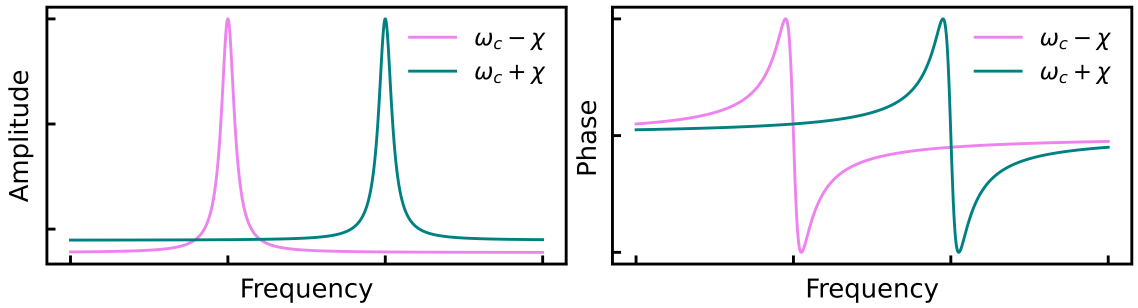

Figure 2.6: Left: amplitude response of a cavity dispersively coupled to a qubit. The state of the qubit *dresses* the resonant frequency of the cavity. Right: Phase response of the cavity under the same conditions as the left panel.

experiments:

$$\chi = -\frac{g^2}{\Delta}\left(\frac{\alpha}{\Delta - \alpha}\right), \tag{2.47}$$

where $\alpha = E_C$ is the anharmonicity of the transmon.

2.5 Microwave cavities for cQED

At this point in the thesis, we have described how we might theoretically realize a quantum two-level system and its interaction with a harmonic oscillator. Because this is a thesis on *experimental* physics, we need to learn how to put these ideas into practice in a meaningful way. Fabrication of Josephson junctions is relatively easily done using standard nanofabrication procedures (see Appendix A for fabrication recipes), and in section 2.4 we derived the Jaynes-Cummings Hamiltonian under the assumption that we would couple the dipole moment of the qubit to the electric field in a microwave cavity. Our next task is to create a physical system that behaves like a quantum harmonic oscillator and provides the necessary dipole coupling mechanism for the Jaynes-Cummings Hamiltonian. Our lab uses the standard "3D" geometry, in which the qubit is actually housed *inside* a three dimensional microwave cavity [117], rather than coupling the devices on the same chip, as pioneered

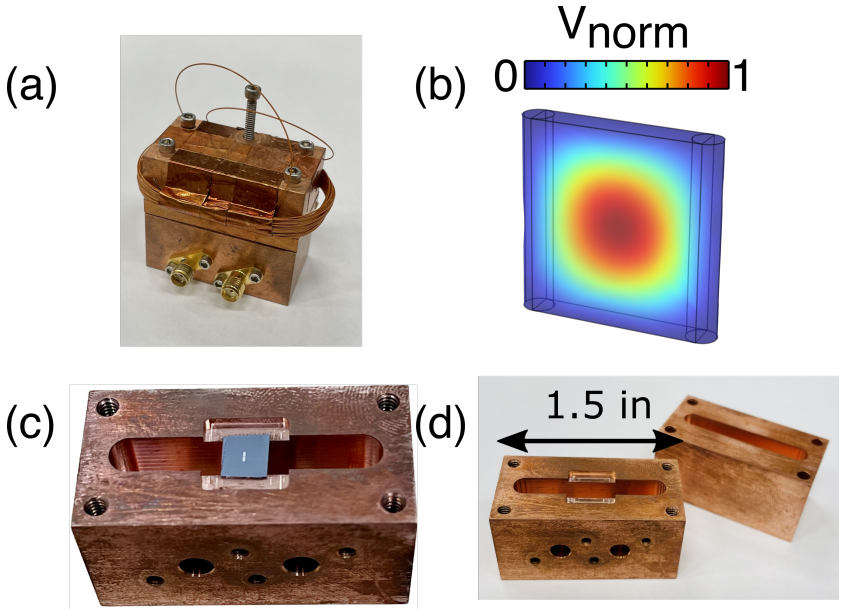

Figure 2.7: (a) Image of a fully assembled 3D cavity. The microwave input/output SMA ports are attached to the cavity and a superconducting solenoid responsible for tuning the qubit frequency can be seen. (b) Finite element method simulation of the normalized spatial voltage profile V_{norm} of the TE_{101} mode of the microwave cavity. The resonant frequency of this mode is $\omega_c/(2\pi) = 6.98$ GHz. The voltage antinode at the center of the cavity allows the electric field to couple to the dipole moment of the qubit. (c) Image of a transmon qubit housed within the bottom half of a microwave cavity. The qubit dipole antenna of dimension 250 μm $\times$ 500 μm are visible. (d) Image of an "open" cavity. The inset inside the bottom half of the cavity allows us to secure the substrate containing the qubit within the cavity.

in Ref. [12]. To create a sufficiently large dipole moment to experimentally realize significant coupling g, we fabricate large aluminum antenna paddles in series with the Josephson junction as seen in Fig. 2.7(c). These antenna paddles are also responsible for creating a large shunting capacitance, ensuring that we can achieve the correct value for E_C and subsequently reach the transmon regime. In order to create a physical system that both behaves like a quantum harmonic oscillator and can house the qubit, a slot of an appropriate dimension is milled out of two halves of bulk conducting material (typically either copper or aluminum). To estimate the resonant frequency of such a cavity, we can approximate the cavity as a 3D rectangular box with perfectly conducting walls. For a cavity having a volume $V = L_x \times L_y \times L_z$, where $L_{x,y,z}$ specify the dimension of the cavity, the resonant

electromagnetic frequencies are [118]:

$$\omega_{nlm} = c\sqrt{\left(\frac{n\pi}{L_x}\right)^2 + \left(\frac{l\pi}{L_y}\right)^2 + \left(\frac{m\pi}{L_z}\right)^2}, \tag{2.48}$$

where the indices n, l, and m are integer values that index the mode number of the cavity.

As seen in Fig. 2.7, the microwave cavities we use are *macroscopic* (you can hold them in your hand!). How can we think of something this large as a single quantum object such as a harmonic oscillator? We often use the lowest frequency mode (the TE_{101} mode of the cavity) as our mode of interest. By ensuring that the hybrid system is operated at sufficiently low temperatures ($\hbar\omega \ll k_b T$), where ω is the relevant frequency of both the qubit and the cavity modes, the hybrid quantum system should be passively cooled near its ground state and we can think of the microwave cavity as a collection of harmonic oscillators each with some transition frequency ω_k, which only depends on the geometry of the cavity. For a sense of scale, the relationship between temperature and frequency can be approximated as 5 GHz $\approx$ 240 mK. If the quality factor of each cavity mode is sufficiently large (or, equivalently, the linewidth of each mode is sufficiently small), we can think of each mode k as an independent harmonic oscillator that do not interact with each other, and the Hamiltonian can be written as:

$$\hat{\mathcal{H}} = \sum_k \omega_k \hat{a}_k^\dagger \hat{a}_k. \tag{2.49}$$

By ensuring that the frequency of both the qubit and cavity mode of interest are largely detuned from the other cavity modes, we can think of our microwave cavity as a single mode cavity. Although this approximation holds very well for the results of this thesis, the presence of these additional cavity modes will contribute to both qubit dephasing and energy decay [81, 119]. Additionally, the qubit within the cavity slightly modifies the spatial profile

of all cavity modes [120].

2.5.1 Aside: experimental preparation of coherent states

As we apply a classical drive signal to our microwave cavity, all of the transitions in the harmonic oscillator are simultaneously driven, leading to a coherent state. In this subsection, we provide a brief refresher on coherent states of the harmonic oscillator and how they can be realized in the lab. The wavefunction for a harmonic oscillator in a coherent state is given by:

$$|\alpha\rangle = e^{-\frac{|\alpha|^2}{2}} \sum_{n=0}^{\infty} \frac{\alpha^n}{\sqrt{n!}} |n\rangle \,. \tag{2.50}$$

Here $|n\rangle$ are the Fock states of the resonator, and $|\alpha|^2 = \langle n \rangle$ is the mean excitation number. It is then straightforward to calculate the probability of the resonator having m excitations:

$$|\langle m|\alpha\rangle|^2 = \left| e^{-\frac{|\alpha|^2}{2}} \sum_{n=0}^{\infty} \frac{\alpha^n}{\sqrt{n!}} \delta_{mn} \right|^2 . \tag{2.51}$$

Carrying out this calculation, one finds the probability of having m excitations in the resonator, given a coherent state with $\overline{n}$ mean excitations:

$$P_{\overline{n}}(m) = e^{-\overline{n}} \, \frac{\overline{n}^m}{m!} \tag{2.52}$$

The result, Eqn. 2.52, is very important, it shows that populating a resonator with a coherent state leads to a Poisson probability distribution, which in general, is asymmetric about the mean.

Coherent states can be generated via the following *displacement operator*:

$$\hat{\mathcal{D}}(\alpha) = \exp(\alpha\hat{a}^\dagger - \alpha^*\hat{a}). \tag{2.53}$$

By using the well known operator identity [121]: $e^{\hat{A}}e^{\hat{B}} = e^{\hat{A}+\hat{B}}e^{-\frac{1}{2}[\hat{A},\hat{B}]}$, it is possible to re-write the displacement operator as

$$\hat{\mathcal{D}}(\alpha) = e^{-\frac{1}{2}|\alpha|^2}e^{\alpha\hat{a}^\dagger}e^{-\alpha^*\hat{a}}. \tag{2.54}$$

From this point, it is possible to identify the following properties of the displacement operator [5]:

$$\begin{aligned}
&\hat{\mathcal{D}}^\dagger(\alpha) = \hat{\mathcal{D}}^{-1}(\alpha) = \hat{\mathcal{D}}(-\alpha) \\
&\hat{\mathcal{D}}^\dagger(\alpha)\hat{a}\hat{\mathcal{D}}(\alpha) = \hat{a} + \alpha \\
&\hat{\mathcal{D}}^\dagger(\alpha)\hat{a}^\dagger\hat{\mathcal{D}}(\alpha) = \hat{a}^\dagger + \alpha^*.
\end{aligned} \tag{2.55}$$

Furthermore, by applying the identites listed in Eqns. 2.55 to the vacuum state $|0\rangle$, it is possible to identify the displacement operator as the one that creates a coherent state from the vacuum:

$$|\alpha\rangle = \hat{\mathcal{D}}(\alpha)\,|0\rangle\,. \tag{2.56}$$

Finally, we turn to the functional form for Eqn. 2.53, we see that the argument is (up to a phase) the same as that of the cavity electric field described in Section 2.4, indicating that displacing a harmonic oscillator in phase space with a time varying electric field will generate a coherent state! This detail will be an important for the key results of chapter 7.

2.6 Conclusion

This chapter has introduced circuit quantum electrodynamics (cQED). We began by describing a quantum mechanical description for the LC oscillator. We then discussed the Josephson junction as a means for creating non-linear circuits, and this allowed us to create a quantum mechanical two level system. We then introduced the Jaynes-Cummings Hamiltonian and explored how this interaction will allow us to measure the state of the qubit via a microwave cavity. The next chapter will describe measurement techniques in cQED using the key ideas presented in this chapter.

Chapter 3

Measurement in Circuit Quantum Electrodynamics

3.1 Introduction

The previous chapter introduced the theoretical framework of circuit quantum electrodynamics (cQED), allowing us to couple a superconducting qubit to a microwave cavity. This chapter aims to expand upon the theoretical background outlined in the previous chapter and introduce several experimental techniques for characterization of the cQED and cQAD systems studied in this thesis. We will begin by discussing the cryogenic system and the key electronic components in our experimental setup. We then describe basic spectroscopic measurements of the hybrid qubit/cavity system. These spectroscopic measurements serve as a calibration for the more complicated measurements of the qubit in the time domain, which are important for the open quantum systems work of chapter 6. We describe the latest "upgrade" to the experimental measurement capabilities in our lab, i.e. integrating our superconducting qubit measurements with a field programmable gate array (FPGA) measurement setup allowing for increased control of the system while simultaneously increasing the rate at which we can perform measurements. Finally, we note that a complete description of the original measurement setup can be found in the thesis of J. R. Lane (Ref [122]).

3.2 The cryostat and input/output lines

We typically operate our superconducting qubits and microwave cavities with resonant frequencies in the GHz regime (a small aside: it is possible to operate some special types of superconducting qubits at much lower frequencies, even as low as tens of MHz, see Refs. [123–126]). In order for these GHz-frequency systems to be passively cooled to near their quantum ground state, the systems must be cooled to very low temperatures relative to their transition frequencies (recall that 5 GHz $\simeq$ 240 mK). To ensure near-unit probability that both the qubit and the cavity are thermally initialized to their ground state, our lab employs a cryogen-free BlueFors LD-400 dilution refrigerator having a nominal lowest temperature below 10 mK (in practice, we often introduce enough experimental heat load to the cryostat that the minimum temperature is closer to 15 mK). Even so, we typically infer the effective temperature of the cQED system via measurements of the residual excited state population of the qubit (see Refs. [127,128] for a description of this experimental technique), and find that the qubit-cavity system is at a higher temperature than the thermometer at the lowest temperature stage (the mixing chamber) of the cryostat to which the experiment is mounted [129, 130]. Nonetheless, operating the hybrid system at these low temperatures serves as an effective starting point for our experiments, largely initializing (on average) all the components of the hybrid system near their quantum mechanical ground states.

At this point, we have emphasized that we will need to implement coupling between a qubit and a microwave cavity to carry out the experiments relevant to this thesis. We have not, however, described how we get the relevant GHz-frequency drive signals into the cryostat or how we will preserve the "quantum" integrity of the output signals. To explain the measurement wiring in the cryostat we will trace the path from room temperature, down

the input line to the hybrid system, and back out through the measurement output line (see Fig. 3.1). On the input line, we attenuate the signal by 60 dB (six orders of magnitude in the *power* of the signal). By strongly attenuating the input control signal, we also attenuate any higher frequency electromagnetic black-body radiation from higher temperature stages within the cryostat. This thermal radiation can exist at frequencies comparable to the resonant frequency of the cavity modes, which can lead to spurious population of photons in the cavity and thus destroy the phase information of the qubit [119, 131]. This electromagnetic radiation can also exist at frequencies comparable to the superconducting gap of aluminum and can therefore lead to qubit depolarization via the breaking of Cooper pairs [132]. We distribute the attenuation over three different stages within the cryostat to minimize resistive heating in the attenuator at any one stage. These attenuators also provide a thermal contact between the inner pin of the coaxial cable and ground. In addition to attenuating the input signal, we also use two different types of filters at the mixing chamber stage of the cryostat to further condition the drive signal applied to the qubit and cavity. We use commercially available low pass filters (LPFs) (K&L Microwave 6L250-00088), which strongly filter any signals at frequencies higher than the operating frequency of a given experiment (typically a cut-off frequency of 8 GHz is sufficient for our purposes). In order to further protect the system from spurious high-frequency photons, we also connect homemade epoxy-based filters (called "Eccosorb" filters) based on the recipe in Ref. [133] in series with the input line.

In order to protect the system from unwanted radiation coming down the output line, we protect the experiment with two cryogenic microwave circulators (Raditek RADC − 4 − 8 − Cryo − 4 − 77K − S23 − 1WR-MS-b) connected in series and thermally anchored to the mixing chamber. Each circulator provides approximately 30 dB of isolation from counter-propagating signals, leading to a total of 60 dB of attenuation for signals directed

down the measurement chain towards the experimental cell. Interestingly, there have been several recent advances towards integrating on-chip non-reciprocal circuit elements for further protection from noise via the output line [134, 135].

Since we significantly attenuate the input excitation signal and would like to measure the small signals produced by the experiment, we need to incorporate low-noise amplification to increase the size of the output of the measurement circuit in order to have signals of large enough amplitude to reliably measure. An amplifier will not only amplify the signal at its input, but also any noise "on top" of that signal. Even worse, the amplifier will also add *additional* noise to the output signal. This added noise is often characterized by an effective *noise temperature* and it can be shown that for a chain of amplifiers in a circuit, the total noise temperature for the amplification chain depends most strongly on the noise temperature of the first amplifier in the chain [80] (by *first* we mean the first amplifier that the signal reaches coming from the experiment). The first amplifier in our measurement chain is a commercially available High Electron Mobility Transistor (HEMT) amplifier made by Low Noise Factory (LNF) (LNF − LNC03_14A) mounted on the 4K stage of the cryostat that provides $\simeq$ 42 dB of gain with an effective noise temperature of approximately 3.5 K over its functional bandwidth (0.3-14 GHz). We further amplify the signal at room temperature using two low-noise high frequency amplifiers (Minicircuits ZX60-83-LN-S+) for a total gain of $\simeq$ 86 dB. Refs. [122, 129] provide a more detailed description of the experimental circuitry we typically use in our experiments. Since the first amplifier in the amplification chain is in some sense the most important (due to its contribution to the total noise temperature), the addition of a quantum limited amplifier would be of great use for our lab. Josephson parametric amplifiers (JPAs) [136–138] and traveling wave parametric amplifiers (TWPAs) [139, 140] are becoming of increasing importance for high-fidelity, single

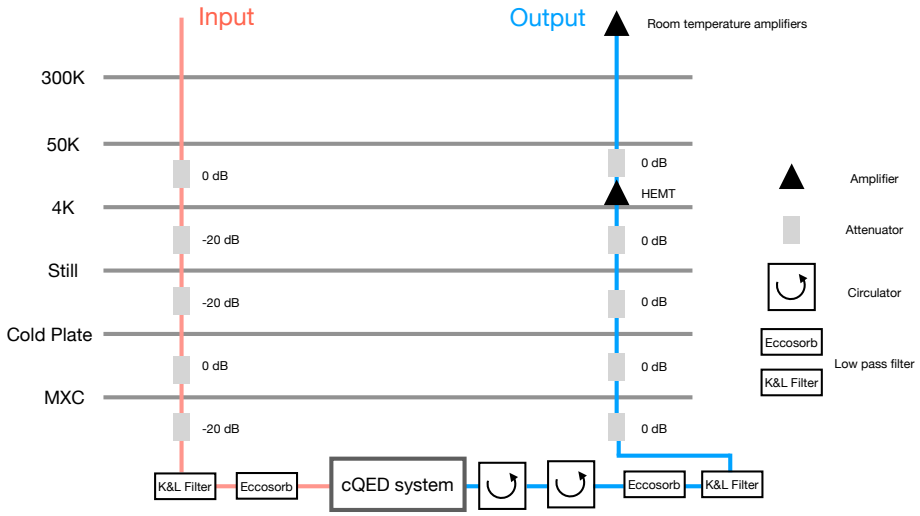

Figure 3.1: Schematic of the cryostat microwave wiring showing the relevant filtering, attenuation, and amplification.

shot measurement in cQED systems. Our lab has recently purchased a commercially available JPA (Raytheon BBN-PS2-JPA-DEVICE-QEC) which should (in principle) offer a minimum gain of 20 dB over an instantaneous bandwidth of 300 MHz while adding minimal noise to the output signal (the quoted noise temperature of this JPA is approximately 300 mK). At the time of the writing of this thesis, calibration of the JPA in our system has yet to be done, but will offer significant advances in the readout fidelity in our experiments.

3.3 High-Power cQED readout

Having described how we will get signals into and out of our experimental system, we will introduce the basic measurements we carry out when cooling down a sample for the first time. Often, the first question we ask upon reaching base temperature is: "Is the qubit alive?" By this, we really mean: "Is there a properly functioning Josephson junction whose dipole moment is coupled to the cavity electric field?" In order to answer this simple, yet important, question we typically first do what we colloquially call a "punch-out" measurement [141]. In

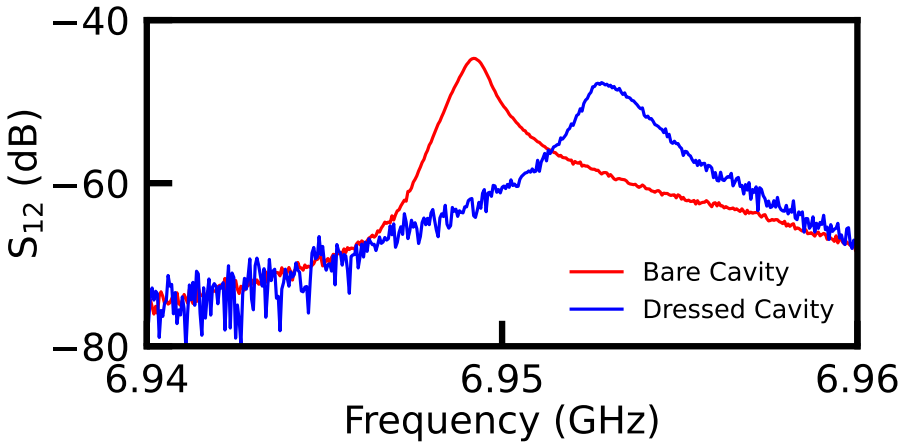

Figure 3.2: Transmission through the microwave cavity at low power ($P_{\text{in}} = -30$ dBm (blue)) compared to the "bare" cavity transmission observed at high power ($P_{\text{in}} = -10$ dBm (red)). In this measurement the measurement power is taken to be the input power at the top of the cryostat. As the cavity becomes populated with many photons, the resonant frequency of the cavity shifts from the dressed cavity frequency to the bare cavity frequency.

this type of measurement, we monitor the transmission through the microwave cavity using a vector network analyzer (VNA) (Agilent N5230A PNA-L Network Analyzer). As we increase the amplitude of the input signal, we measure a shift in the resonant frequency of the cavity from $\omega_c + \chi$ at low measurement power to ω_c at larger measurement power, where ω_c is the *bare cavity frequency* and χ is the dispersive shift due to the coupling between the qubit and cavity. As we increase the amplitude of the input signal, a model of the hybrid system has two solutions that destructively interfere, creating a dark state in the transmission of the signal. As the power increases to a critical power (this critical power depends on the state of the qubit) the system supports a "bright state" at the bare cavity frequency ω_c. The key concept that makes this method of qubit state readout possible is that the onset of the bare cavity response (the aforementioned bright state) in Fig. 3.2 occurs at a lower power if the qubit is in the state $|1\rangle$ versus the state $|0\rangle$ [141–143]. This means that if we send in a high-power microwave signal to the cavity at the bare cavity frequency ω_c at near the nominal "punch-out" power, the transmission through the cavity will be large when the

qubit is in state $|1\rangle$ as compared to the transmission through the cavity when the qubit is in state $|0\rangle$. If the qubit is not functioning, the resonant frequency of the cavity is independent of the input power.

3.4 Cavity spectroscopy

Many of the important experiment we carry out involve a transmon qubit in a SQUID loop geometry (see Section. 2.3), and we need to determine if the qubit responds to an external tuning magnetic field. Therefore, our next calibration measurement is typically to measure the response of the cavity at low drive powers (such that the cavity frequency is dressed by the qubit) as we tune the resonant frequency of the qubit with a magnetic flux. To supply this flux though the SQUID loop of the transmon, we wind a copper-clad niobium ($T_C \simeq 9$K) twisted pair wire around the microwave cavity 30 times. This twisted pair is then thermalized at each stage within the cryostat and connected to a Keithley 2400 SourceMeter at room temperature. Based on the coil geometry (the number of times the wire is wound around the cavity and the area of the SQUID loop), we estimate that we thread a single flux quantum through the SQUID loop in this geometry every $I_{\text{wire}} \simeq 125$ mA, where I_{wire} is the DC current through the coil sourced at room temperature. We then set the current to a particular value and measure the response of the cavity before stepping to the next current. This allows us to tune the qubit through its entire range of possible frequencies (determined by the geometry of the system and the maximum Josephson energy E_J). As we tune the qubit resonance through the resonance of the cavity, we fit the data to a model of coupled resonances and extract the coupling rate between the qubit and the cavity (see Fig. 3.3).

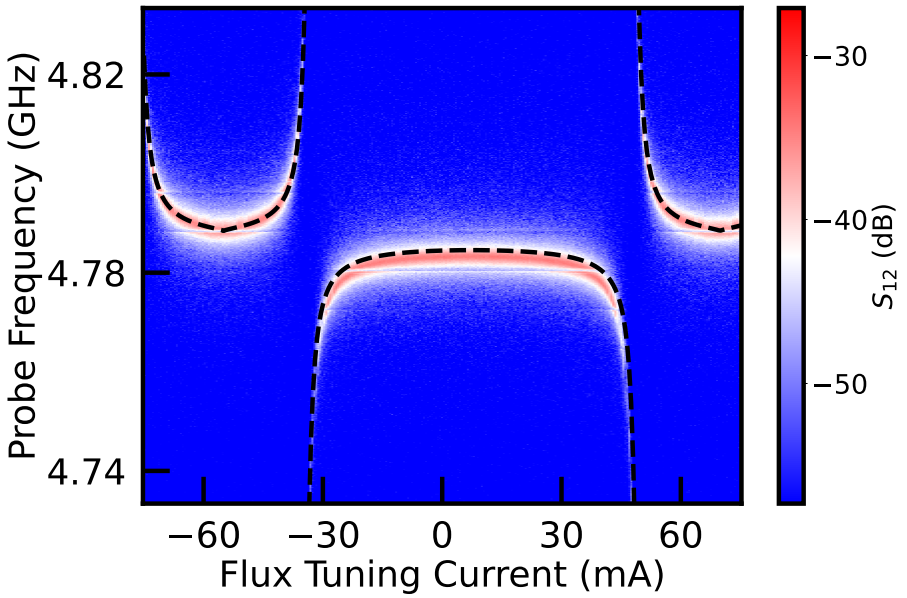

Figure 3.3: Transmission through the microwave cavity as an external flux tunes the resonant frequency of the qubit. As the detuning Δ between the qubit and cavity modes approaches zero, an avoided crossing between the modes is observed. The spectrum is fit to a model of coupled resonances (black dashed line) to extract the qubit-cavity coupling rate, which is $g/(2\pi) = 75$ MHz in this case.

3.5 Qubit spectroscopy

Having described the effect of the qubit state on the cavity, we next turn our attention to a more direct measurement of the qubit spectrum using a method known as *two-tone spectroscopy* [56]. This form of spectroscopy allows us to infer the absorption spectra of the qubit by leveraging the dispersive interaction between the qubit and the cavity. In this measurement protocol we continuously monitor the transmission through the cavity at the *dressed* cavity frequency $\omega_c + \chi$ on the VNA while simultaneously sending in another variable frequency signal into the cavity using a continuous wave (CW) microwave source (Berkeley Nucleonics Model 845). When this second tone is resonant with the qubit frequency, the qubit state will oscillate between ground and excited states, and the cavity frequency will shift depending on the state of the qubit [11]. On the timescale of our measurement (we

normally average the cavity transmission at a given qubit probe frequency for ∼1 second), the qubit is, on average, in the excited state with probability of 1/2. This leads to an average shift of the resonant frequency of the cavity and therefore a drop in transmission at the frequency $\omega_c + \chi$. This dip in cavity transmission allows us to measure the qubit frequency ω_q to high precision. In fact, measurement of the qubit spectra can allow us to learn about the population of the cavity modes, since the dispersive interaction between the qubit and the cavity also impacts the frequency of the qubit (see Eqn. 2.43). This feature is the crux of the surface phonon interference measurements presented in chapter 7.

If we increase the power of the signal driving the qubit transition in this two-tone measurement, we can excite the two photon transition of the transmon state from $|0\rangle \rightarrow |2\rangle$. The frequency at which this transition occurs is $\omega_{02}/2$ (since we require two photons to actually drive this transition). Assuming the device is operated sufficiently far into the transmon regime ($E_J/E_C \gg 1$) this allows us to extract the anharmonicity $\alpha = 2 \times (\omega_{02}/2 - \omega_{01})$. Fig. 3.4 shows a representative measurement of both the ω_{01} and $\omega_{02}/2$ transitions. Finally, if the qubit is strongly interacting with another quantum system (such as an acoustic resonator mode), we can tune the frequency of the qubit through its resonance and extract the coupling strength between qubit and this additional system. As we will see in chapter 6 we use this protocol to measure the coupling between the qubit and a surface acoustic wave mode in our hybrid quantum acoustic system (see Fig. 6.3).

3.6 Coherent control

Up to this point in this chapter we have described only continuous wave (CW) measurements. In these types of experiments, the measurement time is often much longer than the qubit

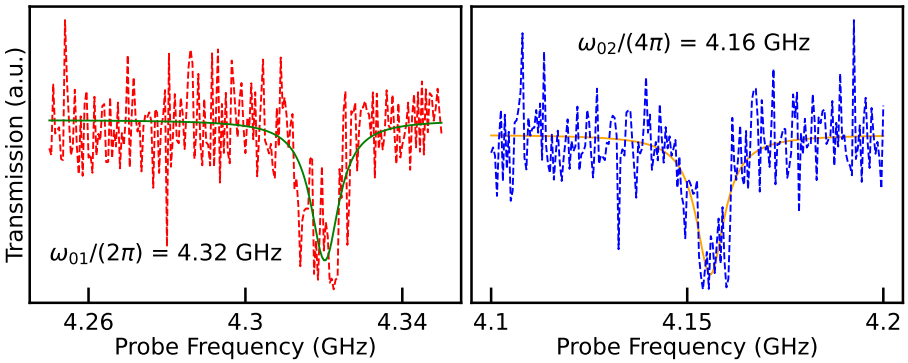

Figure 3.4: Left: measurement of the qubit ground to excited state transition via two-tone spectroscopy. The qubit frequency is extracted from the dip in the spectrum. Right: measurement of the two photon transition from the state $|0\rangle$ to $|2\rangle$. From these measurements, we can extract an anharmonicity $\alpha/(2\pi) \simeq 320$ MHz for this particular device.

lifetime, and therefore we are unable to directly measure either the direct depolarization or decoherence of the qubit in time. In this section, we will modify the measurement circuit such that we can perform measurements in the time domain. In particular, rather than measuring the spectrum of either the qubit or cavity on the VNA, we use an arbitrary waveform generator to synthesize pulses to a high precision in the time domain and quickly measure the output signal from the device with an analog-to-digital converter (ADC). The crux of this measurement circuit is an arbitrary waveform generator (AWG) with sampling rate 1 GS/s (yielding a minimum time resolution of 1 ns for pulses). Our lab uses a four channel AWG (Tabor Electronics WX2184C), which we often just refer to as "the Tabor". We use microwave frequency IQ mixers to modulate the microwave signals we send into the cryostat. An IQ mixer is a four-port device with three inputs, we use two of the inputs to the IQ mixer as low-frequency modulation signals, which we call $I(t)$ and $Q(t)$. Additionally, we apply an signal using a CW microwave source at a frequency ω to the local oscillator (LO) port of the mixer (the 3^{rd} input port) $LO(t) = A\cos(\omega t)$. Two output signals from the Tabor at frequency ω_m are sent into the I and Q ports of an IQ mixer nominally 90 degrees

out of phase with each other, yielding the following time dependence:

$$I(t) = A_{\text{mod}} \cos(\omega_m t + \phi) \tag{3.1}$$

$$Q(t) = A_{\text{mod}} \sin(\omega_m t + \phi), \tag{3.2}$$

where A_{mod} is the amplitude of the pulse and ϕ is the phase shift of the oscillatory signals in the pulses. Under these conditions with the signals going into the I, Q, and LO ports, it may be shown that the signal out of the RF port will be:

$$RF(t) = A \times A_{\text{mod}} \cos((\omega + \omega_m) t + \phi), \tag{3.3}$$

where A is the amplitude of the signal into the LO port. Eqn. 3.3 shows that we can control the relative amplitude, frequency, and phase of the output of an IQ mixer if we have precise control over the parameters of the pulses going into the I, Q, and LO ports of the mixer. As such, the signals from the Tabor allow us to quickly synthesize pulses with well-defined values for these parameters.

The typical mode of operation for time domain experiments in our lab is to set the LO source at a frequency $\omega_q - \omega_m$, where ω_q is the qubit frequency and ω_m is the modulation frequency on the Tabor output (we typically use a modulation frequency of $\omega_m/(2\pi) =$ 150 MHz, although it certainly is possible to use other values). We then tune the parameters of the signals into the I and Q ports of the IQ mixer while monitoring the signal out of the RF port on a spectrum analyzer (Agilent 8592B) in order to verify that the signal sent into the cryostat only has significant spectral components at the frequency ω_q. By uploading a file containing information to encode a pulse sequence to the Tabor having the appropriate

pulse parameters (i.e. the length, amplitude, or phase of the pulse in Eqn. 3.3), we may perform measurements of the system as a function of these pulse parameters.

A first calibration measurement of the qubit state in the time domain is the oscillation between its ground and excited state, called *Rabi oscillations* [144]. By applying a microwave signal at frequency ω_q to the qubit and measuring the probability that the qubit is in its excited state as a function of the length of the pulse, we can verify that we are able to drive the qubit from its ground to excited state (and measure this oscillation via the transmission through the microwave cavity). We repeat the pulse sequence many times (typically we average on the order of 1000 measurements) and bin the measured transmission through the microwave cavity in a histogram, allowing us to discriminate between the qubit ground and excited state (see Fig. 3.5). A representative Rabi oscillation for a transmon in our lab is shown in Fig. 3.5.

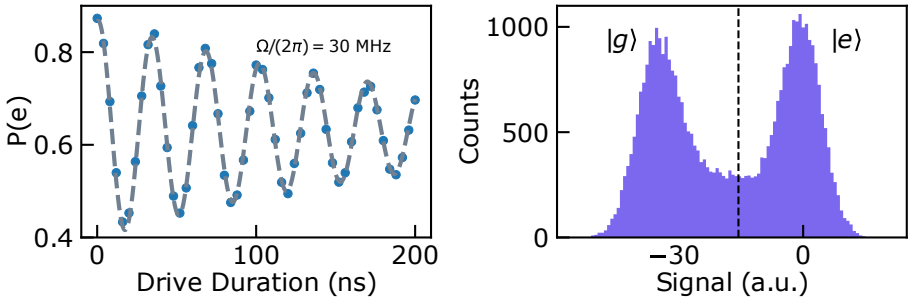

Figure 3.5: Left: Representative Rabi oscillation between the qubit ground and excited state. By fitting the data (blue dots) to a decaying sinusoid (dashed grey line), we extract a Rabi frequency of $\Omega/(2\pi) = 30$ MHz in this case. Right: Representative distribution of readout signals from the system. In this particular measurement we prepare the qubit in its ground state, measure the transmission through the cavity and repeat the process, preparing the qubit in its excited state. The vertical dashed line represents the threshold value for the cavity transmission. We attribute all signals to the left of the dashed line as corresponding to the qubit in its ground state and all measurements to the right of the dashed line as the qubit excited state.

Measurement of Rabi oscillations also serves as an important calibration for subsequent experiments: for a given set of drive parameters we are able to measure *how long* it takes our

microwave signal to drive the qubit from the ground state to excited state (or vice versa). We refer to a pulse that drives the transition $|0\rangle \rightarrow |1\rangle$ as a π-pulse, since this corresponds to rotation of π radians of the qubit state vector on the unit sphere (also called the *Bloch sphere*).

Having calibrated the π-pulse for a given set of drive parameters, we are then able to measure the coherence properties of the qubit in the time domain. By applying a π-pulse to the qubit and preparing the $|1\rangle$ state, we are able to measure the probability that the qubit remains in this state as a function of time. Colloquially, this type of measurement asks the question "If I give the qubit a single quanta of energy, how long, on average, does the qubit remain in its excited state?" By fitting the resulting (typically) exponential decay of this measurement as a function of time, we can extract the qubit energy relaxation time, which is referred to as T_1. See Fig. 3.6(a) for a representative T_1 measurement and corresponding fit.

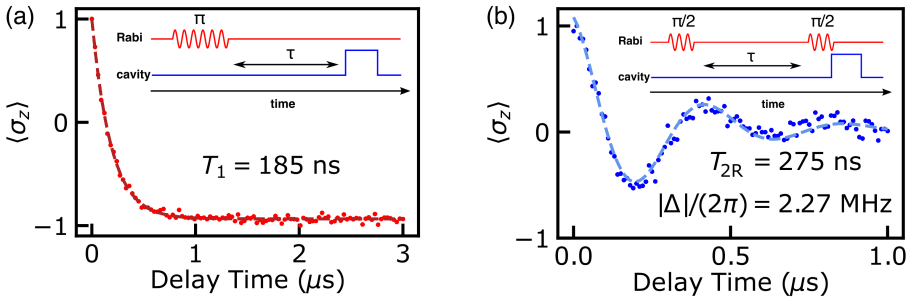

Figure 3.6: (a) Representative qubit energy decay measurement. The relevant pulse sequence is shown in the inset. (b) Representative Ramsey decay measurement. The microwave pulse sequence is shown in the inset. For ease of fitting, we often detune the drive pulses from the qubit transition frequency, leading to the oscillation seen in the data.

In order to measure the phase coherence of the qubit, we apply what we call a $\pi/2$-pulse, which is identical to a π-pulse, except having half the duration (additionally we could, in principle, keep the length of the pulse the same and divide the amplitude of the

pulse by 2). This change to the pulse duration then creates a superposition state of the qubit $|\psi\rangle = 1/\sqrt{2}\left(|0\rangle + e^{i\phi}|1\rangle\right)$, where the phase ϕ is set by the phase of the pulse (see Eqn. 3.3). After preparing a superposition state, we let the state evolve for a variable time before applying another $\pi/2$-pulse with the same phase as the first and measure the state of the qubit. If these pulses are detuned from the qubit frequency ω_q by an amount Δ, the resulting measurement yields a decaying sinusoid having frequency Δ. The decay constant of the sinusoid is called the Ramsey decay time, T_{2R} (see Fig. 3.6(b)). In general, throughout the process of this measurement, the qubit state can lose both phase information as well as emit energy (i.e. undergo a T_1 process). Together, the two decay times T_1 and T_{2R} allow us to calculate the pure dephasing time T_ϕ as:

$$T_\phi = \left(\frac{1}{T_{2R}} - \frac{1}{2T_1}\right)^{-1}. \tag{3.4}$$

Note that in order for the dephasing time T_ϕ to be a positive number, it is physically required that $2T_1 \geq T_{2R}$. Dephasing processes occur at a rate $\Gamma_\phi = 1/T_\phi$ and are produced by variations in the qubit frequency ω_q in time. If these variations are reversible in time, we could actually maintain the phase information in the qubit state for a longer duration. The addition of a π-pulse centered between the two $\pi/2$-pulses in a Ramsey decay measurement "refocuses" low-frequency noise and actually increases the measured decay constant. This is an example of a Hahn echo measurement, a technique developed for nuclear magnetic resonance (NMR) experiments [145] where the "echo" represents the refocusing of the qubit state subject to the aforementioned time reversible noise. We often call the resulting decay constant from a Hahn echo measurement $T_{2,\text{echo}}$, which is related to the Ramsey decay constant as $T_{2,\text{echo}} \geq T_{2R}$. However, in our devices, we often find that $T_{2,\text{echo}} \simeq T_{2R}$,

indicating that this type of low-frequency time reversible phase noise is not the dominant source of dephasing. This echo experiment can be thought of as applying a filter function in the frequency domain, effectively shaping the noise power spectrum experienced by the qubit. By applying many echo pulses to the system throughout a measurement of the phase coherence, one can effectively filter out low frequency noise in the system (this frequency cutoff is related to the number of echo pulses), a technique known as a Carr-Purcell-Meiboom-Gill (CPMG) measurement [146].

3.7 Quantum state tomography

A standard measurement of a superconducting qubit will give us the expectation value of the qubit state in the z-basis (i.e. we measure is $\langle\sigma_z\rangle$). However, this measurement does not provide any information about the phase of the qubit state vector. In order to learn something about this phase one can apply a $\pi/2$-pulse about either the x or y-axis of the Bloch sphere to re-project any component of the qubit vector to one of the poles of the Bloch sphere. In order to fully characterize the qubit state vector, we often repeat a given measurement three times, one measurement without an extra $\pi/2$-pulse, and two more measurements with the extra $\pi/2$-pulse about either the x or y-axis of the Bloch sphere. Together, these measurements allow us to reconstruct both the amplitude and phase of the qubit state vector, and this measurement technique is known as *quantum state tomography*. An example pulse sequence of state preparation and tomography measurement is shown in Fig. 3.7.

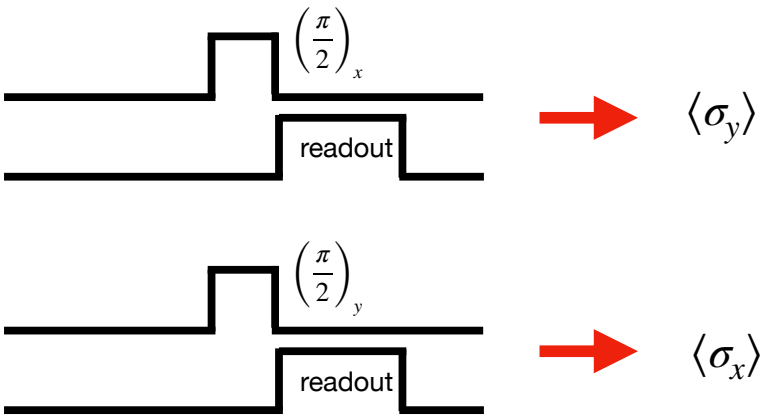

Figure 3.7: Representative pulse sequence for quantum state tomography. By applying a $\pi/2$ rotation about the x-axis (y-axis) of the Bloch sphere, we project the y-component (x-component) of the qubit state vector onto the z-axis of the Bloch sphere and subsequent measurement in the z basis allows us to measure $\langle\sigma_y\rangle$ ($\langle\sigma_x\rangle$). To measure $\langle\sigma_z\rangle$, no additional rotation is required.

The re-projection pulse is turned off to measure $\langle\sigma_z\rangle$. In order to measure $\langle\sigma_x\rangle$, the tomography pulse should have relative phase 90° (assuming that the x-axis of the Bloch sphere is defined as driving the system with relative phase 0°). And finally to measure $\langle\sigma_y\rangle$, the tomography rotation pulse should have a relative phase of 0°, assuming the same phase convention.

Measurement fidelity calibration

Unfortunately, we never actually measure the qubit with perfect fidelity. This leads to an arbitrary signal difference between the qubit excited and ground states. For a simple measurement of the qubit coherence time this does not matter, it only leads to a reduction in the overall amplitude or contrast of the signal and does not impact the extracted coherence time. However, for a tomography measurement, we hope to learn about the dynamics of the expectation values of the qubit projection along a given axis of the Bloch sphere, which should be bounded by ± 1. In order to rescale the experimental data to conform to these

bounds, an additional calibration of the measurement fidelity is needed. In general, one needs to calibrate the measurement fidelity along six different axes of the Bloch sphere ($|e\rangle, |g\rangle, |+x\rangle, |-x\rangle, |+y\rangle$, and $|-y\rangle$). This is done by preparing each of these states and re-projecting it to a pole of the Bloch sphere where a standard measurement of the qubit state gives the relative measurement contrast for that state.

A representative measurement outcome for this calibration protocol is shown in Fig. 3.8:

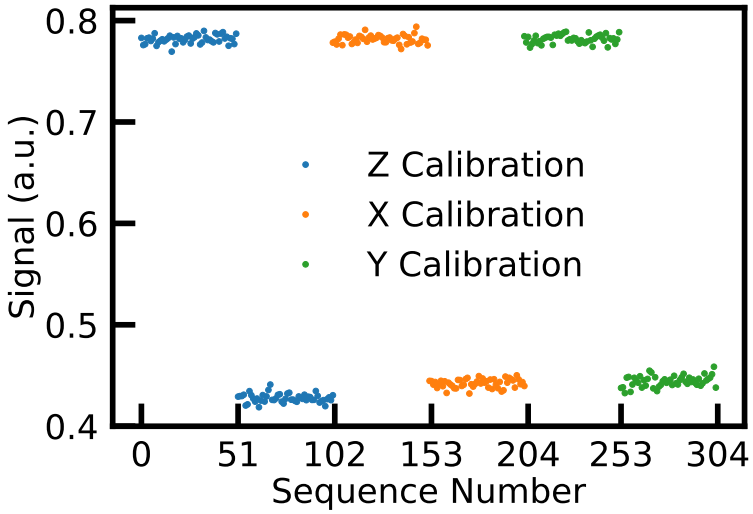

Figure 3.8: Representative calibration of all three Bloch sphere axes

For the calibration data shown in Fig. 3.8, we can see that the signal for the "excited state" is approximately 0.8, and the signal for the ground state is near 0.4. In order to rescale experimental data given this measurement fidelity we scale (for a given axis) the data using the following equation:

$$\text{Scaled Data} = 2 \times (\text{Raw Data} - S_i) / D_i, \tag{3.5}$$

where S_i is the mean of the contrast between the excited and ground state for the i^{th} axis (in our example here it would be $S_i = (0.8 + 0.4)/2 = 0.6$) and D_i is the difference in contrast

between the two states, here $D_i = 0.8 - 0.4 = 0.4$. The additional factor of 2 comes from the fact that our data acquisition software measures a probability (bounded between 0 and 1) and we are interested in expectation values (bounded between -1 and +1).

Phase correcting quantum state tomography data

In order to correct tomography data such that we can discuss the dynamics of the qubit expectation values one must scale the results according to the prescription outlined in the previous section. In the case of a resonant drive, this is quite simple (the state preparation pulse is either in phase with or 90° out of phase with the tomography pulses). In the case where the state preparation pulse is detuned from the qubit frequency, there will be unwanted phase accumulation because the drive is not stationary relative to the qubit (i.e. the frame rotating with the drive is no longer the same as the frame rotating with the qubit). In order to correct for this unwanted phase accumulation, the tomography pulses must have an adjusted phase of $\phi^{'} = \phi - (\Delta \times t)$. For example, in order to measure $\langle \sigma_x \rangle$, the phase of the tomography pulse should be $\phi^{'} = 90° - (360° \times \Delta \times t)$, and likewise for $\langle \sigma_y \rangle$, $\phi^{'} = 0° - (360° \times \Delta \times t)$. Here, Δ is the detuning between the drive and the qubit frequency and t is the *length of time between the beginning of the pulse sequence and the time at which the tomography pulses are turned on.* It is important to make sure that the sign of Δ is correct, but this can be easily verified and changed by adding this correction to the phase of the tomography pulses rather than subtracting it if necessary. When the calibration is done correctly the evolution of tomography data as a function of Δ will be smooth in Δ rather than something that looks periodic. If the data looks periodic in Δ, that should be a clear sign that the phase correction is not correct and the relative rotating frames are wrong.

3.8 FPGA based measurement setup

Although the Tabor-based measurement setup has been highly effective as a measurement tool in our lab, it does have some limitations. Oftentimes, the bottleneck for our measurement speed actually comes from the time it takes to upload pulse sequences from the measurement software to the Tabor itself. When this is happening, no measurements are being done, the instrument is simply communicating with the measurement software. Additionally, the Tabor only has four fully programmable outputs. Since we use IQ mixers for pulse shaping, this means we can only have complete control over two different input signals without making the measurement circuit unnecessarily complicated. Another complication in this measurement setup is that as we tune the qubit frequency, we must update the frequency of the local oscillator for the qubit signal, leading to changes in optimal parameters for the signals $I(t)$ and $Q(t)$ on the Tabor output. This means that as we tune the qubit frequency, the IQ mixers can become "unbalanced" leading to significant spectral components at frequencies *other* than ω_q within the input signal. To improve the existing qubit measurement setup in our lab, we have recently switched measurement hardware to an experimental setup using a Field Programmable Gate Array (FPGA) board (Xilinx Zynq UltraScale+ RFSoC ZCU216) running the open-source Quantum Information and Control Kit (QICK) software [147]. We often refer to this new measurement setup simply as "the QICK board". Although all of the experiments presented in this thesis were performed using the Tabor-based measurement circuit, the remainder of this section serves as a brief summary of the new measurement system, which will be used moving forward.

The QICK board minimizes the need for extra equipment such as IQ mixers or an external clock to synchronize multiple instruments in the experimental setup. The board is

equipped with 16 digital-to-analog converter (DAC) ports with a maximum sampling rate of 9.85 GS/s (almost an order of magnitude faster than the Tabor). Additionally, the board has 16 analog-to-digital (ADC) ports, with a maximum sampling rate of 2.5 GS/s. Due to this lower sampling rate on the ADC side of the board, we cannot reliably measure signals at the cavity frequency (approximately 5 GHz) directly. In order to make sure that we can impart information about the qubit state onto a much lower frequency signal, we use a standard double balanced mixer (Minicircuits ZMX-10G+) to mix a low phase noise LO signal (generated via a SignalCore SC5511A CW microwave source) with a low-frequency pulse synthesized from a DAC port on the QICK board (we typically use pulses with frequency $\omega_{\mathrm{DAC}}/(2\pi) = 150$ MHz again, although this choice of frequency is simply due to habit from the previous measurement setup). The frequency of the mixer output is then ensured to be at the cavity frequency by correctly detuning the frequency of the LO signal from the cavity frequency such that $\omega_c = \omega_{\mathrm{LO}} \pm \omega_{\mathrm{DAC}}$. Note that the mixer will produce signals at two frequencies, we typically use a standard band-pass filter from Miniciruits to ensure that we filter out one sideband and only send signals at the frequency ω_c into the cavity. Conveniently, since the DAC ports have a maximum sampling rate near 10 GS/s, we directly synthesize the qubit drive tones on the board, apply the appropriate band-pass filters and amplification, and send the signal into the cryostat. A huge advantage for this measurement setup is that the phase of the qubit signal is controlled via the software communicating with the QICK board, negating the need for IQ mixers to set the phase of the qubit (or cavity) drive signals. The output signal from the cryostat is then filtered, amplified, and mixed with the same LO signal to ensure that the input to the measurement (ADC) port on the board can be referenced to the signal applied via the DAC port. Fig. 3.9 shows an image of this measurement setup, and Ref. [147] provides a detailed description of the microwave circuitry.

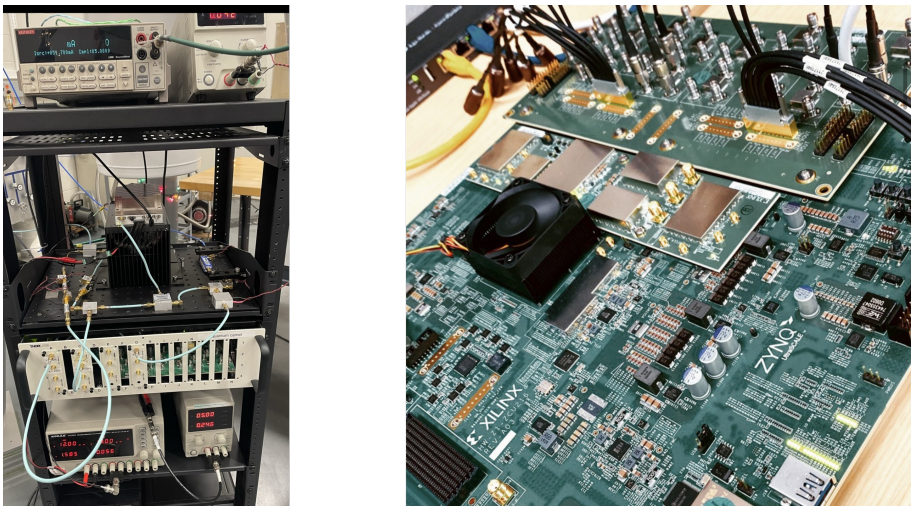

Figure 3.9: Left: Image of the FPGA-based measurement setup. The QICK board is housed within a rack-mounted drawer from Thorlabs and the relevant microwave circuitry is assembled on the optical breadboard above. Right: Close-up image of the FPGA board itself. The relevant microwave input-output signals attach to the baluns on the upper part of the image.

Chapter 4

Surface Acoustic Wave Devices

Creating resonant structures for elastic waves on the surface of, and within the bulk of, piezoelectric materials is a key concept that runs throughout much of this thesis. Mechanical excitations of various forms have been shown to couple to superconducting circuits [9] including bulk [3,28,52,59,148–152] and surface phonons [8,15,16,22–24,26,29,57,153–155], as well as phonons constrained to reside within engineered defects [21,32–36,49,50,68,156–158]. This chapter begins with the fundamental notions of stress and strain within a material and derives the solution for elastic waves from these principles. We then construct a resonant structure out of piezoelectric surface acoustic waves (SAWs) and use a numerical modeling technique known as *coupling of modes* to design the spectral features of SAW resonators to the level of high precision needed for the hybrid quantum acoustic devices studied in subsequent chapters.

4.1 Stress and strain in solids

This discussion is inspired by the excellent Refs. [122,159–161], which discuss both classical and quantum applications of SAW resonators. Elastic waves within the bulk, and on the surface, of materials have two important quantities, *stress* and *strain*. We begin by considering a material consisting of many "particles" (these particles aren't necessarily atoms, but rather volumetric fractions of the composite material that are much smaller than all other

more macroscopic length scales of the material). Then the displacement, $\vec{u}$, of each particle from its equilibrium position is determined by the components of the strain tensor S_{ij}:

$$S_{ij}(\vec{x}) = \frac{1}{2}\left(\frac{\partial u_i}{\partial x_j} + \frac{\partial u_j}{\partial x_i}\right). \tag{4.1}$$

For a three dimensional space, the strain tensor can be represented as a 3×3 matrix. However, Eqn. 4.1 is unchanged under the exchange of the indices i and j, indicating that the matrix representation of the strain tensor is symmetric, constraining the number of independent matrix elements from nine to six.

In order to describe the internal forces in a material subjected to some amount of strain, we introduce the components of the stress tensor T_{ij}. The force in the i^{th} direction per unit area on a plane with corresponding normal vector $\hat{n}$ is given by:

$$F_i = T_{ij} n_j, \tag{4.2}$$

where we have introduced the Einstein summation notation and implicitly suppressed the summation over the index j. This notation will be used for the remainder of this chapter. Similar to the strain tensor in Eqn. 4.1, it may be shown that the stress tensor is also symmetric under exchange of indices, $T_{ij} = T_{ji}$. If the stress is sufficiently small, a deformed material will return to its equilibrium state once the deforming force is removed. This is the definition for the *elastic* response of a material. This is reminiscent of a damped spring mass system, and we can therefore think of a generalization of Hooke's Law that relates stress and strain:

$$T_{ij} = c_{ijkl} S_{kl}, \tag{4.3}$$

where c_{ijkl} is a component of the fourth-rank *stiffness tensor*. The stiffness tensor, with all symmetries and thermodynamic constraints considered, consists of 21 independent entries [159]. Depending on additional symmetries of a material, it is possible to further constrain the number of independent entries in the stiffness tensor (down to as few as two for isotropic materials) [159].

Having introduced both the notion of stress and strain (or equivalently, internal forces and displacements within a material), we turn our attention to the equation of motion for a particle within the material. Assuming that the particle is well-approximated by a cube with characteristic side length δ and mass density ρ, one may calculate the net force on the particle in the i^{th} direction as [159]:

$$F_i = \delta^3 \frac{\partial T_{ij}}{\partial x_j}. \tag{4.4}$$

This net force is related to the acceleration of the particle in the i^{th} direction ($\partial^2 u_i / \partial t^2$) via Newton's Second Law:

$$\rho \frac{\partial^2 u_i}{\partial t^2} = \frac{\partial T_{ij}}{\partial x_j}, \tag{4.5}$$

giving an equation of motion for the particle in terms of the stress, which is related to the strain via Eqn. 4.3.

4.2 Two types of waves: transverse and longitudinal

As mentioned in Section 4.1, the simplest physical geometry of a material (an isotropic material) corresponds to a stiffness tensor with two independent entries. For this type of

material, we can write the stiffness tensor as [162]:

$$c_{ijkl} = \lambda\delta_{ij}\delta_{kl} + \mu\left(\delta_{ik}\delta_{jl} + \delta_{il}\delta_{jk}\right), \tag{4.6}$$

where the Kronecker delta has the important properties $\delta_{ij} = 1$ for $i = j$ and $\delta_{ij} = 0$ for $i \neq j$. Additionally, we have introduced the two positive constants λ and μ, called the Lamé constants, which are related to the elastic moduli of the material [163]. We insert Eqn. 4.6 into Eqn. 4.3 to write the stress tensor as

$$T_{ij} = \lambda\delta_{ij}\Delta + 2\mu S_{ij}, \tag{4.7}$$

where we have simplified the diagonal elements of the strain tensor as:

$$\Delta \equiv S_{ii} = \frac{\partial u_i}{\partial x_i}. \tag{4.8}$$

Furthermore, this allows us to write the equation of motion for our particle (Eqn. 4.5) as:

$$\rho\frac{\partial^2 u_i}{\partial t^2} = (\lambda + \mu)\frac{\partial\Delta}{\partial x_i} + \mu\nabla^2 u_i, \tag{4.9}$$

where $\nabla^2 = \frac{\partial^2}{\partial x_i^2}$.

At this point, our goal is to find solutions to Eqn. 4.9. A good ansatz is plane waves with angular frequency ω and wavevector $\vec{k}$:

$$\vec{u}(\vec{x}, t) = \vec{u}_0 \exp[i\left(\omega t - \vec{k}\cdot\vec{x}\right)], \tag{4.10}$$

where the physical displacement of the particle is related to $\mathrm{Re}\left(\vec{u}\left(\vec{x},t\right)\right)$. Each time derivative of Eqn. 4.10 provides a facor of $i\omega$, while spatial derivatives provide factors of $-ik_j$. Plugging our ansatz into Eqn. 4.9 and simplifying for the equation of motion for the vector $\vec{u}_0$, we arrive at:

$$\omega^2\rho\vec{u}_0 = (\lambda+\mu)\left(\vec{k}\cdot\vec{u}_0\right)\vec{k} + \mu|\vec{k}|^2\vec{u}_0. \tag{4.11}$$

There are two interesting classes of solutions to Eqn. 4.11. The first solution refers to waves which satisfy $\vec{u}\cdot\vec{k}=0$, indicating that the polarization of the wave is perpendicular to its propagation. These types of waves are referred to as *transverse* or shear waves. The second class of solutions corresponds to the polarization and propagation vectors being parallel, and are called *longitudinal* waves.

For transverse waves, Eqn. 4.11, simplifies to:

$$\omega^2\rho\vec{u}_0 = \mu|\vec{k}_t|^2\vec{u}_0, \tag{4.12}$$

which relates the wavevector for transverse waves, $\vec{k}_t$, to the material properties

$$|\vec{k}_t|^2 = \frac{\rho\omega^2}{\mu}, \tag{4.13}$$

and the corresponding wave velocity is given by: $v_t = \sqrt{\mu/\rho}$. This allows us to rewrite Eqn. 4.9 for transverse waves as:

$$\ddot{\vec{u}}_t = v_t^2\nabla^2\vec{u}_t. \tag{4.14}$$

Since we used the fact that $\vec{u}\cdot k = 0$ for transverse waves, we know that they will satisfy $\vec{\nabla}\cdot\vec{u}_t = 0$.

In the case of a longitudinal wave, Eqn. 4.11 can be rewritten as:

$$\omega^2 \rho \vec{u}_0 = (\lambda + 2\mu) \, |\vec{k}_l|^2 \vec{u}_0, \tag{4.15}$$

indicating that we can write the wavevector for longitudinal waves as

$$|\vec{k}_l|^2 = \frac{\rho \omega^2}{\lambda + 2\mu}, \tag{4.16}$$

with corresponding longitudinal wave velocity $v_l = \sqrt{\lambda + 2\mu/\rho}$. Similar to Eqn. 4.14, we can write down a wave equation for longitudinal waves in terms of their velocity:

$$\ddot{\vec{u}}_l = v_l^2 \nabla^2 \vec{u}_l. \tag{4.17}$$

Since for longitudinal waves the polarization and propagation are parallel, longitudinal waves satisfy $\vec{\nabla} \times \vec{u}_l = 0$. Recall that the Lamé coefficients are defined as positive parameters, indicating that the velocity of longitudinal waves is greater than the velocity of transverse waves.

4.3 Surface waves

We now turn our attention to surface waves and this section follows a treatment based on Refs. [159, 164]. Section 4.2 focused on elastic waves in an infinite bulk medium. In this section, we focus on the surface elastic waves important for most of the results in this thesis. Rayleigh waves (also often called surface acoustic waves or SAWs) are named after Lord Rayleigh [165] and propagate on the surface of a substrate, constraining the wave equation

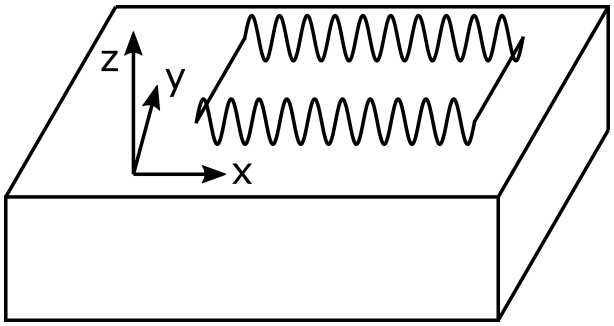

Figure 4.1: Schematic of a surface acoustic wave on the plane $z = 0$ at the surface of a semi-infinite medium. The SAW propagation and wave vector are parallel to the x-axis. The wave properties are invarant along the y-axis. The medium is defined as the volume with $z < 0$ with vacuum filling the volume $z > 0$.

that governs particle displacement. We begin by considering a medium that is infinite in two dimensions and half-infinite in the third direction (see Fig. 4.1). For the purpose this derivation, we consider a wave propagating parallel to the x-axis. The wave equation that dictates the particle displacement is given by Eqn. 4.9, and the presence of the surface of the medium imposes the boundary condition that there are no forces at the plane where $z = 0$. Since the wave properties depend on both x (direction of propagation) and z (enforces the boundary condition), the (x,z) plane is quite important and is referred to as the *sagittal plane*.

We find surface waves that satisfy Eqn. 4.9 by considering linear combinations of longitudinal and transverse waves as discussed in Section 4.2. Since we are seeking a solution constrained to the surface of the material, the solution should decay into the bulk. Additionally, we will assume that the material has translational symmetry along the y-direction, and so the solution should be independent of the y-coordinate, imposing the constraint $\frac{\partial \vec{u}}{\partial y} = 0$. We are seeking a wave with a single frequency component that propagates along x, which means that both the longitudinal and transverse components of our solution should also propagate along x. The assumptions listed above allow us to use the following ansatz for a

solution for each wave component:

$$|\vec{u}| = e^{i(\beta x - \omega t)}\ f(z), \tag{4.18}$$

where β is the wave number and ω is the angular frequency of the wave. The function $f(z)$ will depend on the polarization (transverse versus longitudinal) and dictates how the wave will decay into the bulk. Inserting Eqn. 4.18 into the corresponding wave equation (Eqn. 4.14 for transverse waves or Eqn. 4.17 for longitudinal waves) we find the following differential equation for $f(z)$ for both types of waves:

$$\frac{d^2 f}{dz^2} = \left(\beta^2 - \frac{\omega^2}{v_{l,t}^2}\right) f. \tag{4.19}$$

Since the wave needs to decay into the bulk of the material, we require $\beta^2 - \omega^2/v_{l,t}^2 > 0$. If we did not impose this constraint, the solutions for $f(z)$ would be oscillate within the bulk, which is nonphysical for surface waves. Solutions to Eqn. 4.19 then take the form:

$$f(z) \propto \exp\left(\pm z\sqrt{\left(\beta^2 - \frac{\omega^2}{c^2}\right)}\right). \tag{4.20}$$

The next question we must answer is which of the two solutions in Eqn. 4.20 to choose. If we were to choose the solution with the minus sign, the magnitude of $f(z)$ would increase as $z \to -\infty$. This would *not* correspond to a wave decaying into the bulk, so we must take the solution with the plus sign. In order to simplify the solution for the displacement, we follow convention and introduce the damping coefficient in the z-direction as $\kappa_{l,t} = \sqrt{\beta^2 - \omega^2/v_{l,t}^2}$.

With this simplification, we can write the solution to the wave equation as:

$$|\vec{u}| \propto e^{i(\beta x - \omega t)} \exp\big[z\kappa_{l,t}\big]. \tag{4.21}$$

Recall that at the beginning of this section, we said that we were seeking a solution that is a combination of longitudinal and transverse waves. At this point, we can take Eqn. 4.20 and determine the correct linear combination of transverse and longitudinal waves. We use the fact that longitudinal waves satisfy $\vec{\nabla} \times \vec{u}_l = 0$, so if the wave has no component in the y-direction this simplifies to $\frac{\partial}{\partial z}\ u_{l,x} - \frac{\partial}{\partial x}\ u_{l,z} = 0$. We insert Eqn. 4.20 into this expression to find:

$$\kappa_l u_{l,x} - i\beta u_{l,z} = 0, \tag{4.22}$$

where we have used the damping coefficient corresponding to the longitudinal wave velocity $\kappa_l = \sqrt{\beta^2 - \omega^2/v_l^2}$. We identify solutions to Eqn. 4.22 (up to the overall wave amplitude A) as:

$$\vec{u}_l = A\left(\beta\hat{x} - i\kappa_l\hat{z}\right) e^{-i(\omega t - \beta x) + \kappa_l z}. \tag{4.23}$$

To investigate the transverse component of the wave, we recall that for transverse waves $\vec{\nabla} \cdot \vec{u}_t = 0$. For a wave invariant along y, this simplifies to $\frac{\partial}{\partial x}u_{t,x} + \frac{\partial}{\partial z}u_{t,z} = 0$. Inserting Eqn. 4.20 yields the following equation:

$$i\beta u_{t,x} + \kappa_t u_{t,z} = 0, \tag{4.24}$$

where we have used the damping coefficient corresponding to the transverse wave velocity

$\kappa_t = \sqrt{\beta^2 - \omega^2/v_t^2}$. Solving Eqn. 4.24 gives the transverse wave component as:

$$\vec{u}_t = B\left(\kappa_t \hat{x} - i\beta\hat{z}\right) e^{-i(\omega t - \beta x) + \kappa_t z}, \tag{4.25}$$

again with an overall wave amplitude B. Now that we have an expression for both the longitudinal and transverse wave components, we are able to take the boundary conditions into consideration. Since the medium ends at $z = 0$, the boundary conditions require that the stress at $z = 0$ must be equal to zero. We can relate the spatial derivatives to the stress via Eqn. 4.7 and find three differential equations for $\vec{u}$ from this boundary condition:

$$T_{xz}|_{z=0} = \frac{\partial u_x}{\partial z} + \frac{\partial u_z}{\partial z} = 0, \tag{4.26}$$

$$T_{yz}|_{z=0} = \frac{\partial u_y}{\partial z} + \frac{\partial u_z}{\partial y} = 0, \tag{4.27}$$

$$T_{zz}|_{z=0} = v_l^2 \frac{\partial u_z}{\partial z} + \left(v_l^2 - 2v_t^2\right) \frac{\partial u_x}{\partial x} = 0. \tag{4.28}$$

Since the solutions for $\vec{u}$ are independent of y, we have excluded the y-dependence in Eqn. 4.27. The total solution for $\vec{u}$ is then $\vec{u} = \vec{u}_l + \vec{u}_t$ as defined in Eqn. 4.23 and and Eqn. 4.25 for longitudinal and transverse waves, respectively. Simplifying the differential equations (Eqns. 4.26, 4.27, and 4.28) yields the following set of linear equations for the overall amplitudes A and B:

$$\begin{aligned} A\left(2\beta\kappa_l\right) + B\left(\kappa_t^2 + \beta^2\right) &= 0 \\ A\left(\kappa_l^2 + \beta^2\right) + B\left(2\beta\kappa_t\right) &= 0. \end{aligned} \tag{4.29}$$

We solve Eqn. 4.29 by creating a matrix of the coefficients A and B and setting its determi-

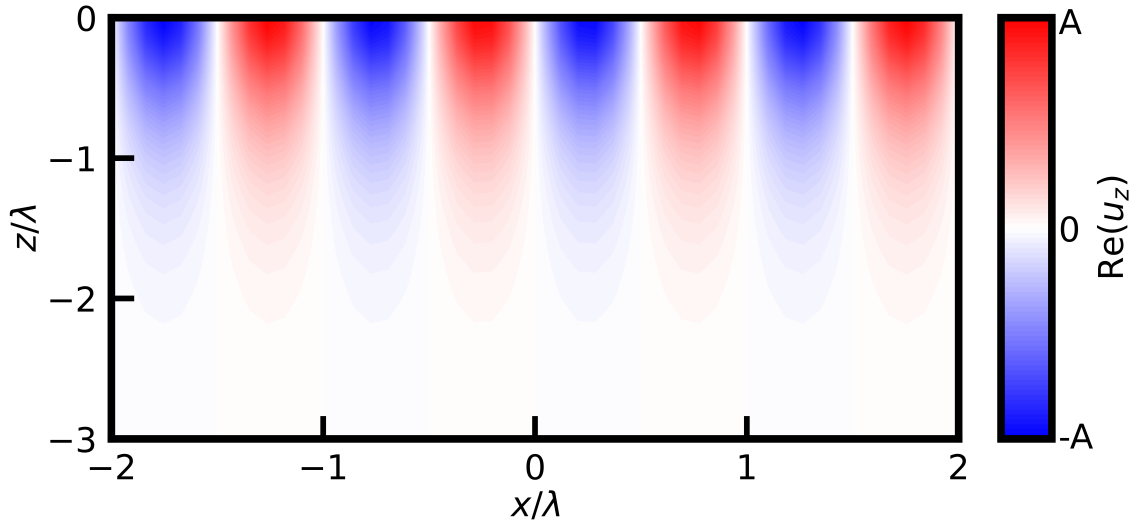

Figure 4.2: Real part of the z-component of the displacement field $\mathrm{Re}(u_z(\vec{r}))$ for $v_l^2 = 2v_t^2$. Both the x and z-axes are normalized by the SAW wavelength λ.

nant to zero. After a tremendous effort, we arrive at:

$$\left(2 - \frac{v^2}{v_l^2}\right)^2 = 4\sqrt{1 - \frac{v^2}{v_t^2}}\sqrt{1 - \frac{v^2}{v_l^2}}, \tag{4.30}$$

where we have introduced the SAW velocity as $v = \omega/\beta$. In order to gain some insight regarding Eqn. 4.30, we rescale the SAW velocity relative to the transverse wave velocity as $v = \xi v_t$, and simplify Eqn. 4.30 as:

$$\left(2 - \xi^2\right)^2 = 4\sqrt{1 - \xi^2}\sqrt{1 - \xi^2\left(\frac{v_t}{v_l}\right)^2}. \tag{4.31}$$

Importantly, Eqn. 4.31 indicates that the SAW velocity is *independent* of its frequency, it only depends on the quantity v_t/v_l. Eqn. 4.31 can be solved numerically for ξ given the ratio v_t/v_l, and is often within the range $\xi \approx 0.875 - 0.955$ based on realistic material parameters [122]. Additionally, we are able to solve for the ratio of the overall amplitudes A and B of longitudinal and transverse waves, respectively as $B/A = \left(\xi^2 - 2\right) / \left(2\sqrt{1 - \xi^2}\right)$.

Furthermore, one can inspect the total solution for SAW waves based on Eqns. 4.23 and 4.25 and identify a relative phase difference between the $\hat{x}$ and $\hat{z}$-components of the wave, indicating that the individual "particles" follow elliptical displacement paths, as displayed in Fig. 4.2.

4.4 Piezoelectric surface waves

Now that we have built a general understanding of how surface waves behave, we turn our attention to a more complicated form of Rayleigh waves - namely piezoelectric surface acoustic waves. In a piezoelectric medium, the underlying crystalline inversion symmetry is broken, and the presence of an external electric field can generate strain in the material and vice versa. In a medium that does not support piezoelectricity, the electric displacement field $\vec{D}$ in the medium is related to the electric field $\vec{E}$ via the well known relation $\vec{D} = \epsilon\vec{E}$, where ϵ is the dielectric tensor. Additionally, we can relate the stress and strain in a non-peizoelectric medium (Eqn. 4.3) via the stiffness tensor. However, if the material is piezoelectric, the relation for both the electric and strain fields are modified [166]:

$$D_i = \epsilon_{ij}E_j + e_{ijk}S_{jk} \tag{4.32}$$

$$T_{ij} = c_{ijkl}S_{kl} - e_{kij}E_k, \tag{4.33}$$

where e_{ijk} is component of the *piezoelectric tensor*. Similar to the treatment in the previous section, we can use Eqn. 4.32 and Eqn. 4.33 to find an equation of motion for a particle in such a material. In the case of a piezoelectric material, this equation of motion is much more

complicated than the isotropic case [159]:

$$\rho \frac{\partial^2 u_i}{\partial t^2} = e_{kij} \frac{\partial^2 \Phi}{\partial x_j \partial x_k} + c^E_{ijkl} \frac{\partial^2 u_k}{\partial x_j \partial x_l}, \tag{4.34}$$

where Φ is the electric potential and the superscript E on the stiffness tensor indicates that the electric field is held constant. In addition to the mechanical boundary conditions imposed by Eqns. 4.26, 4.27, and 4.28 we now additionally impose that (if the material is insulating) there are no free charges and thus we have an additional *electrical* condition that $\vec{\nabla} \cdot \vec{D} = 0$ throughout the medium. We can relate this boundary condition to find another differential equation for the system [159]:

$$\epsilon^S_{ij} \frac{\partial^2 \Phi}{\partial x_i \partial x_j} - e_{ijk} \frac{\partial^2 u_j}{\partial x_i \partial x_k} = 0, \tag{4.35}$$

where the superscript S on the component of the dielectric tensor indicates that the strain is held constant. Together Eqn. 4.34 and Eqn. 4.35 yield a system of four coupled differential equations for three spatial displacement components u_i as well as the electrostatic potential Φ. Although these equations can be solved analytically in some cases, a full solution is outside the scope of this thesis.

Next, we consider two special cases for the electrical surface boundary condition. If the surface of the piezoelectric medium is metallized, the electric field parallel to the surface must be zero. If the surface is not metallized, it is often assumed that there are no free charges and there will be a non-zero electric potential above the surface of the medium. In the case of a metallized surface, the acoustic wave will have a modified velocity v_m compared to the free surface velocity v_f. In order to quantify the strength of the interaction

of the acoustic wave with electrical environment we introduce the normalized velocity change $K^2 = 2\left(v_f - v_m\right) / \left(v_f\right)$. Materials with large values of K^2 are considered to be strong piezoelectrics while in weaker piezoelectric materials the value of K^2 is quite small and the interaction of the acoustic and electric fields is minimized. To provide context for this velocity shift, the primary results of this thesis utilize a particular cut of piezoelectric lithium niobate referred to as *YZ*-lithium niobate, which has a relatively large value of $K^2 = 4.5\%$, much larger than that of other commonly used piezoelectric materials such as quartz ($K^2 = 0.11\%$) or gallium arsenide ($K^2 = 0.06\%$) [167].

4.5 Construction of a SAW resonator

In order to physically construct a resonant structure for the SAW waves derived in Section 4.3, we need to understand the key ingredients for both exciting and reflecting SAW excitations. SAW resonators consist of periodic metallic structures fabricated on the surface of a piezoelectric substrate so that the electromechanical properties of the device are coupled as in Eqn. 4.32 and Eqn. 4.33. The physical periodicity of the metallic structures defines the wavelength λ of the SAW excitations. The operating frequency of the device is then given by $f = v/\lambda$, where v is the speed of sound on the surface of the substrate. We use the well-known coupling of modes (COM) technique [159] to numerically calculate the response of each component of the device as well as the response of the composite resonator as a whole. By defining both fabrication and material parameters for the device and substrate and using the COM modeling method, we are able to calculate the electromechanical properties of the device or its constituent parts. This section will be broken into three subsections; the first will describe the "P-matrix" techniques that are required for COM analysis, the second part

will describe the modeling techniques we use for acoustic transducers, and the final subsection will describe how we model the Bragg mirrors that form the effective reflecting walls of the acoustic cavities.

4.5.1 Coupling of modes and the P-matrix

We use the the standard P-matrix approach to model SAW devices [159]. A P-matrix for a SAW device is a 3×3 matrix that represents an acoustic structure comprised of two acoustic ports ($A_{i,j}$) and one electrical port (I, V). In this picture each acoustic port represents either left or right moving acoustic waves. We can then write down the P-matrix as:

$$\begin{pmatrix} A_{1,\text{out}} \\ A_{2,\text{out}} \\ I \end{pmatrix} = \begin{pmatrix} P_{11} & P_{12} & P_{13} \\ P_{21} & P_{22} & P_{23} \\ P_{31} & P_{32} & P_{33} \end{pmatrix} \begin{pmatrix} A_{1,\text{in}} \\ A_{2,\text{in}} \\ V \end{pmatrix} \tag{4.36}$$

The matrix elements relating the two acoustic ports (port 1 and port 2) contains information about how incoming and outgoing acoustic waves are scattered off of the structure and can be thought of in very close analogy to the scattering matrix S of a microwave circuit. If the structure is "passive" (meaning there are no electrical connections) matrix elements relating port 1 and port 2 are the only non-zero matrix elements of the P-matrix. Bragg mirrors and empty surfaces are passive elements in this fashion. The P-matrix element P_{11} relates the incoming and outgoing mechanical waves from port 1 and is therefore often the relevant P-matrix element that identifies reflecting properties.

To understand the electrical properties of a given SAW structure, we turn our attention to the P_{33} matrix element. If we consider the case where there are no incoming surface waves,

we can relate the current to the voltage via $I = P_{33}V$. This relationship allows us to identify the matrix element P_{33} as the *electrical admittance*, $Y(\omega)$, of the resonator. The real part of this quantity is the conductance $G(\omega)$, while the imaginary part gives the susceptance $B(\omega)$. Additionally, reciprocity leads to several more relations between elements of the P-matrix:

$$P_{21} = P_{12} \tag{4.37}$$

$$P_{31} = -2P_{13} \tag{4.38}$$

$$P_{32} = -2P_{23}. \tag{4.39}$$

As will be described in the following sections, SAW resonators are comprised of three key components. Firstly, acoustic transducers are responsible for converting electrical excitations to mechanical excitations and vice versa. This indicates that for these structures the primary P-matrix element of interest will be P_{33}. Second, Bragg mirrors are responsible for the reflection of acoustic excitations, and therefore for mirror structures we will primarily be interested in the quantity P_{11} (the P_{22} matrix element would also suffice, since for symmetric resonators we would expect $P_{11} = P_{22}$). Finally, free propagation space between components of a resonator will allow for an increased effective acoustic cavity length, decreasing the free spectral range of the resonator and allowing us to design the number of resonant modes the device hosts. The primary advantage of utilizing this type of modeling is that it allows us to calculate the P-matrix for a given structure and *cascade* many structures together to calculate the P-matrix for the composite device using a method known as *coupling of modes*. This method is similar to the *ABCD* matrix multiplication method for 2-port microwave systems [168], although the transduction between electrical and mechanical signals makes the calculations relatively more complicated. A complete description of this procedure can

be found in Ref. [159] (specifically Appendix D). Since finding analytic solutions for complicated acoustic resonators can prove to be a tedious calculation, it is convenient to use numeric methods [122]. The remainder of this chapter will focus on the device parameters and subsequent considerations one needs to take into account when modeling an acoustic resonator. We will build a "toy resonator" on YZ-lithium niobate as an example. By varying the parameters of the device we will see how the electrical response of the resonator changes. The relevant material properties of the resonator are listed in Table 4.1, and can be found in Ref. [167].

Parameter	Physical quantity	Value
v_{sound}	Speed of sound (at room temperature)	3488 m/s
K^2	Piezoelectric Coupling Coefficient	4.5%

Table 4.1: Summary of material parameters for a SAW resonator on YZ-lithium niobate

4.5.2 Interdigitated transducers

Before using P-matrix techniques to identify the admittance of an acoustic interdigitated transducer (IDT), we will construct a minimal model that allows us to gain some qualitative understanding of important properties of these structures, which are used to excite SAWs. Let's begin by considering a physical model of a transducer as a linear array of metal strips with spatial periodicity λ along the x-direction having a voltage on each strip that alternates between $+1$ (in some normalized voltage unit) and ground, i.e. $V = 0$ (see Fig. 4.3). For the purposes of this model, each metal strip of the IDT will be considered to be infinitely thin and infinite along the y-direction. We can then write down the total voltage profile as

a sum of delta functions spaced along the x-direction:

$$V \propto \sum_{n=0}^{N_p-1} \delta\left(x - \lambda n\right), \tag{4.40}$$

where N_p is the number of finger pairs in the transducer. The upper bound of the sum only runs to $N_p - 1$ rather than N_p because we choose to start the sum at $n = 0$ rather than $n = 1$. We Fourier transform Eqn. 4.40 to identify the wavevector response for this system (also called the *transfer function*):

$$H(k) \propto \sum_{n=0}^{N_p-1} e^{-i\lambda k n} = \frac{\sin\left(N_p k\lambda/2\right)}{\sin\left(k\lambda/2\right)} e^{-i(N_p-1)k\lambda/2}. \tag{4.41}$$

Where we have summed the geometric series $\sum_{n=0}^{N-1} x^n = \left(1 - x^N\right)/\left(1 - x\right)$. Additionally, the wavevector is related to the speed of sound $k = 2\pi f/v_s$. Furthermore, the transducer will have a central frequency f_0 related to the speed of sound and the periodicity of the structure $f_0 = v_s/\lambda$. Near f_0, we use the approximation $\sin(k\lambda/2) \simeq k\lambda/2$. These relations and approximation allow us to write down the transfer function for the IDT model as a "sinc" function centered around the frequency f_0:

$$H(f) \simeq N_p |\mathrm{sinc}\left(N_p \pi (f - f_0)/f_0\right)|, \tag{4.42}$$

where $\mathrm{sinc}(x) \equiv \sin(x)/x$. In order to study the electrical properties of a transducer, we consider its total frequency-dependent admittance:

$$Y(\omega) = i\omega C + Y_a(\omega), \tag{4.43}$$

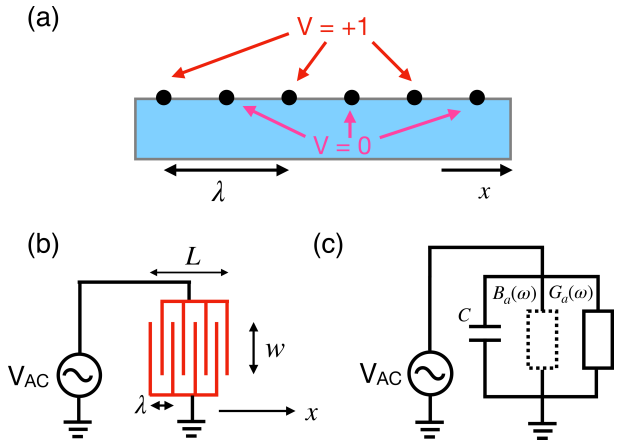

Figure 4.3: (a) Minimal model of an acoustic transducer. Alternating electrodes are biased at $V = +1$ relative to ground. The spatial periodicity of the electrodes is λ. In this geometry the surface acoustic wave will propagate along the x-direction. (b) Schematic of the circuit representation of an acoustic transducer. An alternating voltage is biased across the IDT relative to ground to excite SAWs. The width of the SAW beam is given as w and the length of the transducer is L. (c) Schematic of the same circuit with the IDT represented as three parallel circuit elements. The geometric capacitance of the structure is C, and the electromechanical response of the transducer consists of a real conductance $G_a(\omega)$ and an imaginary susceptance $B_a(\omega)$.

where C is the geometric capacitance of the interdigitated transducer structure and the admittance $Y_a(\omega)$ is a complex admittance describing the transduction between acoustic and electrical excitations. In the case where all of the dissipated electrical power is converted to acoustic waves, it can be shown that the real part of $Y_a(\omega)$ is related to the transfer function (Eqn. 4.42) as $\mathrm{Re}(Y_a(\omega)) \equiv G_a(\omega) \propto |H(\omega)|^2$. In addition to the real part, the admittance also contains an imaginary part [169]. Taking the full complex admittance into account, we can represent the SAW IDT as a lumped electrical circuit consisting of 3 parallel components (see Fig. 4.3(c)):

$$Y(\omega) = i\omega C + G_a(\omega) + iB_a(\omega), \tag{4.44}$$

where both the conductance and susceptance can be written as:

$$G_a(\omega) = G_{a0}\ \mathrm{sinc}^2\left(X\right) \tag{4.45}$$

$$B_a(\omega) = G_{a0}\left(\frac{\sin\left(2X\right) - 2X}{2X^2}\right) \tag{4.46}$$

$$X = \left(\frac{N_p\pi(\omega - \omega_0)}{\omega_0}\right). \tag{4.47}$$

Calculation of the prefactor G_{a0} is quite involved and leads to $G_{a0} \simeq 1.3K^2N_p^2\omega WC_p$, where the parameters K^2, N_P, W,and C_p are the piezoelectric coupling coefficient, number of finger pairs, SAW beam width, and capacitance per IDT finger pair per unit length, respectively [169].

The previous simplified model of an acoustic transducer was missing a key ingredient-namely internal reflections within the transducer structure were not taken into account. Fortunately for us, the coupling of modes method allows us to take into account these internal reflections and solve for more realistic values of $G_a(\omega)$ and $B_a(\omega)$. A representative calculation for $G_a(\omega)$ and $B_a(\omega)$ using the coupling of modes method is shown in Fig. 4.4 with $\lambda = 1\ \mu$m, $L = \ 25\mu$m, the reflection probability per finger $|r| = 2\%$, and $W = 50\ \mu$m.

We can identify some of the physical quantities that are important for the design and construction of an acoustic transducer. Fig. 4.5 displays the log-scale magnitude of the P_{33} matrix element for an IDT structure as the length L of the structure is varied (see Fig. 4.3). Moreover, as the length is increased, the periodicity of the lobes of the sinc function decrease in frequency, consistent with the prediction from Eqn. 4.45. As the length of the transducer increases, the impact of internal reflections within the IDT structure become more apparent, with the transducer response becoming heavily skewed towards lower frequencies.

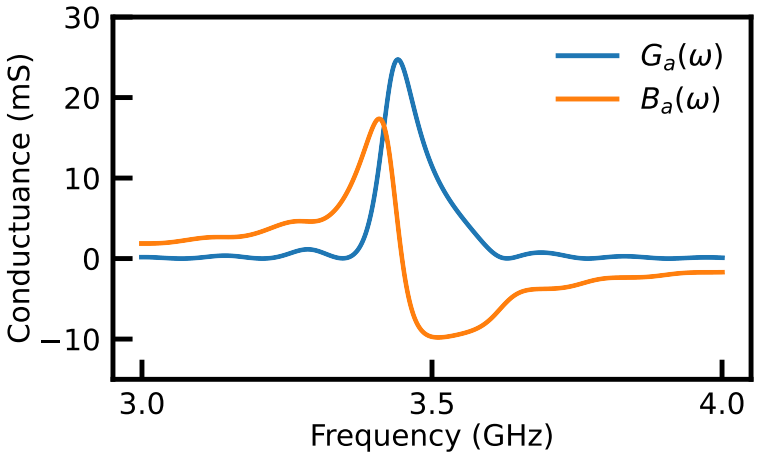

Figure 4.4: Conductance and susceptance of an IDT structure calculated using the coupling of modes method. The skew in the device resonance arises from internal reflections within the transducer ($r = 2\%$ per finger pair).

4.5.3 Bragg reflection gratings

Now that we have built a framework that allows us to design a device that transduces electrical energy into surface phonon acoustic energy, we next introduce Bragg reflection gratings. These gratings will allow for the strong reflection of phonons at certain frequencies, allowing us to construct a resonator. By fabricating many strips of metal having a spatial periodicity λ_{mirror} that are electrically disconnected from each other, we can leverage the finite reflectivity per electrode to form an acoustic "mirror" structure. Since the reflectivity per electrode is quite low (approximately 1% per electrode), we often require on the of order several hundred gratings to construct a Bragg mirror with near-unit total reflectivity. The frequency range over which SAWs are faithfully reflected is often referred to as the mirror stop-band (Δf), which is directly proportional to the reflectivity of the electrodes $\Delta f/f \approx 2|r_m|/\pi$ [159]. As described in Section 4.5.1, the relevant P-matrix quantity for a mirror structure is P_{11}. The magnitude and phase of the quantity P_{11} is displayed for a mirror structure on YZ-lithium niobate with $\lambda_{\text{mirror}} = 1.01$ μm, length $L_{\text{mirror}} = 100$ μm,

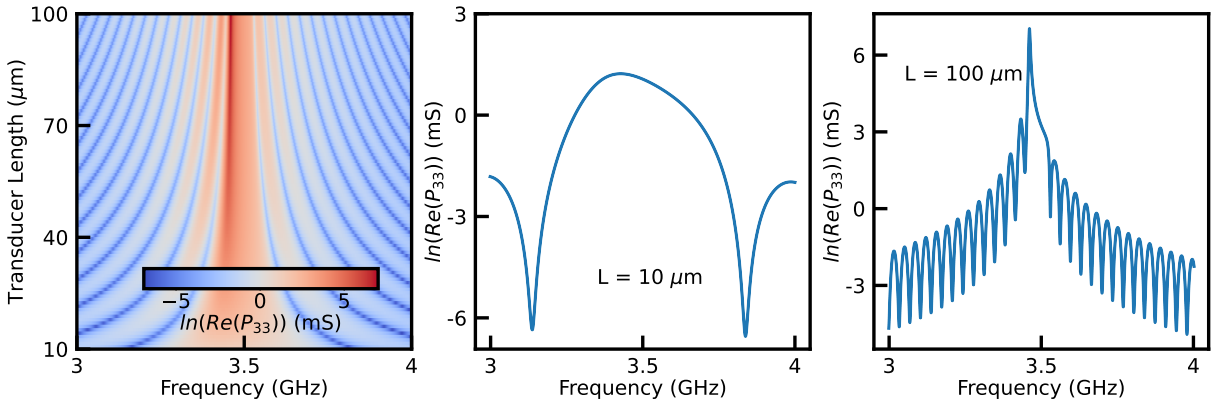

Figure 4.5: Left: Log-scale conductance of the IDT calculated with coupling of modes. As the transducer length is increased, the width of the response in frequency drastically decreases. Middle: Conductance of the transducer with a width $L = 10$ μm. The width of the central peak is of order 100 MHz. Right: Conductance of the transducer with a width $L = 100$ μm. The width of the central peak is of order 10 MHz.

and reflectivity per grating $r_m = 2\%$ is shown in Fig. 4.6. Since the stop-band width depends intimately on the reflectivity of the mirrors, it is important to study the properties of P_{11} for a mirror structure as a function of the reflectivity. As shown in Fig. 4.7, as we increase the reflectivity of the mirrors, we observe a corresponding increase in the width of the mirror stop-band. This is quite important since the reflectivity of the mirrors is not a geometrically defined quantity, but rather a somewhat difficult to control fabrication parameter of the device [170].

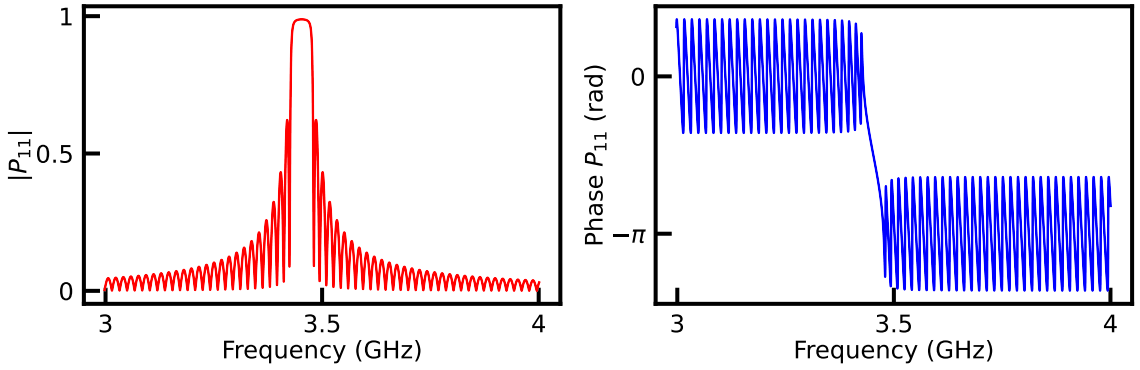

Figure 4.6: Left: amplitude of P_{11} for a SAW mirror structure. In this example, the center of the mirror stop band is near 3.45 GHz, with the reflection rapidly decaying outside of the mirror stop band. Right: phase response of P_{11} for the same mirror structure.

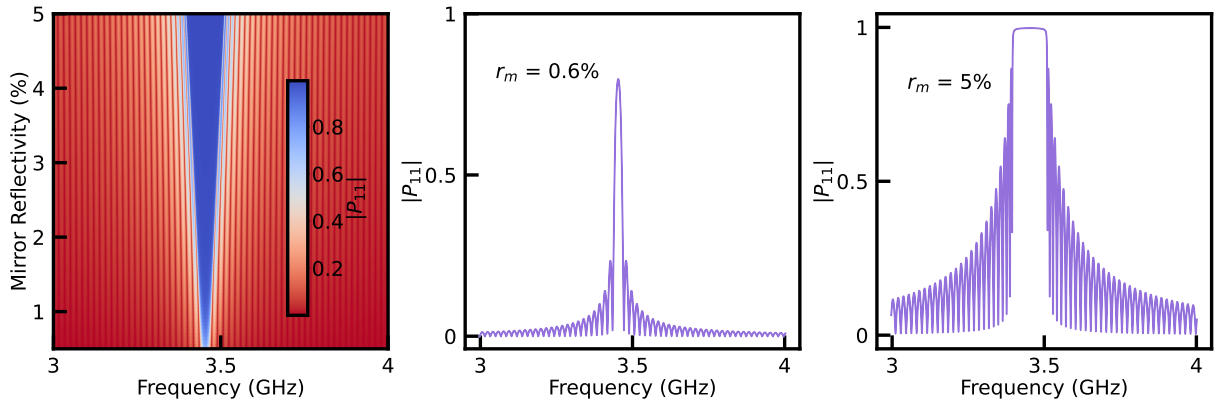

Figure 4.7: Left: Amplitude of P_{11} for the mirror structure from Fig. 4.6 with varying mirror reflectivity r_m. Center: $|P_{11}|$ with a reflectivity of $r_m = 0.6\%$. The stop-band is quite narrow, and the maximum reflectivity is significantly less than unity. Right: $|P_{11}|$ with a reflectivity of $r_m = 0.6\%$. Compared to the center panel, the mirror reflectivity is much more broad and the maximum reflectivity is near unity.

Since the spectral shape of the mirror reflectivity is quite complicated (i.e. it is not a simple boxcar function), it is often useful as thinking of the acoustic cavity as spatially distributed over the length of the mirror structure with an effective length L_{eff} as described in the following section.

4.5.4 Complete model of a SAW resonator

Now that we understand how to both excite and reflect phonons, we have the complete framework to construct a composite SAW resonator consisting of both and IDT structure surrounded by Bragg mirrors on either side so that phonons generated in the center of the device are strongly reflected by the Bragg mirrors, forming an acoustic cavity as shown in Fig. 4.8. An example calculation is done below using the pieces we have already constructed in the previous two sections. We take the response of the IDT structure in Fig. 4.4 and place it between two Bragg mirrors as seen in Fig. 4.6 with zero free propagation distance between the IDT and mirrors ($L_{\text{free}} = 0$). The total electrical conductance for this resonator

is shown in Fig. 4.8. For completeness, we also plot $|P_{11}|$ for the mirrors and $\mathrm{Re}(P_{33})$ for the IDT on the same plot to identify salient features of both the IDT and mirrors on the response of the composite resonator.

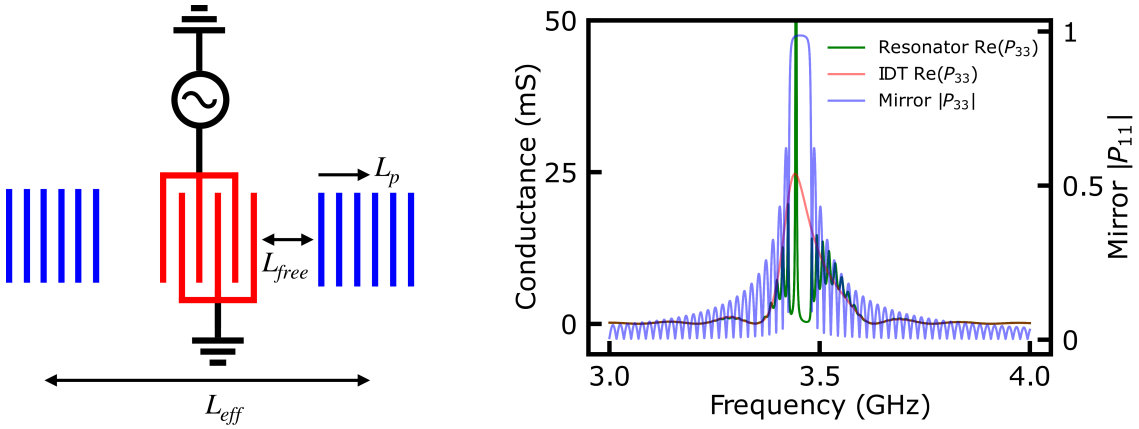

Figure 4.8: Left: geometric sketch of a complete SAW resonator. The IDT (red) is responsible for the transduction of electrical excitations into phononic excitations. The Bragg mirrors (blue) are responsible for reflecting these excitations. The free spectral range of the resonator is determined by the speed of sound as well as the effective length of the cavity $L_{\mathrm{eff}} = 2L_P + L + L_{\mathrm{free}}$. Right: Conductance for a SAW resonator calculated via coupling of modes with $L_{\mathrm{free}} = 0$. There is a single confined mode near 3.45 GHz. The peak of the IDT conductance is within the mirror stop-band, leading to an enhancement of the resonator conductance within the mirror stop-band.

The effective length of the SAW cavity is comprised of three parts. The first part is the distance (on average) waves will propagate into the mirrors. Since each grating reflects only a small percentage of the wave, one can estimate the penetration depth of the wave into the mirrors as $L_P \simeq |r_m|\lambda_{\mathrm{mirror}}/2$. The last length scale that is important in defining the total length of the effective SAW cavity is the free propagation distance between the IDT and the mirrors (see Fig. 4.8). Taking each of these parameters into account, we can estimate the effective length of the SAW cavity as $L_{\mathrm{eff}} = 2L_P + L + L_{\mathrm{free}}$, where we have included the factor of 2 to account for the mirrors on either side of the IDT.

The spacing in frequency between confined SAW modes (called the *free spectral range*) in this type of resonator is given by: $\Delta f_{FSR} = v_s/(2L_{\mathrm{eff}})$. As the free propagation distance

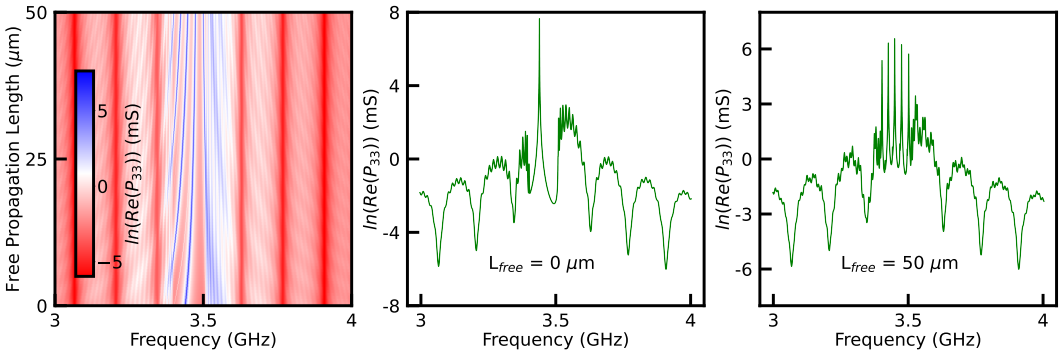

Figure 4.9: Left: Log-scale conductance of the SAW resonator in Fig. 4.8 with varying free propagation distance L_{free}. Center: resonator conductance with $L_{\text{free}} = 0$. This resonator supports a single confined surface phonon mode. Right: resonator conductance for the same SAW resonator but with $L_{\text{free}} = 50$ μm. This resonator supports five confined mechanical modes.

L_{free} is increased the free spectral range decreases. When the free spectral range becomes significantly smaller than the width of the mirror stop-band, multiple resonant modes can exist within the mirror stop band, leading to a multi-mode acoustic cavity [8, 57, 154].

In order to gain intuition for how important the free propagation distance L_{free} is for the response of the resonator, we plot $\text{Re}(P_{33})$ for the model SAW resonator from Fig. 4.8 as L_{free} is varied with all other parameters held constant. As the free propagation distance is increased, we see the device host an increasing number of resonant modes. By specifically designing L_{free} for a given resonator design, we are able to produce resonant spectra containing a custom-made number of resonant acoustic modes.

4.6 Conclusion

This chapter has focused on the design of surface acoustic waves beginning with the concept of elastic waves in a solid. By constraining the wave to the surface we have found the general structure of surface acoustic waves. We have used the coupling of modes machinery to model each constituent part of a SAW resonator and explored how the physical parameters of each

part of the resonator impact the response of individual components of the resonator as well as the composite response of the resonator as a whole. We build on these ideas in the following chapters by precisely designing the conductance of a high-frequency SAW resonator that will be used in our quantum acoustic experiments.

Chapter 5

Open Quantum Systems

5.1 Introduction

When we learn quantum mechanics for the first time, an emphasis is placed on *closed* quantum systems. What do we mean by "closed" in this context? For the purposes of this thesis, a closed quantum system is a system whose dynamics follow the rules of quantum mechanics, and the system is completely isolated from its environment. In such a closed system, the Hamiltonian ($\hat{\mathcal{H}}$) can be identified and the evolution of the wavefunction of the system $|\psi(t)\rangle$ follows the results from the Schrödinger equation depending on the initial state of the system $|\psi(0)\rangle$ and the Hamiltonian ($\hbar = 1$):

$$|\psi(t)\rangle = \exp(-i\hat{\mathcal{H}}t)\,|\psi(0)\rangle\,. \tag{5.1}$$

Note, that Eqn. 5.1 assumes that the Hamiltonian $\hat{\mathcal{H}}$ is *time-independent*. In the case of a time-dependent Hamtiltonian the solution to Schrödinger's equation becomes slightly modified:

$$|\psi(t)\rangle = T_{\leftarrow}\exp\left[-i\int_{t_0}^{t} \mathrm{d}t'\hat{\mathcal{H}}(t')\right]|\psi(0)\rangle\,, \tag{5.2}$$

where the arrow indicates that products of time-dependent operators are ordered such that their arguments in time increase from right to left.

Now let's imagine a more complicated example. Take our quantum system of interest (a qubit is actually the simplest case!), and let's try to write down the Hamiltonian that describes the qubit plus the local microwave environment plus all of the defects in the system and how strongly they couple to the qubit. What do these interactions look like at the level of the Hamiltonian? How large is the Hilbert space for this system? As one can see, this problem ranges from very difficult to highly impractical. As such, when we are interested in the evolution of a quantum system that is interacting with its environment, we need to introduce an new tool for analyzing systems that interact with many degrees of freedom. This is an example of what we consider an *open* quantum system, where the interactions between the system of interest and the environment are sufficiently strong that they cannot be ignored. For this type of system, rather than study the wavefunction $|\psi\rangle$ we need to work with the reduced density matrix ρ. As we will see in this chapter, by considering both coherent and dissipative effects in the system, we are able to construct an equation of motion for the qubit's reduced density matrix, which allows us to study the dynamics of certain types of open quantum systems.

5.2 Lindblad master equation

In this section, we present a partial derivation of the Lindblad Master Equation [72], which we will use in our analysis of open quantum systems. This section is inspired by Refs. [171–175]. We begin by considering the density matrix ρ for a quantum system. The density matrix has several important properties, listed below:

- Unit trace: $Tr(\rho) = 1$.
- Hermiticity: $\rho^\dagger = \rho$.

- Positive eigenvalues: $\lambda \geq 0 \; \forall \; \lambda$ of ρ.

The last two bullet points define the density matrix ρ to be a *positive semidefinite matrix*. The density matrix can be constructed as as a weighted sum over many different pure states of the quantum system $|\psi_i\rangle$:

$$\rho = \sum_i p_i \left|\psi_i\right\rangle \left\langle\psi_i\right| . \tag{5.3}$$

In Eqn. 5.3, the sum is over each pure state $|\psi_i\rangle$ and is weighted by the probability p_i. Note that the first bullet point listed above constrains the probabilities in Eqn. 5.3 such that $\sum p_i = 1$. The density matrix can be used to as a tool to probe the operators acting on the system via the equation $\langle\hat{O}\rangle = Tr(\rho\hat{O})$ for a given system operator $\hat{O}$. In order to see this, we consider the expansion of $Tr(\rho\hat{O})$:

$$\begin{aligned} Tr(\rho\hat{O}) &= \sum_{i,j} p_i \left\langle\psi_j\middle|\psi_i\right\rangle \left\langle\psi_i\right| \hat{O} \left|\psi_j\right\rangle , \\ &= \sum_{i,j} \delta_{i,j} p_i \left\langle\psi_i\right| \hat{O} \left|\psi_j\right\rangle , \\ &= \sum_i p_i \left\langle\psi_i\right| \hat{O} \left|\psi_i\right\rangle , \\ &= \sum_i p_i \langle\hat{O}\rangle_i = \langle\hat{O}\rangle. \end{aligned} \tag{5.4}$$

Additionally, the density matrix also informs us of the *purity* of the state via the quantity $\mathcal{P} = Tr(\rho^2)$, which will be an important metric for the open quantum systems work of chapter 7. The purity of a maximally mixed state is given by the minimum purity $\mathcal{P}_{\text{min}} = 0.5$, while the maximum state purity is given by a pure state with $\mathcal{P}_{\text{max}} = 1$. A state is called a *pure state* if it can be represented by a sum of basis states and has $\mathcal{P} = 1$, while a state is called a *mixed state* if it can only be represented by a statistical mixture of pure states [176].

In order to study how the density matrix changes in time, we consider the full Hamiltonian $\hat{\mathcal{H}}$ of a quantum system interacting with its environment:

$$\hat{\mathcal{H}} = \hat{\mathcal{H}}_S \otimes \hat{\mathbb{I}}_E + \hat{\mathbb{I}}_S \otimes \hat{\mathcal{H}}_E + \hat{\mathcal{V}}. \tag{5.5}$$

In Eqn. 5.5, the first term describes the Hamiltonian of the system as $\hat{\mathcal{H}_S}$ and the tensor product with the identity operator for the environment. The second term describes the Hamiltonian of the environment $\hat{\mathcal{H}_E}$ and the tensor product with the identity operator for the system. The third and final term represents the interaction between the quantum system and its environment. The density matrix that describes the composite interacting system is ρ_T. In order to describe the *redcued* density matrix for the system dynamics (ρ), we simply trace over the environmental degrees of freedom: $\rho = Tr_E(\rho_T)$. In the interaction picture, the equation of motion for the density matrix ρ_T is given by

$$\dot{\rho}_T = -i[\hat{\mathcal{V}}(t), \rho_T]. \tag{5.6}$$

Integrating Eqn. 5.6 and substituting the solution back into itself yields the equation:

$$\dot{\rho}_T = -\int_0^t [\hat{\mathcal{V}}(t), [\hat{\mathcal{V}}(t'), \rho_T(t')]]\ dt'. \tag{5.7}$$

We assume $Tr_E([\hat{\mathcal{V}}(t), \rho_T(0)]) = 0$ via a choice of the interaction Hamiltonian, allowing us to set the constant of integration to 0. At this point it is useful to trace over the environmental degrees of freedom in order to write an equation of motion for the reduced density matrix ρ:

$$\dot{\rho}(t) = -\int_0^t Tr_E\left([\hat{\mathcal{V}}(t), [\hat{\mathcal{V}}(t'), \rho_T(t')]]\right)\ dt'. \tag{5.8}$$

In order to further simplify Eqn. 5.8, we need to make several assumptions about the interactions between the system and the environment. By assuming that there are **no initial correlations between the system and the environment**, then $\rho_T(0) = \rho(0) \otimes \rho_E(0)$, where ρ_E is the density matrix describing the environment. Furthermore, we can make the **Born approximation** [177], assuming that the coupling between the system and its environment is weak ($|\hat{\mathcal{V}}| \ll |\hat{\mathcal{H}}_0|$) we can rewrite the total density matrix as $\rho_T(t) = \rho(t) \otimes \rho_E(t)$. Along the same lines, the Born approximation also allows us to consider the environment as a large "bath" for the system, by which we mean the **environmental dynamics do not substantially change the dynamics of the system in time**, i.e. $\rho_E(t) = \rho_E$. Furthermore, by assuming that there is **no flow of information from the environment back to the system** (the **Markov approximation**) [171] we can replace $\rho(t')$ in the integrand of Eqn. 5.8 with $\rho(t)$. Additionally, if we assume that the **system state does not change significantly on time scales relevant to the environment decay**, we can rewrite Eqn. 5.8 as:

$$\dot{\rho}(t) = -\int_0^\infty Tr_E \left([\hat{\mathcal{V}}(t), [\hat{\mathcal{V}}(t-t'), \rho(t) \otimes \rho_E]] \right) dt'. \tag{5.9}$$

Eqn. 5.9 is known as the *Markovian master equation*, and the assumptions that led us from Eqn. 5.8 to Eqn. 5.9 (highlighted in **bold text**) are known as the *Born-Markov approximations*. In order to further simplify Eqn. 5.9, we will expand Eqn. 5.9 in terms of the interaction potential, and it will be possible to further simplify the Markovian master equation into Lindblad form (see Refs. [171–174] for details), where the dynamics of the density

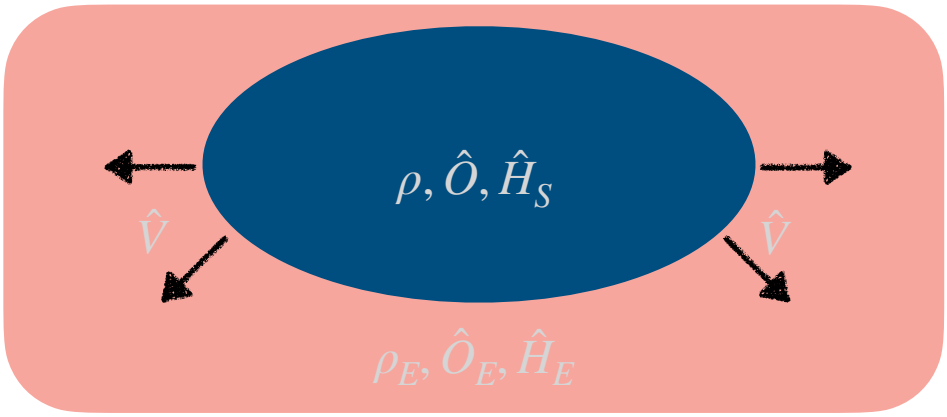

Figure 5.1: Depiction of an open quantum system. The system (blue) is described by a reduced density matrix ρ, has "system" operators $\hat{O}$, and is subject to a Hamiltonian $\hat{\mathcal{H}}$. The environment also has its own reduced density matrix, operators, and Hamiltonian $(\rho_E, \hat{O}_E, \hat{\mathcal{H}}_E)$. The goal of this chapter is to develop a framework to disentangle the two from each other so that we may study the system independent from the environment.

matrix is comprised of two primary parts:

$$\dot{\rho} = -i[\hat{\mathcal{H}}, \rho] + \sum_k \gamma_k \mathcal{D}[\hat{L}_k]. \tag{5.10}$$

In Eqn. 5.10, we have introduced the superoperator $\mathcal{D}[\hat{L}_k]\rho = \hat{L}_k \rho \hat{L}_k^\dagger - \frac{1}{2}\{\hat{L}_k^\dagger \hat{L}_k, \rho\}$ that describes dissipation in the system. Each rate γ_k provides the appropriate weight to the corresponding "jump" operators $\hat{L}_k$, which are responsible for driving the quantum system between states.

Although Eqn. 5.10 *seems* to be incredibly compact, in principle we could consider many jump operators $\hat{L}_k$. Additionally, Eqn. 5.10 describes the evolution of a *matrix*, not a single vector. In order to solve this equation for a particular system given set of jump operators, it is sometimes useful to "vectorize" Eqn. 5.10 (see Ref. [178] for more details). The remainder of this chapter will focus on providing several simple examples of solutions to Eqn. 5.10 in

order to gain some intuition for the effects of drive and dissipation on a quantum system.

5.3 Driven-dissipative qubit

Since many of the results of this thesis are important within the context of quantum two level systems, it is an extremely useful example to consider the dynamics of a qubit under the presence of drive and dissipation. We can consider the Hamiltonian of the driven-dissipative qubit as:

$$\hat{\mathcal{H}} = -\frac{\omega_q}{2}\hat{\sigma}_z + \Omega\cos(\omega_d t)\hat{\sigma}_x. \tag{5.11}$$

In Eqn. 5.11, the qubit energy splitting is given by ω_q, and the drive is parameterized by its frequency ω_d and amplitude Ω. We can transform this Hamiltonian to the frame rotating with the drive via $\hat{\mathcal{H}} \rightarrow \hat{U}\hat{\mathcal{H}}\hat{U}^\dagger + i\hat{U}^\dagger\dot{\hat{U}}$, where $\hat{U} = \exp(-\omega_d t\hat{\sigma}_z/2)$. In this frame, the Hamiltonian becomes time-independent and is therefore much easier to analyze:

$$\hat{\mathcal{H}} = \frac{\Delta}{2}\hat{\sigma}_z + \frac{\Omega}{2}\hat{\sigma}_x, \tag{5.12}$$

where we have introduced the detuning $\Delta = \omega_d - \omega_q$. In order to discuss dissipation in this system, we consider two jump operators. To describe energy relaxation, we use the operator $\hat{\sigma}_- = \hat{\sigma}_x - i\hat{\sigma}_y$, along with corresponding rate γ_1 (the subscript "1" is to indicate that this describes a T_1 process as discussed in chapter 3). To account for loss of phase information, we use the operator $\hat{\sigma}_z$ along with corresponding rate $\gamma_\phi/2$ (this follows the convention of pure dephasing as described in chapter 3). Under this type of drive and dissipation, we can

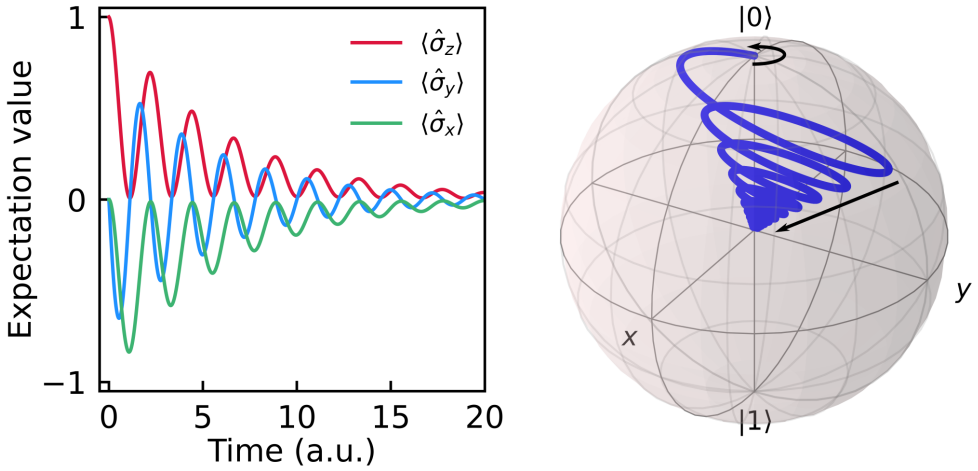

Figure 5.2: Left: Tomography components of a driven-dissipative qubit. Each component oscillates in time before decaying to a maximally mixed state. The trajectory of each component is set by solutions to Eqn. 5.13. Right: Bloch sphere representation of the data from the left panel.

write Eqn. 5.10 as:

$$\dot{\rho}(t) = -i\left[\frac{\Delta}{2}\hat{\sigma}_z + \frac{\Omega}{2}\hat{\sigma}_x, \rho(t)\right] + \gamma_1 \mathcal{D}[\hat{\sigma}_-] + \frac{\gamma_\phi}{2}\mathcal{D}[\hat{\sigma}_z]. \tag{5.13}$$

Since we are considering only a two-level system in this case, it is possible to solve Eqn. 5.13 analytically. However, for simplicity, we employ Qutip [179], a Python package which is optimized to find numerical solutions to the Lindblad equation. By solving Eqn. 5.13 for $\rho(t)$, we can calculate trajectories of each qubit vector component $\langle\hat{\sigma}_i\rangle$ for $i \in x, y, z$. As seen in Fig. 5.2, the qubit state vector traces out a particular path within the Bloch sphere and eventually decays to the center of the Bloch sphere. In this particular simulation, we have set $\Omega = -\Delta$ and have scaled the rates corresponding to all jump operators so that $\Omega = |\Delta| = 4\gamma$. In this parameter regime, the drive is dominant and we are able to see the qubit state vector trace out multiple oscillations before it descends to the center of the Bloch sphere as seen in Fig. 5.2.

5.4 Driven-dissipative harmonic oscillator

Although the many of the results of this thesis focus on superconducting qubits, the Lindblad master equation is useful for a variety of quantum systems. Specifically, within the context of quantum acoustics systems, it may behoove us to study the dynamics of harmonic oscillator states as described towards the end of Ch. 6. In this section we consider solutions to the Lindblad equation for a quantum harmonic oscillator. In the absence of an external drive applied to the system, we take the Hamiltonian of the oscillator to be:

$$\hat{\mathcal{H}} = \hat{a}^\dagger \hat{a}. \tag{5.14}$$

At the level of this example, we will only include two jump operators $\hat{a}$ and $\hat{a}^\dagger$. In the case of an electromagnetic oscillator (like our microwave cavities), these jump operators correspond to photon loss and photon gain, respectively. We relate the rate of each jump operator to the average population of a thermal bath, so that the rate of photon loss is given by $\gamma_- = \kappa(1 + \overline{n}_{th})$, and the rate of photon gain is given by $\gamma_+ = \kappa\overline{n}_{th}$. In this case, Eqn. 5.10 becomes:

$$\dot{\rho}(t) = -i[\hat{a}^\dagger \hat{a}, \rho(t)] + \kappa(1 + \overline{n}_{th})\mathcal{D}(\hat{a}) + \kappa\overline{n}_{th}\mathcal{D}(\hat{a}^\dagger). \tag{5.15}$$

At this point, Eqn. 5.15 looks rather intimidating to solve analytically, so we continue to utilize Qutip for numeric simulations. By initializing the oscillator state in a coherent with $\overline{n} = 4$, we can solve for the density matrix ρ at a given point in time and use it to investigate physical quantities (operator expectation values) of interest for the oscillator. For example, we can calculate quantities like the average photon number as $\overline{n} = Tr(\rho\hat{n})$, as well as the probability of having n photons in the oscillator as ρ_{nn}, as the n^{th} diagonal density matrix

element. As shown in Fig. 5.3, when the oscillator is initialized in a coherent state, the photon number distribution is Poissonian at $t = 0$ as expected [5]. In this particular we have defined the environment as a thermal bath with average energy equal to the transition energy of the harmonic oscillator. As the system interacts with its dissipative environment, the mean phonon number decays from the initial value to $\overline{n} = 1$, where the system is in thermal equilibrium with its environment, which is an external parameter we set in this particular simulation. In the presence of an external drive the system Hamiltonian now

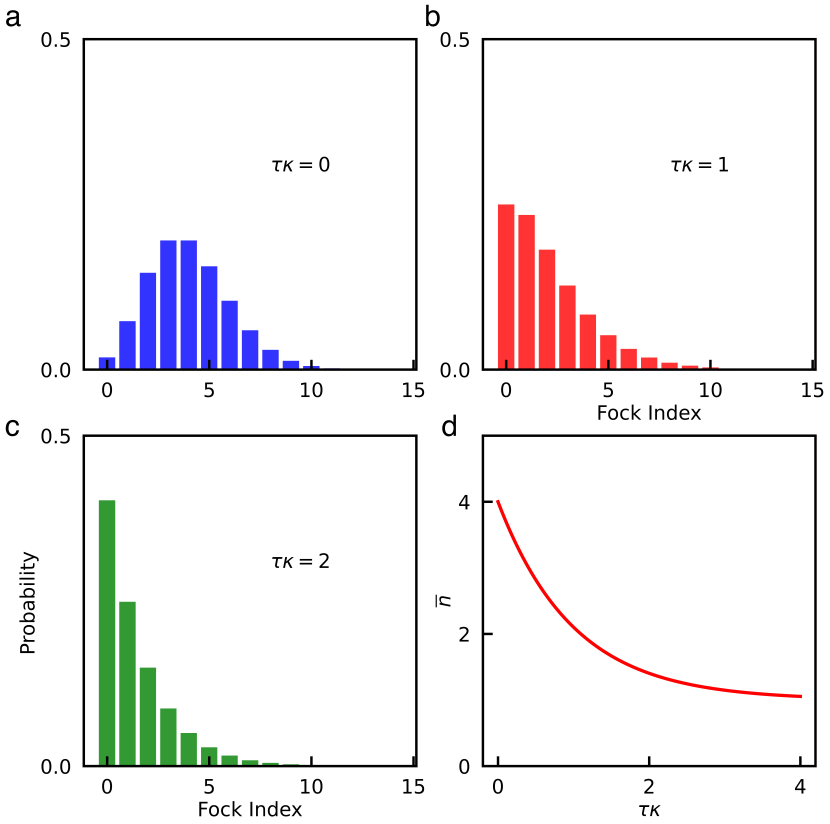

Figure 5.3: (a) Photon number distribution at $\tau\kappa = 0$, where τ is the time during which the oscillator is subject to dissipation and κ is related to the rate of the operators $\hat{a}$ and $\hat{a}^\dagger$. (b) Photon number distribution at $\tau\kappa = 1$. (c) Photon number distribution at $\tau\kappa = 2$. (d) Evolution of the average photon number $\overline{n}$ while the system is subject to dissipation.

becomes:

$$\hat{\mathcal{H}} = \hat{a}^\dagger \hat{a} + \mathcal{V}\left(\hat{a} + \hat{a}^\dagger\right), \tag{5.16}$$

where the strength of the external drive is given by $\mathcal{V}$. The term $(\hat{a}+\hat{a}^{\dagger})$ is the coordinate of the harmonic oscillator in operator form, and the external drive is reminiscent of an external force changing the coordinate of our oscillator. In the following numeric simulations, we relate the drive strength to the dissipation by setting $\mathcal{V} = \frac{3}{4}\kappa$, so that drive and dissipation are (almost) of the same magnitude. All other parameters in the simulations in Fig. 5.3 and Fig. 5.4 are the same across the two sets of simulations. In Fig. 5.4, we now see that rather than decay to the population of the thermal environment, the average number approaches a steady state with $\overline{n} > \overline{n}_{th}$ due to the presence of the drive. Additionally, the number distribution starts as a Poisson distribution as in the undriven case, but as the drive and dissipation act on the system during its evolution, the number distribution is significantly different than that in Fig. 5.3.

5.5 Conclusion

This chapter introduced the concept of an open quantum system, where interactions between a quantum system and its environment can lead to the loss of information in the quantum system. We have presented a derivation of the Lindblad master equation and used two simple examples to see how the impact of dissipation changes the system dynamics. The next chapter uses the idea of driven-dissipative systems to leverage the engineered dissipation of a superconducting qubit as a resource for quantum control.

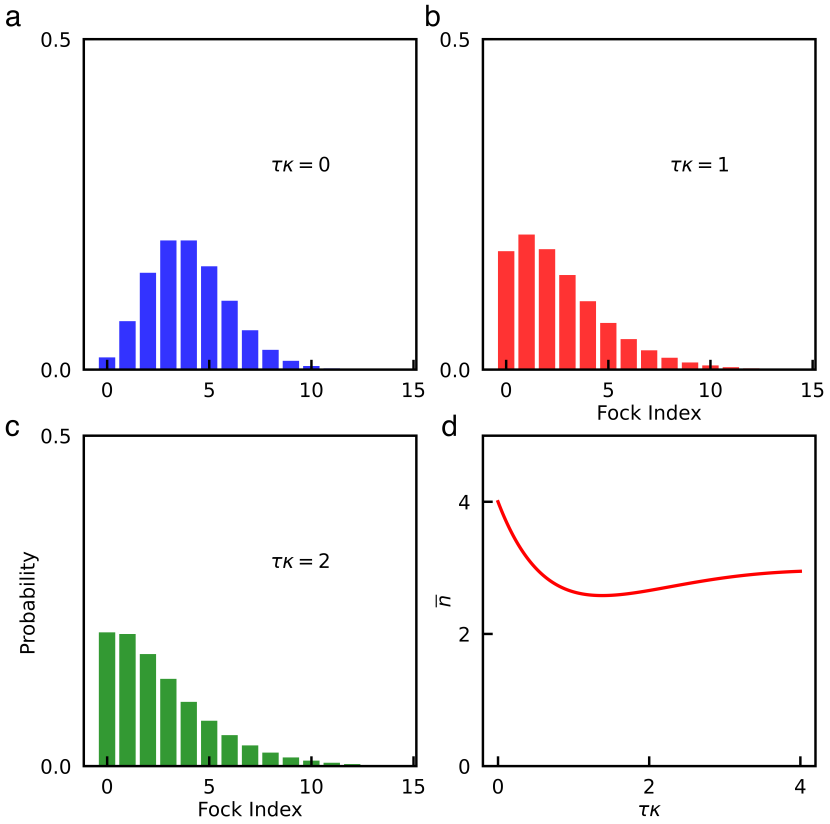

Figure 5.4: (a) Photon number distribution at $\tau\kappa = 0$, where τ is the time under which the oscillator is subject to dissipation and κ is related to the rate of the operators $\hat{a}$ and $\hat{a}^\dagger$. (b) Photon number distribution at $\tau\kappa = 1$. (c) Photon number distribution at $\tau\kappa = 2$. (d) Evolution of the average photon number $\overline{n}$ while the system is subject to both drive and dissipation.

Chapter 6

Phononic Bath Engineering of a Superconducting Qubit

6.1 Introduction

Phonons, the ubiquitous quanta of vibrational energy, play a vital role in the performance of many quantum technologies. Coupling to well-defined phonon modes allows for highly-connected multi-qubit gates in ion trap architectures [180–182] as well as the generation of entangled states in systems of superconducting qubits [24, 25]. Even when the phonons take the form of a large dissipative bath, an irreversible flow of heat allows for state initialization critical to the function of laser systems [183] and the operation of optically active spin qubits [184, 185]. Conversely, unintended coupling to phonons has been shown to degrade qubit performance by generating decohering quasiparticles and leading to correlated errors in superconducting qubit systems [186–188]. Regardless of whether a phononic bath plays an enabling or deleterious role, it is typically intrinsic to the system and does not admit specific control over its spectral properties, nor the possibility of engineering aspects of its dissipation to be used as a resource. Here we show that by precisely designing the coupling of a superconducting qubit to phononic degrees of freedom enables a novel platform for investigating the behavior of open quantum systems in which qubit dynamics is determined

by phononic loss. By shaping the loss spectrum of the qubit via its coupling to a bath of lossy piezoelectric surface acoustic wave phonons, we demonstrate preparation and dynamical stabilization of a family of superposition states when the qubit is subjected to the combined effects of drive and dissipation. We model this driven open quantum system using the Lindblad master equation, and find excellent agreement for both the qubit dynamics as well as its steady state. These experiments highlight the versatility of engineered phononic dissipation in superconducting circuits. The results advance the understanding of mechanical losses in open quantum systems and extensions of this work could impact the mitigation of phonon-induced decoherence in superconducting processors.

Hybrid quantum systems based on the coherent coupling of two or more distinct, but interacting, systems enable the development of advanced quantum technologies [6], and investigation into the fundamental properties of complex interacting quantum degrees of freedom. Hybrid systems based on superconducting qubits, utilizing the experimental tool-kit of circuit quantum electrodynamics (cQED) [11], are a versatile platform for creating and controlling heterogeneous quantum systems and investigating their coherent dynamics [7]. Of particular interest is the ability to leverage the intrinsically strong nonlinearity provided by the qubit to manipulate collective mechanical and acoustic degrees of freedom and explore new regimes of circuit quantum optics using GHz-frequency phonons. By engineering strong interactions between superconducting qubits and mechanical resonators it is possible to study the quantum limits of high-frequency sound in a wide variety of systems composed of qubits coupled to bulk phonons [3,28], Rayleigh-like surface waves [4,8,14,153,154,169,189], as well as flexural modes in suspended structures [190–192]. Impressive experimental results have been demonstrated using integrated quantum acoustic systems, including single phonon splitting of the qubit spectrum [49, 57, 59], Wigner function negativity of an acoustic resonator [3, 4, 50, 59],

electromagnetically induced acoustic transparency [189], and phonon mediated state transfer [24, 25]. Hybrid quantum acoustics systems that integrate superconducting qubits with

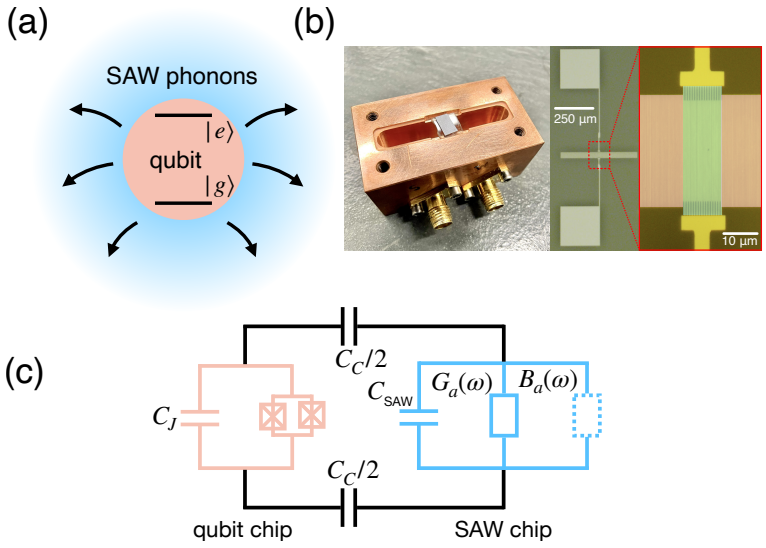

Figure 6.1: (a) Schematic representing a qubit coupled to a bath of SAW phonons. The qubit (salmon) non-unitarily radiates excitations into a bath of SAW phonons (blue), where the emission rate is mediated by the electrical conductance of the SAW structure. (b) Image of the flip-chip qubit-SAW hybrid device mounted in a 3D microwave cavity (left), which is used for control and readout. False color optical micrograph of the acoustic resonator (right), consisting of an IDT (green), as well as acoustic Bragg mirrors (red). (c) Equivalent circuit model of the composite qubit-SAW system. Here C_J is the total capacitance shunting the Josephson junctions, C_C is the capacitance responsible for coupling the qubit and SAW resonator, which is primarily dictated by the parallel-plate capacitance between the two substrates, and C_{SAW} is the geometric capacitance of the SAW resonator. The complex admittance that represents the electro-mechanic response of the SAW resonator is divided into a conductance $G_a(\omega)$, as well as a susceptance $B_a(\omega)$.

phononic degrees of freedom typically operate in a domain where the interaction strength between the two far exceeds the loss rate of either system. In this strong coupling regime, the emphasis is on the coherent dynamics of the coupled systems rather than on the dissipation presented to the qubit via the phononic bath. However, the ability to create open quantum acoustic systems in which the qubit is variably coupled to multiple mechanical degrees of freedom with vastly differing strengths and loss rates opens the door for dissipative state preparation and dynamically stabilized states in the presence of a strong drive

and customized phononic loss channels. Piezoelectric surface acoustic wave (SAW) devices, which can be engineered into compact devices with sharp spectral responses [4, 8, 169], are a promising avenue for engineering highly frequency dependent phononic dissipation channels for quantum bath engineering protocols, in which the level of surface wave dissipation and qubit coupling can be precisely designed and controlled (see Fig. 6.1(a)).

The spectral response of the SAW resonator was calculated using coupling-of-modes (COM) [122]. The periodicity of the SAW interdigitated transducer (IDT) structure is fabricated to be $\lambda_{\mathrm{IDT}} = 800$ nm. The periodicity of the mirror structure is fabricated to be slightly larger than the periodicity of the IDT structure ($\lambda_{\mathrm{mirror}} = 816$ nm) to guarantee a single sharply peaked resonant acoustic mode within the stopband of the mirrors where phonons are strongly reflected, which produces the confined acoustic resonance at 4.46 GHz. A list of the complete SAW device parameters are listed in Table 6.1. The last four rows of Table 6.1 are adjusted to fit the spectroscopy of the hybrid system to the simulated conductance via coupling-of-modes. The first six rows of Table 6.1 define the geometric properties of the SAW device and are defined in fabrication, and we calculate the relevant scattering parameters for each structure in the SAW resonator using coupling-of-modes with the results shown in Fig. 6.2.

The broad frequency response of the conductance in Fig. 6.2(c) arises from the Fourier transform of the spatial structure of the SAW transducer. The width of the response is dictated by the number of finger pairs constituting the transducer, labeled N_p in Table 6.1 (see Fig. 6.1) [159]. The SAW device is galvanically connected to two large antenna pads and coupled to the transmon qubit via a flip-chip technique, forming an effective set of parallel plate capacitors between the antenna pads on the SAW and transmon chips as depicted in Fig. 6.2(e).

Parameter	Physical quantity	Value
λ_{IDT}	Transducer periodicity	800 nm
$\lambda_{\mathrm{mirror}}$	Mirror periodicity	816 nm
N_P	Number of finger pairs	16
W	Finger pair overlap	35 μm
L_{mirror}	Bragg mirror length	240.72 μm
L_{IDT}	Transducer length	12 μm
v_{sound}	Speed of sound	3638 m/s
η	SAW propagation loss	500 Np/m
r_i	Transducer reflectivity	-0.005i
r_m	Mirror reflectivity	-0.005i

Table 6.1: Summary of relevant parameters for the SAW resonator used in the experiment

6.2 SAW + qubit experiments

We implement a quantum acoustic bath engineering protocol using a hybrid quantum system consisting of a flux-tunable transmon qubit coupled to a SAW Fabry Pérot cavity fabricated on the surface of single crystal lithium niobate (see Fig. 6.1 and Fig. 6.2). The complex admittance that describes the electro-mechanical properties of the SAW device, and tailors the coupling to the phonon bath, are calculated using coupling of modes [122, 159]. The qubit and SAW resonator are fabricated on separate substrates and their purely capacitive coupling is mediated in a flip-chip geometry via antenna pads attached to each device in the form of a pair of parallel plate capacitors (see Fig. 6.1)). For control and readout, the composite flip-chip device is free-space coupled to the fundamental mode of a three-dimensional (3D) electromagnetic cavity with a frequency of $\omega_c/(2\pi) = 4.788$ GHz. As shown in Fig. 6.3(a), we design the SAW resonator spectral response in order to access both its coherent coupling to the transmon as well as the dissipative qubit-phonon dynamics. The SAW resonator is engineered to confine a single acoustic mode, which appears as a sharp peak in the conductance of the resonator near 4.46 GHz (see Fig. 6.3(a)). Near this confined acoustic mode, we fit the simulated conductance to a Lorentzian function and extract the

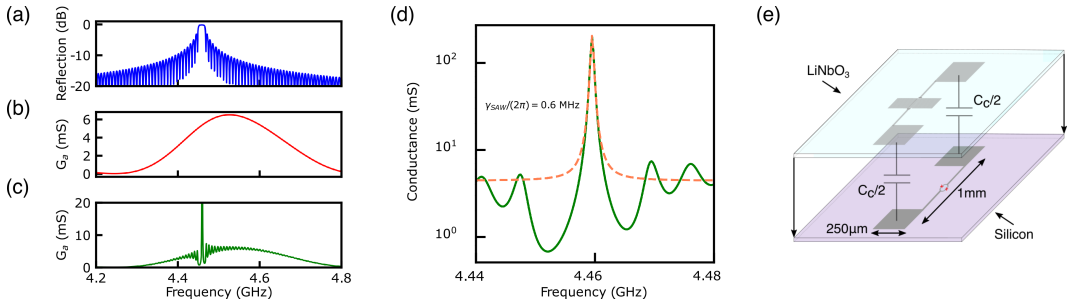

Figure 6.2: (a) Simulated reflection of the Bragg mirror structure in the SAW resonator. (b) Simulated conductance of the SAW transducer, which is centered between the two acoustic Bragg mirrors. (c) Composite conductance of the SAW transducer cascaded with the mirror structure, leading to a single confined SAW mode near 4.46 GHz and a continuous conductance associated with the leakage of SAW energy through the Bragg mirrors. (d) Near the confined mode the SAW resonator conductance can be approximated by a Lorentizian function (dashed orange fit). The full width at half maximum of this Lorentizian is used to estimate the energy decay rate of the confined SAW mode. (e) Schematic of the flip-chip assembly. The antenna pads on either substrate form parallel plate capacitors between the two devices.

SAW energy decay rate $\gamma_{\mathrm{SAW}}/(2\pi) = 0.6$ MHz from the full width at half maximum (see Fig. 6.2). On either side of this main SAW resonance, phononic energy loss is governed by a continuum of dissipative SAW states that manifest as frequency ripples in the effective conductance of the acoustic resonator and correspond to the leakage of surface-phonons out of the SAW resonator through the acoustic Bragg mirrors (see Fig. 6.1(b)). Measurements shown in Fig. 6.3(b) reveal how the features of the SAW resonator response are imparted onto the spectroscopic properties of the hybrid system and enable access to multiple regimes of circuit quantum acoustodynamics (cQAD) [8]. The qubit and the confined SAW mode interact with a coupling rate $g_m/(2\pi) = 12 \pm 0.6$ MHz, larger than the loss rate of either system ($\gamma_{\mathrm{SAW}}/(2\pi) = 0.6$ MHz and $\gamma_q/(2\pi) = 2.67$ MHz), which is a hallmark of the quantum acoustic strong coupling regime. Strong coupling between a resonant SAW mode and a transmon qubit has been observed in previous experiments [4, 57, 154] and this regime serves to demonstrate hybridization between the qubit and SAW modes. More importantly,

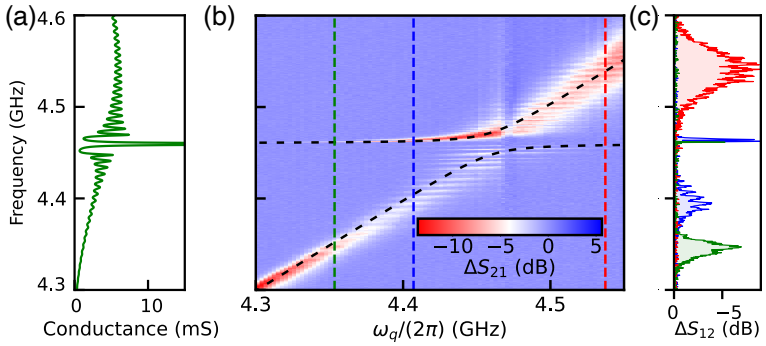

Figure 6.3: (a) Simulation of the SAW resonator conductance $G_{\mathrm{a}}(\omega)$ based on the coupling-of-modes modeling. The resonator is designed to host a single confined SAW mode, which corresponds to the narrow peak in the device conductance at 4.46 GHz, and the effective electrical conductance of the device mediates the coupling between the qubit and a given SAW mode. (b) Two-tone spectroscopy of the SAW-qubit hybrid system revealing an avoided crossing between the qubit and main SAW mode. Black dashed line: fit to the data, indicating an acoustic coupling of $g_m/(2\pi) = 12 \pm 0.6$ MHz. (c) Spectroscopy line-cuts from (b) at the positions of the vertical dashed lines. The oscillations in frequency in each scan highlight the phononic loss channel imparted on the qubit, which arise from the modulation of the conductance of the SAW resonator and are associated with the leakage of SAW excitations through the acoustic Bragg mirrors.

the spectroscopy shown in Fig. 6.3(b,c) also reveals signatures of controlled surface phonon loss arising from the interaction of the qubit with the continuum of SAW modes on either side of the confined SAW mode. This interaction manifests as a series of dark states in the qubit spectrum, which appear as horizontal fringes in Fig. 6.3(b), and corresponds to the acoustic analog of the bad-cavity limit of cQED [11]. In this dissipative regime the dynamics of the hybrid system is dominated by the loss of phonons from the resonator that have a frequency outside of the acoustic mirror stop band.

To utilize the frequency-dependent acoustic loss for dynamical quantum state stabilization, we consider the effect of phononic decay on qubit decoherence in the presence of a strong coherent drive of amplitude Ω near resonant with the qubit. In this regime, the emission spectrum the system consists of a peak at the drive frequency ω_d and two additional sidebands at $\omega_d \pm \Omega_R$, where $\Omega_R = \sqrt{\Omega^2 + \Delta^2}$ is the generalized Rabi frequency and

$\Delta = \omega_d - \omega_q$ is the detuning between the drive and the qubit [193–195] (see Fig. 6.4(a)). In the presence of a frequency-dependent emission spectrum, one sideband can be suppressed, leading to preferential emission from the other sideband and non-zero qubit coherence in the undriven basis for times long compared to the intrinsic lifetime of the qubit [89]. For this type of bath engineering protocol to work in our device, the SAW admittance must modify the decoherence rate of the qubit over frequencies comparable to experimentally accessible values of Ω_R. To verify this, we measured the qubit decay rate $\Gamma_q = 1/T_1$ across a broad range of frequencies far-detuned from the main acoustic resonance (see Fig. 6.4(b)) where phonon leakage through the acoustic mirrors is maximized. At these frequencies, the conductance of the SAW resonator is well approximated by that of the acoustic transducer, as the reflectivity of the acoustic Bragg mirrors is small, and the total loss of the qubit can be approximated as:

$$\Gamma_q\left(\omega_q\right) = \frac{\omega_q}{2\pi Q_i} + \Gamma_0 \ \mathrm{sinc}^2\left(\pi N_p \frac{\omega_q - \omega_s}{\omega_s}\right), \tag{6.1}$$

where $Q_i = \ 1.67 \times 10^3$ is the qubit internal quality factor, $\Gamma_0 = 0.252$ ns^{-1} is the maximum conversion rate of the qubit excitation into SAW phonons, $N_p = 16$ is the number of finger pairs in the IDT structure of the SAW resonator, and $\omega_s/(2\pi) = 4.504$ GHz is the central SAW frequency, which is within 1% of the value predicted from the device fabrication parameters(reference the table here). The first term in Eq. 7.1 describes the decay of the bare qubit while the second term is associated with qubit energy conversion into SAW phonons. At $\omega_q/(2\pi) = 4.001$ GHz, where the gradient of qubit loss into SAW phonons is large, the qubit decay rate varies by a factor of 3.7 over a span of 80 MHz ($\approx 2\Omega_R$) and allows us to use SAW phonon modes for efficient state preparation.

The dynamics of the reduced qubit density matrix in the combined presence of the drive

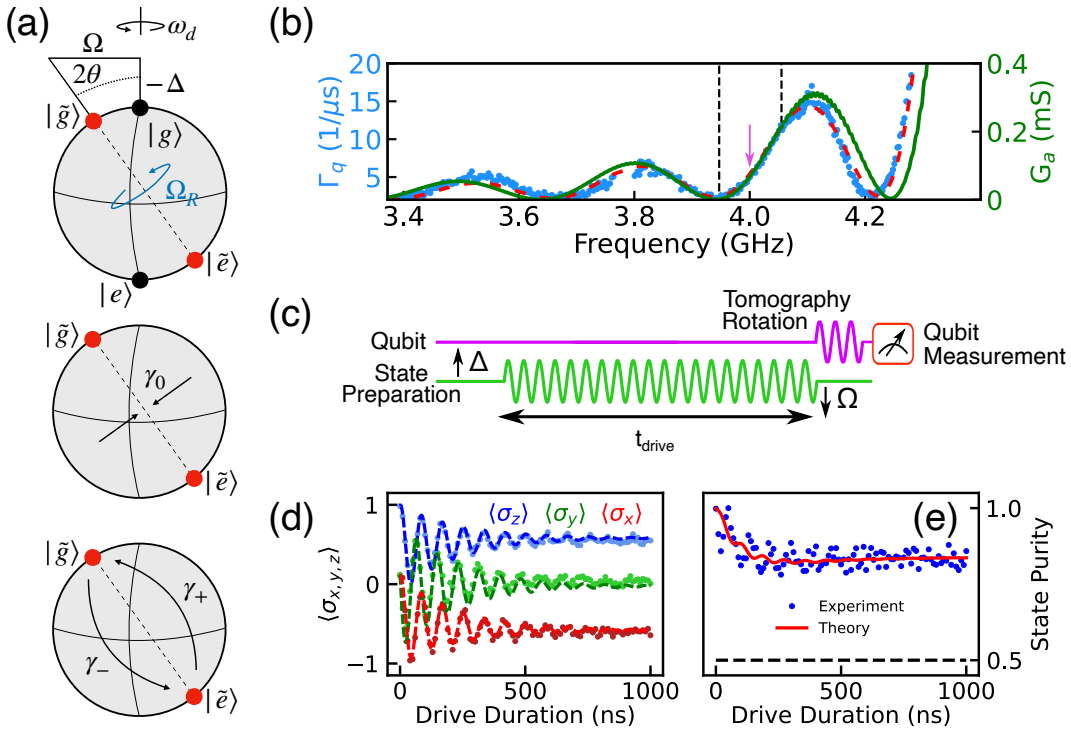

Figure 6.4: (a) Top: schematic representing the rotation of the qubit eigenbasis in the presence of a detuned drive applied to the qubit. Center: representation of pure dephasing in the dressed basis. Bottom: representation of competing decay rates in the dressed qubit basis. By tailoring the coupling of the qubit to the frequency-dependent phonon bath, we are able to control the relative size of $\gamma_\pm$ as a function of qubit frequency. (b) Measurement of qubit loss $\Gamma_q = 1/T_1$ versus frequency (blue). The red curve is a fit to Eq. 7.1 showing that the variation in the qubit loss is dictated by conversion into SAW phonons. The green curve is a result of coupling-of-modes model for the electrical conductance of the SAW resonator with no fit parameters. The arrow indicates the frequency at which the bath engineering experiments are performed. The black dashed lines are the endpoints of experimentally accessible Mollow triplet sidebands. (c) Pulse sequence for investigating the coherence of the driven-dissipative quantum acoustics system. (d) Tomographic reconstruction of qubit state evolution at a resonant Rabi frequency of $\Omega/(2\pi) = 8.47$ MHz and drive detuning $\Delta/(2\pi) = -10$ MHz. Dots represent the experimental data while the dashed lines are solutions to Eq. 6.2 with the same drive parameters, which correspond to $\gamma_+ = 3.4\ \mu s^{-1}$ and $\gamma_- = 1.3\ \mu s^{-1}$. (e) Measurement of the state purity as a function of time. In the combined presence of phonon loss and drive the purity reaches a value of 0.85 at $t = 1\ \mu$s, in contrast to a maximally mixed state represented by the dashed line at $\mathcal{P} = 0.5$. The solid red line is the expected state purity based on Eq. 6.2.

and frequency-dependent SAW loss are described by the Lindblad master equation [72,87,89]:

$$\dot{\rho} = i[\rho, \mathcal{H}] + \gamma_0 \cos^2(\theta) \sin^2(\theta) \mathcal{D}[\tilde{\sigma}_z]\rho + \gamma_- \sin^4(\theta) \mathcal{D}[\tilde{\sigma}_+]\rho$$
$$+ \gamma_+ \cos^4(\theta) \mathcal{D}[\tilde{\sigma}_-]\rho + \gamma_1 \mathcal{D}[\sigma_-]\rho + \frac{\gamma_\phi}{2} \mathcal{D}[\sigma_z]\rho, \tag{6.2}$$

where $\mathcal{D}[A]\rho = \left(2A\rho A^\dagger - A^\dagger A\rho - \rho A^\dagger A\right)/2$. The angle θ is defined by $\tan 2\theta = -\Omega/\Delta$ and represents the rotation of the qubit eigenbasis under the drive (see Fig. 6.4(a)). The operators $\tilde{\sigma}_\pm$ and $\tilde{\sigma}_z$ along with the corresponding rates $\gamma_\pm$ and γ_0 represent transitions between eigenstates and dephasing in the rotated frame. Dissipation in the lab frame is represented by the operators σ_- and σ_z along with the rates γ_1 and γ_ϕ, for qubit depolarization and dephasing. The transition rates $\gamma_\pm$ represent competing decay of the qubit into SAW phonons in the rotated basis, and by tailoring the frequency-dependent phonon bath these rates vary significantly over the frequency scale $2\Omega_R$ as seen in Fig. 6.4(b). In the limit $\gamma_\pm \gg \gamma_\mp$, the spectral weight of one sideband of the qubit emission spectrum is suppressed, leading to dynamical stabilization of a rotating-frame eigenstate. In general, the plane accessible within the Bloch sphere is controlled by the phase of the drive signal. In the measurements described below, we set the phase of the drive such that the qubit eigenstates lie in the XZ - plane of the Bloch sphere. The chosen Rabi frequency and drive detuning further constrain the qubit eigenstates to a particular axis in this plane.

6.3 Numerical calculation of Lindblad dynamics

Given a periodic drive coupling to the σ_x operator with Rabi frequency Ω, the Hamiltonian that describes the qubit in the frame rotating at ω_d is given by

$$\mathcal{H} = \frac{\Delta}{2}\sigma_z + \frac{\Omega}{2}\sigma_x, \tag{6.3}$$

where $\Delta = \omega_d - \omega_q$ is the qubit-drive detuning. In the presence of the drive, the corresponding qubit eigenstates ($|g\rangle$,$|e\rangle$) are rotated to a dressed basis ($|\tilde{g}\rangle$,$|\tilde{e}\rangle$), corresponding to the

eigenvectors of Eq.6.3:

$$|\tilde{g}\rangle = \cos\theta\,|g\rangle - \sin\theta\,|e\rangle \tag{6.4}$$

$$|\tilde{e}\rangle = \sin\theta\,|g\rangle + \cos\theta\,|e\rangle\,,$$

where the rotation angle of the eigenstates is defined by $\tan 2\theta = -\Omega/\Delta$. This allows the Hamiltonian to be rewritten in the dressed basis as

$$\mathcal{H} = \frac{\Omega_R}{2}\tilde{\sigma}_z, \tag{6.5}$$

where $\Omega_R = \sqrt{\Omega^2 + \Delta^2}$ is the generalized Rabi frequency and $\tilde{\sigma}_z = \sin 2\theta\sigma_x - \cos 2\theta\sigma_z$. The evolution of the reduced density matrix in the dressed basis as given by the Lindblad master equation (Eqn. 6.2). We represent the density matrix as a vector $\rho = (\rho_{gg}, \rho_{ge}, \rho_{eg}, \rho_{ee})^T$, which is evolved in time as $\rho(t) = e^{\mathcal{L}t}\rho(0)$. The matrix $\mathcal{L}$ represents the Lindblad operator as a 4×4 matrix that is exponentiated via the transformation $Ve^{Dt}V^{-1}$, where V is the matrix that diagonalizes $\mathcal{L}$ and D is a diagonal matrix containing the eigenvalues of $\mathcal{L}$. We calculate expectation values by taking the trace $\langle\sigma_x\rangle = \mathrm{Tr}(\sigma_x\rho)$ and similarly for the other components of the qubit expectation value. Custom Python code for this process can be found at Ref. [196].

6.4 Phononic open quantum system results and discussion

We calibrate the magnitude of the resonant Rabi frequency by measuring the excited state population of the qubit as a function of time over a range of drive amplitudes as shown in Fig. 6.5(a). The frequency of the resulting oscillatory behavior varies linearly with drive amplitude as shown in Fig. 6.5(b) and provides a mapping between Rabi frequency and drive. To demonstrate the phononic bath engineering protocol, we flux bias the qubit to

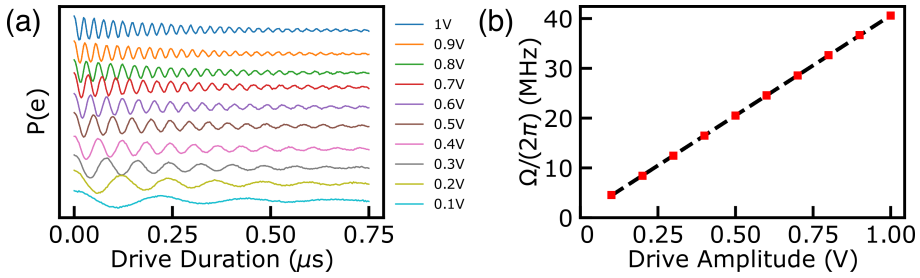

Figure 6.5: (a) Resonant Rabi oscillations for various drive amplitudes ranging from 0.1V to 1V. As the amplitude is increased, the frequency of oscillation increases. Traces have been vertically offset for clarity. (b) Extracted Rabi frequencies from the data in panel (a). The frequency increases linearly with drive amplitude as expected and allows us to interpolate the resonant Rabi frequency for a given drive amplitude.

$\omega_q/(2\pi) = 4.001$ GHz, where the gradient of the qubit loss varies strongly as a function of frequency (see Fig. 6.4(b)). By tailoring the drive parameters the qubit emits radiation at frequencies corresponding to Mollow triplet sidebands [193] at rates governed by the SAW-phonon induced loss. To calibrate the drive strength, we measure resonant Rabi oscillations as a function of drive amplitude and interpolate the results to obtain a mapping between drive amplitude to Rabi frequency (see Fig. 6.5). By driving the qubit at a detuning $\Delta/(2\pi) = -10$ MHz with strength $\Omega/(2\pi) = 8.47$ MHz we demonstrate the ability to prepare a qubit state in the XZ-plane of the Bloch sphere, which we verify using tomographic reconstruction of the

qubit state as a function of driving time t_{drive} (see Fig. 6.4(c,d)). As shown in Fig. 6.4(d), in the limit $t_{\text{drive}} \gg T_1$, the qubit density matrix approaches a fixed point determined by the drive parameters and asymmetric phononic loss. We further quantify this dissipation-enabled dynamical stabilization protocol by calculating the state purity of the qubit, $\mathcal{P} = \text{Tr}(\rho^2)$, as a function of time as shown in Fig. 6.4(e). We see that, in the limit $t_{\text{drive}} \gg T_1$, the state purity reaches $\mathcal{P} = 0.85$, well above the value $\mathcal{P} = 0.5$ of a maximally mixed state. By including fit parameters that describe the global dephasing rate $\gamma_\phi = 1.48\ \mu\text{s}^{-1}$ and global depolarization rate of $\gamma_1 = 2.46\ \mu\text{s}^{-1}$ in the numerical solutions to Eq. 6.2, we find quantitative agreement with the tomography data shown in Fig. 6.4(d,e).We note that these optimal fit parameters are in reasonable agreement with the measured values for the bare qubit decay at this frequency $\gamma_q/(2\pi) = f_q/Q_i \simeq 2.4\ \mu\text{s}^{-1}$ and the pure dephasing rate $\gamma_{\phi,\text{exp}} \simeq 0.93\ \mu\text{s}^{-1}$.

In the basis dressed by the drive, this dynamically stabilized qubit state is effectively cooled toward thermal equilibrium via the frequency-dependent emission of energy into SAW phonons. Because the qubit reduced density matrix is no longer evolving in time for sufficiently long values of t_{drive}, the driven-dissipative system has reached its steady state and the notion of an effective qubit temperature is well-defined. To quantify the efficiency of this phonon-induced qubit cooling, we consider the driven qubit as a two level system subject to the Hamiltonian $\mathcal{H} = \frac{\hbar\Omega_R}{2}\tilde{\sigma}_z$, in equilibrium with an effective thermal bath, where $\tilde{\sigma}_z = \sin(2\theta)\sigma_x - \cos(2\theta)\sigma_z$. The partition function for this system is $\mathcal{Z} = 2\cosh\left(\frac{\hbar\Omega_R\beta_{\text{eff}}}{2}\right)$, with $\beta_{\text{eff}} = 1/k_b T_{\text{eff}}$, where k_b is the Boltzmann constant and T_{eff} is the effective qubit temperature. Over many repeated measurements the average qubit energy is given by $\langle\epsilon\rangle = \frac{\hbar\Omega_R}{2}\langle\tilde{\sigma}_z\rangle$, which can used along with the partition function to relate the measured value of $\langle\tilde{\sigma}_z\rangle$ to the effective temperature $T_{\text{eff}} = -\hbar\Omega_R/(2k_b \tanh^{-1}\langle\tilde{\sigma}_z\rangle)$.

With the qubit in thermal equilibrium with the surface phonon bath, we find an effective temperature of $T_{\text{eff}} \approx 250$ μK based on the experimental data in Fig. 6.4(d), which is also the lowest effective temperature we were able to obtain in our experiments. This low effective temperature arises from the fact that the driven-dissipative protocol creates and cools an effective quantum two-level system having an energy splitting $\Omega_R/(2\pi) \approx 13$ MHz, which is significantly lower than the frequency of the qubit in the lab frame. This combination of effective temperature and transition frequency $\Omega_R/(2\pi)$ correspond to an excited state population of approximately 10%, equivalent to a transmon qubit with a transition frequency of 4 GHz at a temperature of 90 mK. Finally we note, that the efficiency of the driven-dissipative cooling in the current experiment is primarily limited by the relatively large rates γ_1 and γ_ϕ of the qubit. In particular, solutions to Eq. 6.2 predict an effective temperature as low as 85 μK if the global energy decay rate and dephasing of the qubit were improved by approximately an order of magnitude to $\gamma_1 = \gamma_\phi = 0.1$ μs^{-1}. In the combined presence of drive and phonon loss through the mirrors, the steady-state of the qubit should exhibit coherence on timescales long in comparison to the intrinsic qubit lifetime in the lab frame. To investigate this steady-state behavior, we apply a coherent drive to the qubit for a time $t_{\text{drive}} = 3$ μs, which is approximately one order of magnitude longer than the measured depolarization time of the qubit in the absence of drive. By choosing the parameters of the drive, we control both the rotation of the qubit eigenstates as well as the splitting of the Mollow triplet sidebands, which modifies their coupling to the lossy phononic bath. We begin by tomographically reconstructing the steady-state expectation value $\langle\sigma_x\rangle = \text{Tr}(\rho\sigma_x)$ in the bare qubit eigenbasis as a function of drive parameters and compare with the solutions to Eq. 6.2 as shown in Fig. 6.6. As we modify parameters of the drive, we observe excellent agreement between the measured and predicted value of $\langle\sigma_x\rangle$ of the resulting qubit state,

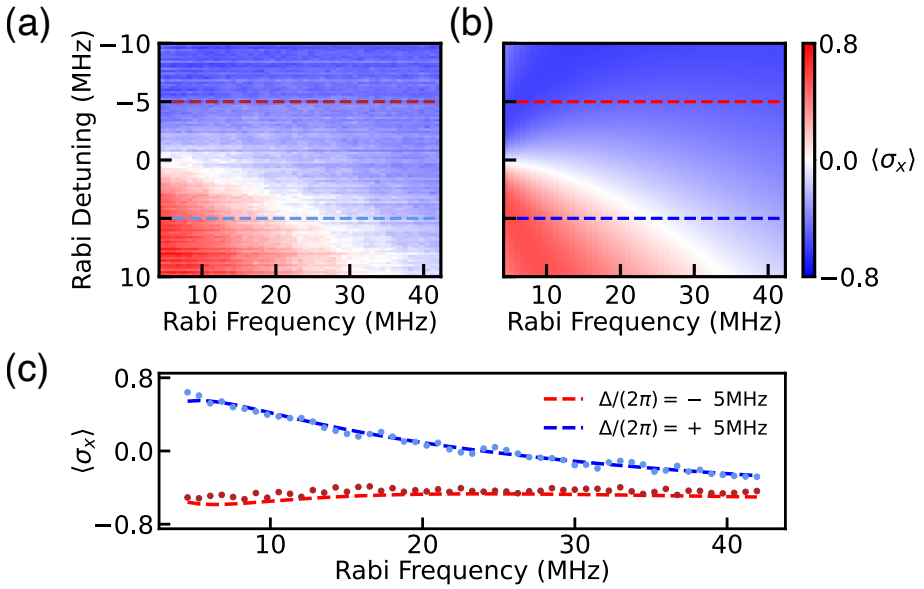

Figure 6.6: (a) By varying both the strength (resonant Rabi frequency) and the detuning of the state preparation pulse relative to the qubit frequency we are able to demonstrate dynamical state stabilization that has both positive and negative values of $\langle\sigma_x\rangle$. (b) Numerical solutions to Eq. 6.2 over the same range of drive parameters as in panel (a). The rates γ_1 and γ_ϕ are fit parameters as described in the text, while all other model parameters are determined empirically. (c) Representative horizontal linecuts from panel (a) along with the corresponding predictions based on the solution to the Lindblad master equation (panel (b)).

and reveal a region of zero coherence where the competing loss rates $\gamma_\pm$ in Eq. 6.2 cancel each other and $\langle\sigma_x\rangle = 0$.

For completeness we also present the measured values of $\langle\sigma_z\rangle$ and $\langle\sigma_y\rangle$ in Fig. 6.8(a,c) along with comparison to Eq. 6.2 in Fig. 6.8(b,d). The qubit reduced density matrix is given by $\rho = \frac{1}{2}\left(\mathbb{1} + \sigma_x\langle\sigma_x\rangle + \sigma_y\langle\sigma_y\rangle + \sigma_z\langle\sigma_z\rangle\right)$, where $\mathbb{1}$ is the 2×2 identity matrix. Each tomography component is calibrated relative to the readout contrast along each axis of the Bloch sphere and scaled such that the length of the qubit state vector does not exceed unity. The purity of a given state is then calculated to be $\mathcal{P} = \mathrm{Tr}(\rho^2)$ and is shown in Fig. 5(a,c) of the main text and is compared with the results of Eq.6.2 in Fig. 5(b,c). The systematic difference between the measured tomography components and those obtained from solutions to Eq. 6.2 (most evident as small non-zero measured values of $\langle\sigma_y\rangle$ in Fig. 6.8(c)) likely

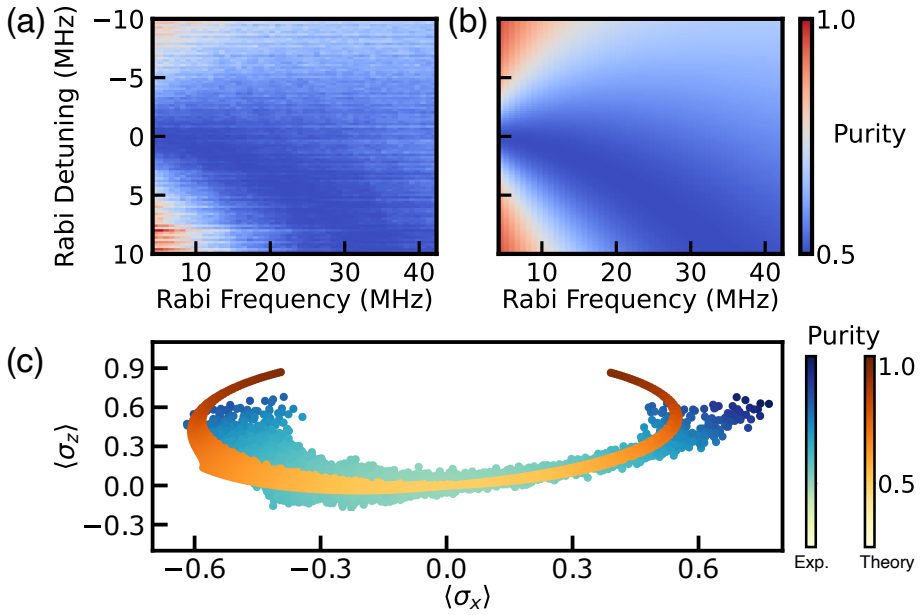

Figure 6.7: (a) Measured steady-state purity with the same drive parameters as in Fig. 4. (b) Purity based on solutions to Eq. 6.2 under same drive parameters. (c) Purity of the qubit steady-state in the XZ-plane of the Bloch sphere across the same range of drive parameters, where solutions to Eq. 6.2 are overlaid on the experimental data.

arises from systematic errors produced by time-dependent variation of the qubit transition frequency over the relatively long duration (several hours) of the tomography measurements as a function of drive parameters. A tomography measurement consists of a $\pi/2$ rotation with a well-defined phase to project either the x or y-component of the qubit state vector onto the measurement (z) axis of the Bloch sphere, and subsequent projective measurement. To obtain the z-component of the state vector, no tomography rotation is required prior to measurement. In the presence of a detuned drive, as is the case for our measurements at $\Delta \neq 0$ in Figs. 3-5 in the main text and Fig. 4, the qubit state acquires an additional phase shift of $\phi = 2\pi \times \Delta \times t_{\text{drive}}$, during the detuned drive. To account for this additional phase accumulation, the phase of each tomography pulse is shifted by the same amount ϕ prior to projective measurement. Because the phase of the tomography pulses depend on the detuning in this fashion, fluctuations in Δ introduce systematic errors in the measured

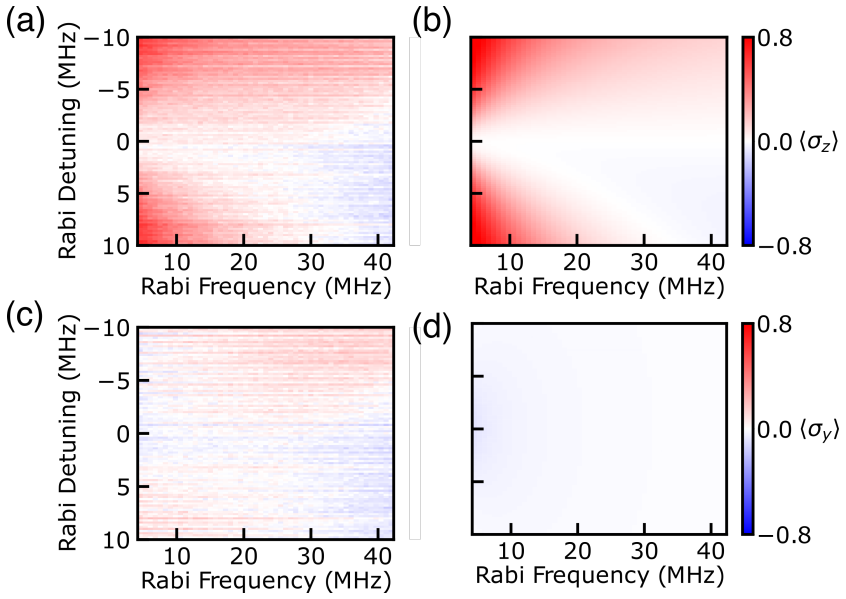

Figure 6.8: (a) Measured values of $\langle\sigma_z\rangle$ with the same drive parameters as in Fig. 4 of the main text. (b) $\langle\sigma_z\rangle$ obtained from solutions to Eq. 6.2 with the same drive parameters as Fig. 4 of the main text. (c) Measured values of $\langle\sigma_y\rangle$ with the same drive parameters. (d) $\langle\sigma_y\rangle$ obtained from solutions to Eq. 6.2 with the same drive parameters.

tomography components. Qubit frequency variations can be clearly seen in measurements of Ramsey interferometry taken over many hours, as shown in Fig. 6.9. We observe slow drift in the qubit frequency, indicating the presence of low-frequency noise in the system as well as discrete "jumps" in the qubit frequency. These type of discrete jumps are often seen in superconducting qubit experiments and in our case likely arise from unwanted coupling to dielectric two-level fluctuators [197]. Furthermore, full tomographic measurement of the qubit state vector allows us to reconstruct the qubit reduced density matrix and calculate the steady-state purity of the qubit as function of drive parameters as shown in Fig. 6.7(a), which we also find to be in good agreement with solutions to Eq. 6.2 (see Fig. 6.7(b)). As shown in Fig. 6.7(c) we further investigate the versatility of this state preparation protocol by plotting the purity as a function of the coordinates of the qubit state vector in the XZ-plane over the experimentally accessible values of the drive parameters. We find that the

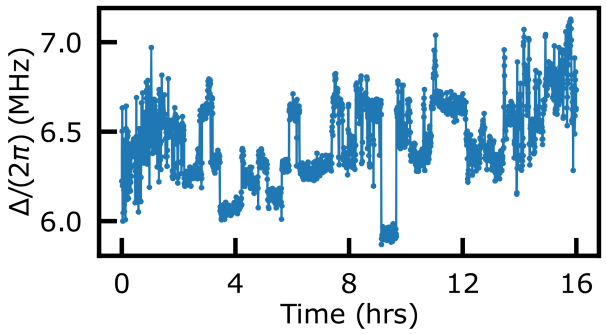

Figure 6.9: Detuning ($\Delta = \omega_d - \omega_q$) between the time-varying qubit frequency and a fixed drive frequency ($\omega_d/(2\pi) = 4.007$ GHz) measured via Ramsey interferometry over 16 hours. Both slowly varying frequency drift and discrete frequency jumps on the order of 1 MHz are observed in $\omega_q/(2\pi)$. The discrete frequency jumps are likely due to non-resonant coupling to two-level fluctuators in the qubit chip.

dissipation-enabled state preparation can be used to create high purity superposition states across a relatively large range of $\langle\sigma_x\rangle$. However, access to large negative values of $\langle\sigma_z\rangle$ is limited in this device by the difference between γ_+ and γ_- arising from the slope of the SAW device conductance versus frequency. We find that these experimental results are also in good agreement with the open quantum systems modeling based on solutions to Eq. 6.2, which is also displayed in Fig. 6.7(c). We note that the systematic difference in the span between the experimentally and numerically obtained values of tomography components in the XZ-plane likely arises from long timescale variation in the qubit frequency during the relatively long duration (several hour) tomography measurements (see Fig. 6.9).

Finally, we investigate the thermodynamic properties of the driven dissipative qubit. Importantly, because the qubit cooling procedure depends on the rotation of the qubit eigenstates relative to the undressed basis, we might similarly expect the steady-state effective temperature T_{eff} to depend on the drive parameters. As shown in Fig. 6.10, the dependence of the steady-state effective temperature largely follows that of $\langle\sigma_x\rangle$. Interestingly, we note that we are able to achieve *negative* effective temperatures, which correspond to population

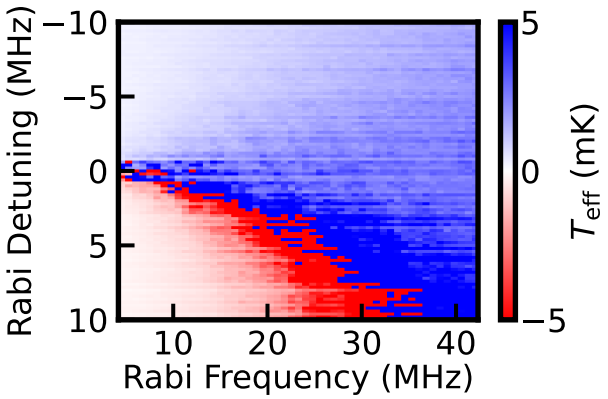

Figure 6.10: Steady-state temperature of the driven-dissipative qubit as a function of drive strength Ω and drive detuning Δ.

inversion, i.e. when the steady-state of the qubit has an appreciable population in the state $|\tilde{e}\rangle$. Furthermore, we can re-cast the data presented in Fig. 6.10 as a histogram. As seen in Fig. 6.11 we measure a distribution of temperatures with an average effective temperature $\overline{T}_{\text{eff}} = 1.24$ mK. We approximate the width of the distribution as the full-width at half-maximum $\Delta T_{\text{eff}} = 2.85$ mK.

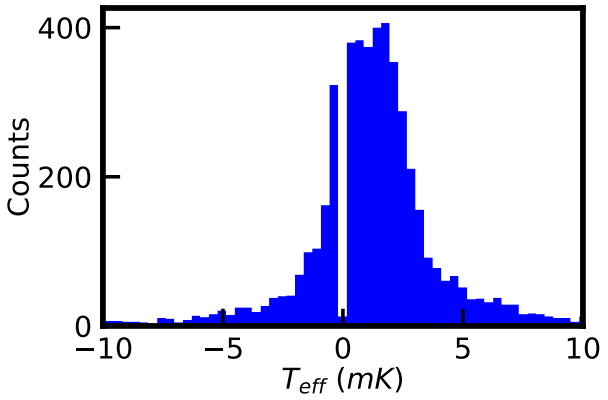

Figure 6.11: Distribution of effective temperatures T_{eff}. We measure a significant portion of negative effective temperatures, corresponding to population inversion.

6.5 Conclusion

In this chapter we have described a phononic open quantum system composed of a superconducting qubit coupled to an engineered bath of lossy surface acoustic wave phonons. This system enables the investigation of the dynamical and steady-state of superpositions of the qubit when it is subjected to the combined effects of strong driving and phononic loss. The lossy SAW environment allows for high-purity qubit state preparation and dynamical stabilization within a plane in the Bloch sphere. Modest improvements to the transducer design and qubit quality factor offer an avenue to prepare states with purity exceeding 99%. In particular, this could be achieved by improving the bare qubit lifetime and pure dephasing rate by an order of magnitude, which would enhance the decay of qubit energy into phonons rather than the electromagnetic environment. Similarly, modifying the SAW transducer design to have a sharper spectral response would increase the relative difference of the rates $\gamma_{\pm}$, improving the efficiency of the phononic bath engineering protocol. Finally we note that these results also open the door to investigating the non-unitary evolution of quantum states and effective non-Hermitian Hamiltonians hosting decoherence-induced exceptional points in open quantum acoustic systems via post-selection protocols [91].

Chapter 7

Interference and Scattering in Multi-Mode Quantum Acoustic Systems

7.1 Introduction

Quantum acoustic systems offer a unique opportunity to investigate phononic *interference* and *scattering* processes in the quantum regime. In particular the interaction between a superconducting qubit and a phononic oscillator allows the qubit to sense the oscillator's excitation spectrum and underlying interference effects. In this Chapter we present measurements revealing Fano interference of a resonantly trapped piezoelectric surface acoustic wave (SAW) mode with a broad continuum of surface phonons in a system consisting of a SAW resonator coupled to a superconducting qubit. The experiments highlight the existence of additional weakly coupled mechanical modes and their influence on the qubit-phonon interaction and underscore the importance of phononic interference in quantum acoustic architectures that have been proposed for quantum information processing applications. Additionally, we find that the composite device geometry supports bulk acoustic excitations and identify the mode structure and polarization of these spurious vibrational modes.

Wave interference is a universal phenomenon manifesting in a wide variety of both classical and quantum systems ranging from ocean waves to quantum circuits. The spectral response of these systems encodes the existence of the underlying interference processes, resonant modes, and their losses. A hallmark example is the Fano resonance [60, 61, 198], which arises from the interference between a resonantly scattered mode and a continuum of background states, and leads to a characteristically asymmetric spectral lineshape. Fano interference has been realized in various fundamentally different quantum systems in which sharp resonant modes interact with continuum excitations, including atomic and molecular systems [199, 200], scattering in optical experiments [201, 202], and transport measurements in quantum dot-based condensed matter systems [203, 204]. Regardless of the physical platform, this type of interference manifests as a significant change in the spectral response of the system, and is therefore an important process to understand when interpreting spectroscopic or temporal measurements or assessing device performance. Here we demonstrate, for the first time, the manifestation of Fano-interference in a quantum acoustics system. This interference arises from the interaction between resonantly trapped surface acoustic wave (SAW) phonons with a background of continuous phonon modes in an acoustic Fabry-Pérot resonator that is cooled to near its quantum mechanical ground state. We infer the SAW phonon interference by measuring the absorption spectrum of a superconducting transmon qubit capacitively coupled to the SAW device.

7.2 Experimental setup

Figure 7.1a depicts a schematic of our experiment, which consists of a flux-tunable superconducting transmon qubit that is capacitively coupled with a SAW device hosting a resonant

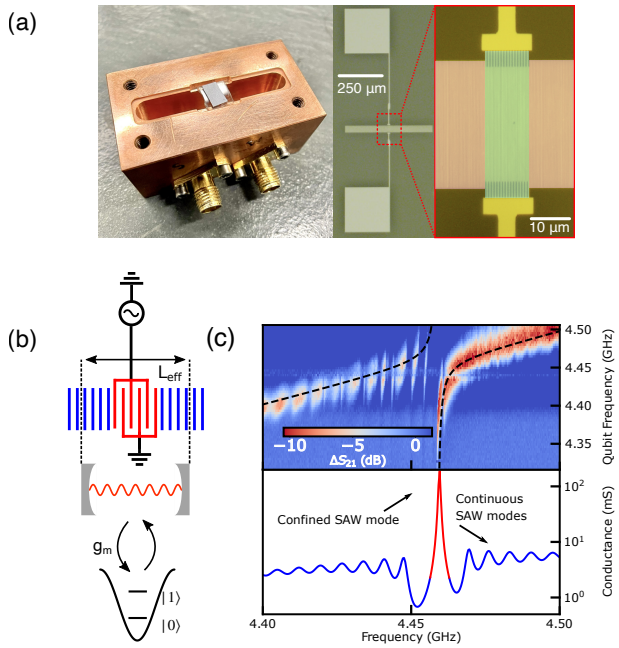

Figure 7.1: (a) Left: Image of the hybrid system housed in the 3D microwave cavity used for control and readout. Center: Optical micrograph of the SAW resonator. The large antenna mediate the coupling between the qubit and SAW resonator. Right: The acoustic transducer (green) is electrically connected to the antenna pads and phonons are confined within the acoustic cavity by the Bragg mirrors (red). (b) Schematic of the experiment. Phononic Bragg mirrors form a spatially distributed Fabry-Pérot cavity that allows for a coherent exchange of energy between the qubit and a resonantly confined SAW mode. (c) Top panel: Measurement of two-tone qubit spectroscopy as the qubit is tuned through the main acoustic resonance and nearby SAW continuum. Strong coupling is seen between the confined acoustic mode while weaker coupling is seen between the qubit and the background of acoustic states. Bottom panel: Simulated mode structure for the SAW device, in which the confined acoustic mode is housed within a continuum of SAW states.

mode at $\omega_m/(2\pi) = 4.4588$ GHz. The spectral response of the SAW device was precisely designed using the coupling-of-modes theory to define the electro-mechanical scattering properties of the device [122, 159], as shown in Fig. 7.1b. The effective electrical conductance of the SAW device was designed such that the resonantly confined acoustic mode is in close spectral proximity to a continuum of acoustic states (see Fig. 7.1b and Section 7.3). The qubit and SAW device are fabricated on separate substrates, with the SAW device on YZ-cut $LiNbO_3$ and the qubit on high-resistivity silicon with maximum Josephson tunneling energy $E_{J,\max}/h = 19.7$ GHz and capacitive charging energy $E_C/h = 328$ MHz. Both devices are

galvanically connected to large antenna pads having an area 250 μm $\times$ 250 μm that form a pair of parallel plate capacitors between the two devices when they are assembled in a flip-chip configuration. The capacitive coupling in this hybrid system ensures that strain in the piezoelectric SAW substrate induces a voltage across the qubit antennae, allowing for the exchange of energy between the qubit and SAW phonons (see Fig. 7.1a). The composite qubit-SAW system is housed in a 3D electromagnetic cavity with fundamental frequency $\omega_c/(2\pi) = 4.788$ GHz, which is used for qubit control and readout as well as for applying independent excitation tones to populate the SAW device, and the interaction strength between the qubit and microwave cavity is measured to be $g/(2\pi) = 75$ MHz. A superconducting coil wound around the cavity provides magnetic flux tunability of the resonant frequency of the qubit. The qubit absorption spectrum is measured via two-tone spectroscopy, using the dispersive interaction between the qubit and cavity to determine the qubit state. As the resonant frequency of the qubit is tuned through the confined acoustic mode, we observe an avoided crossing of magnitude $g_m/(2\pi) = 9.76 \pm 0.60$ MHz (see Fig. 7.1b). Additional interactions between the qubit and phonon modes are also observed. In particular these features correspond to interactions between the qubit and phonons that are not strongly confined to the SAW resonator and therefore couple much more weakly to the qubit, manifesting as a series of dark states in the qubit spectra.

7.3 SAW resonator design

Although the SAW device used for this set of experiments is the same device as the previous chapter, we now focus on the response of the phonon resonator in close proximity to the confined acoustic mode rather than the phonon modes outside of the mirror stop-band. In

this section, we take a closer look at the properties of these resonant phonons and identify how they can satisfy the physical constraints necessary to produce a Fano resonance. A complete list of the SAW device parameters is presented in Table 6.1. Since the reflectivity of the mirrors is relatively low per mirror grating, on average acoustic waves penetrate a distance $L_P \simeq \lambda_{\text{mirror}}/2|r_m|$ into the mirrors before being reflected. Based on the parameters in Table 6.1, we calculate $L_P = 81.6$ μm and the total effective length of the phonon cavity is $L_{\text{eff}} = L_{\text{IDT}} + 2L_P = 175.2$ μm. The free spectral range of the SAW resonator can then be estimated as $\Delta f_{\text{FSR}} = v_s/2L_{\text{eff}} = 10.4$ MHz. The width of the mirror stop band is given by $\Delta f_{\text{mirror}} = \frac{2|r_m|f}{\pi} = 14.2$ MHz [122, 159]. Since the width of the mirror stop band is comparable to the mode spacing, we expect the resonator to host a single strongly confined acoustic mode as well as other more weakly reflected SAW modes as seen in Fig. 7.2 and 7.5.

In Fig. 7.2 we plot the simulated conductance of the composite resonator along with the conductance of the IDT structure. On the frequency scale of the confined mode ($\sim$ 1 MHz) the IDT response is approximately constant creating a continuum of background SAW phonons.

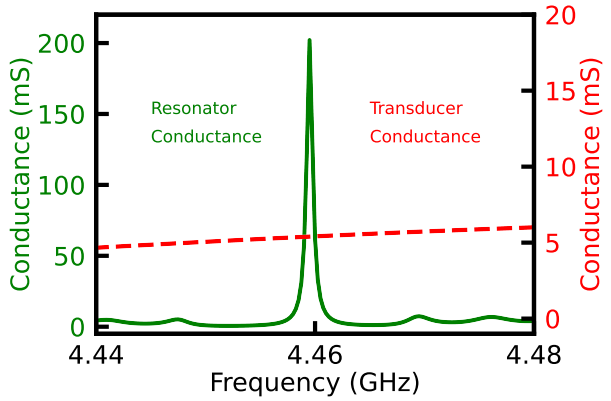

Figure 7.2: Solid green curve: Simulated conductance of the phononic resonator consisting of a central acoustic transducer enclosed in Bragg mirrors. Dashed red curve: simulated conductance of the acoustic transducer alone. The linewidth of the central resonance is much smaller than the width of the transducer response, which can be approximated as a continuous background.

7.4 Results and discussion

To utilize the qubit to measure surface phonon excitations, we first calibrate the qubit response to SAW excitations in the acoustic dispersive limit using the primary confined SAW resonance. In this regime the qubit frequency and spectral shape depend in an established and systematic fashion on the excitation number of SAW bosons. This ac Stark shift has been observed in superconducting qubit systems coupled to both microwave resonators in the cQED framework [40,56] as well as mechanical oscillators of multiple cQAD architectures [8, 49, 57, 59]. In this dispersive limit, the detuning between the qubit frequency (ω_q) and the resonant SAW mode (ω_m) is large compared to g_m ($g_m \ll |\Delta|$, $\Delta = \omega_q - \omega_m$). In particular we tune the qubit frequency such that $\Delta/(2\pi) = -138.6$ MHz and $E_J/h = 8.5$ GHz. In this regime, we can approximate the Hamiltonian describing the hybrid system as ($\hbar = 1$) [10]

$$\hat{H} \simeq \omega_m \left(\hat{a}^\dagger \hat{a} + 1/2\right) + \frac{1}{2}\left(\omega_q + 2\chi_m \hat{a}^\dagger \hat{a} + \frac{g_m^2}{\Delta}\right)\hat{\sigma}_z. \tag{7.1}$$

In Eq. (7.1) the SAW degrees of freedom are described by bosonic operators $\hat{a}$ and $\hat{a}^\dagger$, and the qubit is described by the spin 1/2 operator $\hat{\sigma}_z$. By considering the transmon as a multilevel artificial atom, the total frequency shift of the qubit frequency per piezophonon, $2\chi_m$ must take into account multiple partial dispersive shifts and is therefore given by [103]

$$2\chi_m = -\frac{2g_m^2}{\Delta}\frac{\alpha}{\Delta - \alpha}, \tag{7.2}$$

where $\alpha/h = 328$ MHz is the anharmonicity of the transmon. Based on the experimental parameters of our system the qubit frequency shift per phonon at this detuning is $2\chi_m/2\pi = \ -0.97$ MHz.

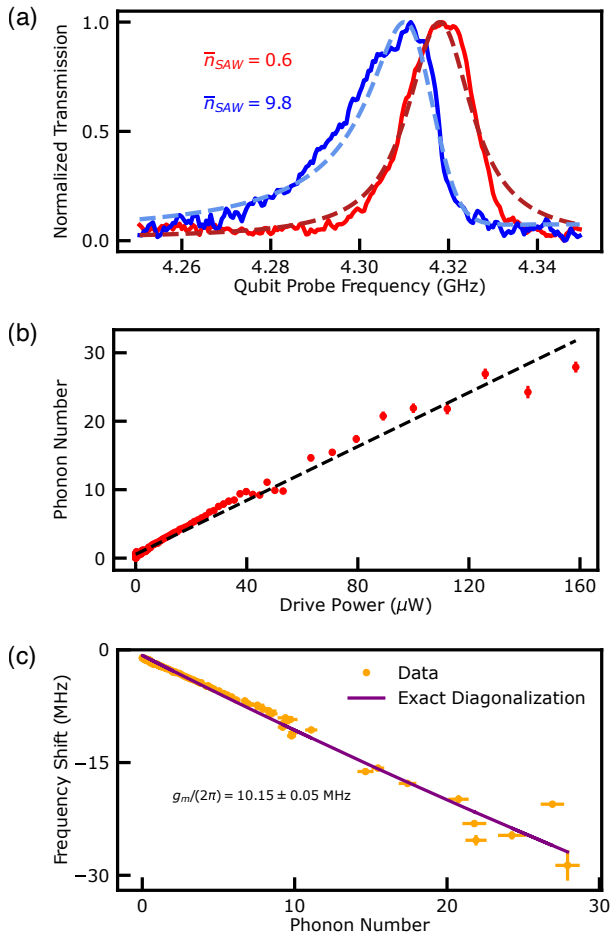

Figure 7.3: (a) Representative qubit spectra at two different applied powers near resonance with the confined SAW mode. With increasing power the qubit spectrum both shifts in frequency and inherits a spectral lineshape expected from the statistics of the acoustic coherent state. (b) Measurement of mean phonon number as a function of drive power. The extracted phonon number follows the expected linear trend (black). (c) Qubit frequency shift versus extracted mean phonon number. Exact diagonalization considers the qubit as a 5 level atom, which agrees with the experiment.

By applying a tone that is resonant with the confined acoustic mode we generate a coherent SAW state and subsequent measurement of the resulting qubit spectra allows us to determine the mean SAW resonator occupancy number. We fit the qubit spectra (see Fig. 7.3a) to a model [13] consisting of a two level system coupled to a harmonic oscillator coherent state and extract the average phonon occupation number $\overline{n}$. The asymmetry of the qubit spectra at large excitation numbers (see Fig. 7.3a) arises from the Poisson statistics of the distri-

bution of phonon numbers in the resulting SAW coherent state [5]. As shown in Fig. 7.3b we find a linear relationship between the drive power populating the SAW resonator and the extracted mean phonon number. We note that the power reported in our measurements is that applied at room temperature, which is further attentuated by 60 dB in the cryostat before entering the microwave cavity. Exact diagonalization of a multi-level Jaynes-Cummings Hamiltonian describing this coupled system allows us to extract the expected qubit frequency shift as a function of phonon number in the dispersive limit [154] and we find excellent agreement between this prediction and the measured phonon number as shown in Fig. 7.3c. In this analysis the coupling strength g_m is a fit parameter to the data and we extract $g_m/(2\pi) = 10.15 \pm 0.05$ MHz, which is in reasonable agreement with the measured value determined from fitting the avoided crossing between the qubit and SAW modes. Having calibrated the frequency response of the qubit to phonons in the confined SAW resonance, we extend these Stark shift measurements to probe the acoustic environment outside of the stop-band of the SAW mirrors. We measure the acoustic Stark shift $\delta\omega_q$ as a function of drive frequency ω_d, and extract the mean phonon occupation $\overline{n} = \delta\omega_q/2\chi_m$ over a range of drive frequencies. As shown in Fig. 7.4a, the measured phonon number has a maximum at the resonant frequency of the confined acoustic mode $\omega_m/(2\pi) = 4.4588$ GHz, and is strikingly asymmetric about this peak. The acoustic excitation spectrum hosts a rich structure near this confined resonance, making it possible for phonons across a range of frequencies to interfere with each other. Because the reflectivity of the mirrors that define the SAW cavity is relatively low ($\sim 0.5\%$ per mirror structure), the reflection process for surface phonons is distributed over the length of the cavity. This creates a situation in which phononic excitations that reflect at different spatial positions within the cavity interfere with each other either constructively or destructively depending upon their relative wavevectors and propagation

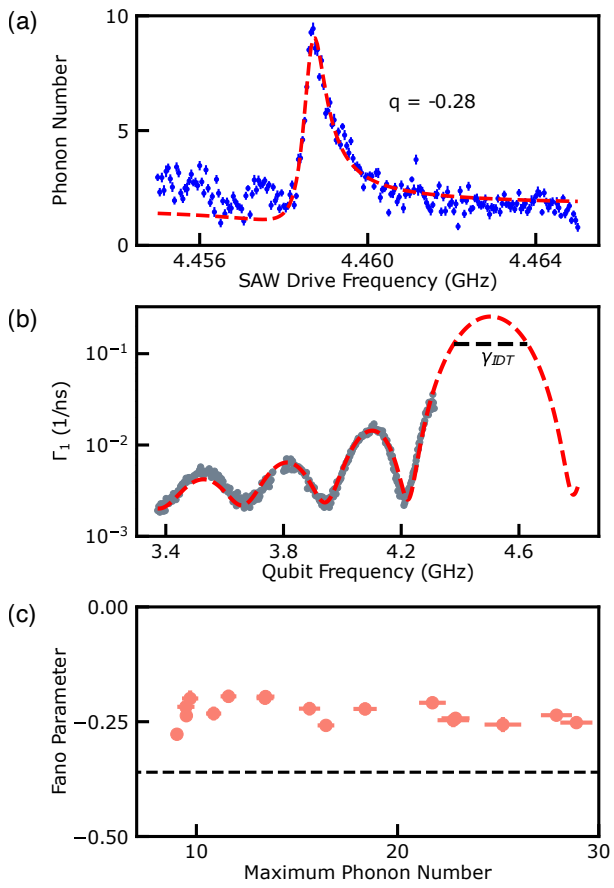

Figure 7.4: (a) Mean phonon number as a function of SAW drive frequency at a fixed power of $P_{drive} = 25\ \mu W$. The SAW resonance is asymmetric in frequency and is well-described by a Fano absorption function. The asymmetry arises from phonons in the confined acoustic mode interacting with phonons in the SAW continuum. (b) Measurement of the qubit decay rate over a broad range of frequencies far from the confined acoustic resonance. The fit (red) is to the analytical expression of the SAW-induced loss due to the central SAW transducer. The decay rate of the transducer is $\gamma_{IDT}/(2\pi) = 249.7$ MHz. (c) Fano asymmetry parameter q as a function of drive power. The horizontal error bars correspond to the uncertainty in the fit parameter $\overline{n}_{max}$ in Eq. (7.3). The black dashed line indicates q based on the analysis of two coupled harmonic oscillators as described in the text.

paths. These interference processes produce a Fano lineshape, as phonons in the confined acoustic mode are subject to differing interference with continuum surface phonons existing outside of the mirror stop-band. We model the resulting frequency-dependent phonon

number as a Fano resonance [60, 61] with an absorption spectra, $\overline{n}(\omega)$:

$$\overline{n}(\omega) = \overline{n}_{\max}\left(1 + q^2 - \frac{(q\Gamma/2 + \omega - \omega_m)^2}{(\Gamma/2)^2 + (\omega - \omega_m)^2}\right) + \overline{n}_{\text{off}}. \tag{7.3}$$

Equation (7.3) depends on the linewidth Γ, of the resonantly confined mode, the average background population of the continuum phonon modes $\overline{n}_{\text{off}}$, as well as the Fano parameter q, which describes the level of interference between the confined and lossy surface phonons. The fit parameter $\overline{n}_{\max}$ quantifies the maximum phonon number for a given measurement, which is set by the drive power. The first two terms in Eq. (7.3) do not depend on frequency and impose the physical constraint that the minimum SAW phonon number is non-negative. We note that the limit $q \rightarrow 0$ corresponds to the absence of phonon interference, and in this limit a Lorentzian response is recovered.

To determine the characteristic level of phonon interference in our device, we use the qubit to measure the phonon occupation near the confined acoustic mode as a function of the power used to populate the SAW device with phonons. By fitting each resulting phonon spectra using Eq. (7.3) we determine the Fano parameter as a function of the maximum mean phonon number. These results provide a relative measure of the acoustic interference in the device and are displayed in Fig. 7.4c. In particular, we find that the phonon interactions are well-described by Eq. (7.3), with a negative Fano parameter, down to the lowest phonon levels we are able to measure. Additionally, we find that the phonon interference is roughly constant with $q \simeq -0.25$.

To understand the interference we observe in our measurements, we compare the SAW phononic system to a minimal classical model of Fano interference arising in two coupled oscillators in which one oscillator has a significantly larger loss rate than the other [205].

In this model, the lossy oscillator approximates a continuum over the frequency scale of the confined mode (see Section 7.3) and the interaction between the two oscillators leads to Fano interference. The loss rate of the confined acoustic mode, which corresponds to the low loss oscillator, is extracted from the linewidth of the fit to the resonantly trapped SAW mode in Fig. 7.4a. This linewidth indicates that the loss of the confined mode is $\gamma_{\mathrm{SAW}}/(2\pi) = 630$ kHz, corresponding to a SAW quality factor $Q_{\mathrm{SAW}} \simeq 7000$. To estimate the loss rate of the significantly broader interdigitated transducer (IDT) response, which acts as an effective continuum over the scale of γ_{SAW}, we measure the qubit decay rate, $\Gamma_1 = 1/T_1$, as a function of qubit frequency far from the confined acoustic resonance. In this regime, the qubit loss is proportional to the electrical conductance [15, 81] of the SAW device, which is well described by only the IDT response far from the confined mode, where the mirror reflectivity is much less than one. In particular we fit Γ_1 to a phenomenological form taking into account loss resulting in the transduction of qubit excitations into phonons that exit the SAW mirrors,

$$\Gamma_1\left(\omega_q\right) = \frac{\omega_q}{Q_i} + \Gamma_0 \,\mathrm{sinc}^2\left(\pi N_p \frac{\omega_q - \omega_{IDT}}{\omega_{IDT}}\right), \tag{7.4}$$

where $Q_i = 1.05 \times 10^4$ is the qubit internal quality factor (this value is different from the previous chapter, in this chapter we have defined the qubit quality factor as $Q_i \equiv \omega_q \times T_{1i}$, where T_{1i} is the intrinsic lifetime of the qubit. The previous chapter uses the convention $Q_i \equiv f_q \times T_{1i}$), $\Gamma_0 = 0.252$ ns^{-1} is the maximum conversion rate of the qubit excitation into SAW phonons, $N_p = 16$ is the number of finger pairs in the IDT structure of the SAW resonator, and $\omega_{\mathrm{IDT}}/(2\pi) = 4.504$ GHz is the central transducer frequency, which is within 1% of the value predicted from the device fabrication parameters. By fitting the qubit

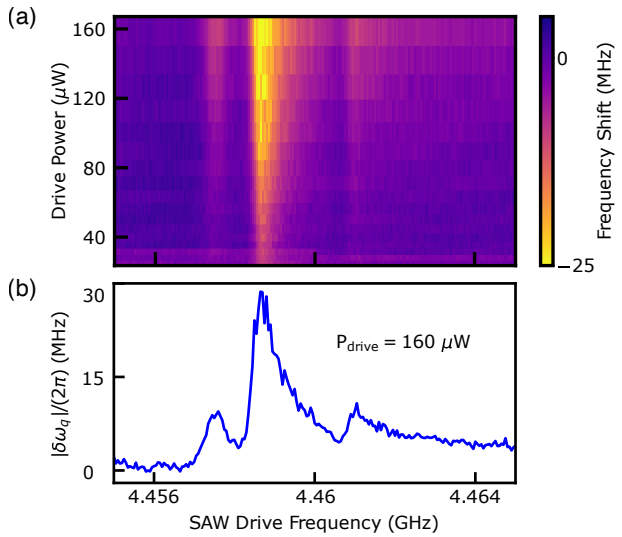

Figure 7.5: (a) Spectra of the SAW resonator inferred from the phonon-induced qubit Stark shift as a function of power. As the drive power is increased, two additional spectral features surrounding the strongly confined mode are visible, which we attribute to SAW modes that are weakly confined by the Bragg mirrors. (b) Horizontal linecut of panel (a) taken at a drive power of $P_{\text{drive}} = 160$ μW.

loss to the response given by Eq. (7.4) (see Fig. 7.4b), we are able to extract the overall loss associated with the central transducer, which we approximate as a Lorentzian with a width of $\gamma_{\text{IDT}}/(2\pi) = 249.7$ MHz. In the limit where the response of the transducers is broad in frequency compared to that of the confined mode, as is the case in our experiments ($\gamma_{\text{SAW}}/\gamma_{\text{IDT}} \approx 0.3\%$), the Fano parameter can be calculated as [205],

$$q = \frac{1}{\gamma_{\text{IDT}}\ \omega_{\text{SAW}}} \left(\omega_{\text{SAW}}^2 - \omega_{\text{IDT}}^2\right). \tag{7.5}$$

Based on the experimental parameters this model predicts $q = -0.36$, which is indicated by the black dashed line in Fig. 7.4b. The systematic deviation between the experimentally determined and predicted values of q could arise from the presence of additional mechanical modes near the confined SAW resonance. In fact, in our higher power measurements shown in Fig. 7.5(a,b) we observe evidence for the existence of such modes on either side of the

strongly confined SAW resonance. These modes also exhibit asymmetry, indicating that they are also interfering with the continuous phonon background. Since the calculated free spectral range of the SAW resonator is comparable to the width of the mirror stop-band, it is likely that these additional modes correspond to surface acoustic waves weakly confined within the SAW cavity (see Section 7.3).

7.5 Coupling to transverse bulk phonons

At this point, we have seen how the interaction between different types of phonons is important for understanding quantum acoustic systems. Even when specific types of mechanical excitations are designed (like the surface phonon excitations in the previous section), the possibility of other, naturally occurring phonon modes exist and can effect device performance. Because the experiments described in this thesis use a relatively strong piezoelectric material ($LiNbO_3$), it is natural for us to consider the possibility of other types of mechanical excitations within our system as well. This section details how our device geometry supports transversely polarized bulk phonons that are excited via the large dipole moment of the device on lithium niobate and how they couple to the cQED system in our experiments. Furthermore, as we shall see, we are able to perform contact-less excitation and measurement of these acoustic excitations and their coupling to the microwave cavity even at room temperature.

Quantum acoustics systems, in which superconducting qubits are interfaced with mechanical degrees of freedom offer a promising platform for quantum information science, as mechanical resonators having a small spatial footprint and long coherence times can be straightforwardly fabricated. By engineering hybrid quantum systems in this fashion, it

possible to design quantum memory protocols [20], implement microwave-to-optical transduction schemes [27, 34], and operate the qubit as a sensor [16, 68]. The ability to leverage mechanical degrees of freedom at the level of single, or few phonons, makes them promising candidates for quantum information processing, with recent experimental results demonstrating the creation of phononic Schrödinger cat states [52], the joint entanglement of high-frequency mechanical oscillators [50], and the ability to simulate open quantum acoustic systems [15]. However, the relatively large and geometrically complex structures typically used in quantum acoustics devices can host a litany of other mechanical modes that may have spurious coupling to the electromagnetic degrees of freedom of the quantum circuit. Identifying and understanding these couplings is vital for high-fidelity control of the device degrees of freedom, but also opens the door to coupling simultaneously to multiple distinct types of phononic excitations in a single architecture. On the other hand, when they are poorly controlled, these modes can act as unwanted decoherence channels for the quantum systems of interest. Optimization of device geometry allows for the mitigation of these unwanted couplings and methods for improving the coherence of quantum acoustic systems. In this work, we demonstrate a hybrid system that enables the interaction between a microwave cavity and natural *bulk transverse* substrate phonons in Y-cut lithium niobate. By integrating this hybrid electromechanical system with a superconducting qubit, we are able to tune the cavity frequency via its dispersive interaction with the qubit, enabling measurement of the coupling between the cavity and high-frequency overtones of the acoustic mode. These transverse acoustic modes are directly excited via the free-space coupling of the device dipole to the 3D microwave cavity housing the devices and at low temperature we find that they exhibit coupling to the qubit-cavity system with an interaction strength comparable to the decay rate of the hybrid device. Additionally we find that similar devices, in which the qubit

is removed, enable contact-less coupling to these naturally occurring transverse modes with a coupling that persists to room temperature (cf. Ref. [206]).

The experimental results reported here were obtained using a flip-chip hybrid quantum acoustic device originally designed to investigate the coupling of a flux tunable transmon qubit, fabricated on silicon, to a surface acoustic wave (SAW) resonator, fabricated on *YZ*-lithium niobate [15, 16]. These previous experiments reached the strong coupling regime of quantum acoustics, with a mechanical coupling strength of $g/(2\pi) \approx 10$ MHz between the qubit and SAW modes. In the present manuscript, we report on experimental work demonstrating the existence of additional *bulk* phononic modes in the lithium niobate chip and how their direct coupling to the resonant mode of a 3D microwave cavity is mediated by the dipole moment of the device. Due to the dispersive interaction between the cavity and the qubit [11], these bulk acoustic modes also indirectly interact with the qubit. As shown in Fig. 7.6(a), the qubit and phononic chips are coupled purely capacitively to each other via large $(250\ \mu\text{m})^2$ antenna pads on either substrate that form a set of parallel plate capacitors when the devices are vertically aligned and adhered together using standard flip-chip techniques [207]. The flip-chip stack is mounted in a copper 3D electromagnetic cavity to control and measure the coupled devices (see Fig. 1 (a)). The antenna pads on the qubit and phononic chips serve dual purpose, enabling the coupling between the devices as well as serving as a coupling mechanism between the electric field in the microwave cavity and either device independently [16]. As we will describe below, these macroscopic antenna pads also introduce an unintended and surprisingly strong coupling to high-overtone bulk phononic excitations, with harmonic number beyond 1000, in the lithium niobate substrate.

To experimentally investigate the coupling of the microwave cavity to these modes we measure the microwave transmission S_{12} through the 3D microwave cavity at a relatively

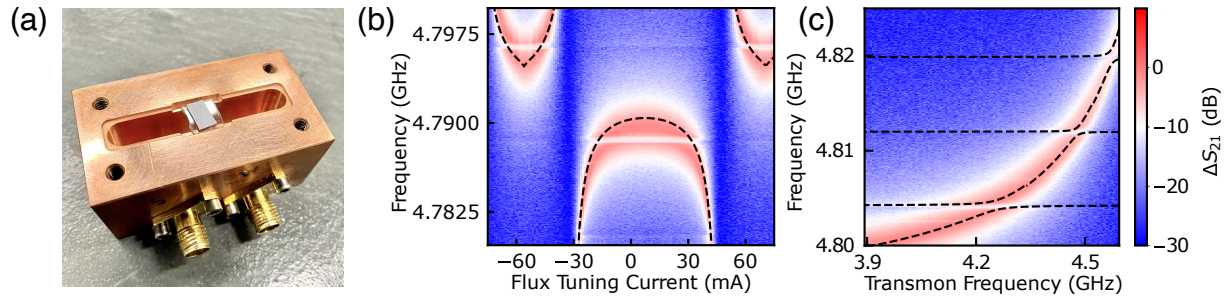

Figure 7.6: (a) Image of the composite flip-chip stack in the bottom half of the 3D microwave cavity used to probe the properties of the system. (b) Spectroscopy of the hybrid qubit-cavity system as the qubit frequency is tuned via the magnetic flux through an external superconducting coil. The qubit and cavity are coupled with an interaction strength of $g/(2\pi) = 73 \pm 2$ MHz (black dashed line). Additional coupling between the hybrid system and bulk acoustic modes is observed as horizontal features at constant frequency, which are largely independent of the external magnetic flux. (c) Spectroscopic data over a tighter frequency range demonstrating clear avoided crossings between the qubit-cavity system and the acoustic modes. The fit to the data (dashed black lines) represent a coupled oscillator model used to extract the coupling strengths (see Fig. 7.7).

low input power ($P_{\text{input}} \approx -110$ dBm) as we tune the qubit frequency via an external magnetic flux. As shown in Fig. 7.6(b), when the resonant frequency of the qubit is tuned across an entire flux quantum, the qubit and cavity modes undergo an avoided crossing, which can be used to extract a coupling strength of $g/(2\pi) = 73 \pm 2$ MHz between the two modes. As seen in Fig. 1(b) the cavity transmission also exhibits a series of avoided crossings, indicating coupling to additional modes, which appear as horizontal breaks in microwave transmission, and are largely independent of external magnetic flux. By zooming in on several of these additional avoided crossings in Fig. 7.6 (c) the transmission data are fit to a coupled oscillator model to extract the interaction strength between the qubit-cavity mode and these additional weaker resonances. In the top panel of Fig. 7.7 we present the fitted coupling rates $g_m/(2\pi)$ for the five anti-crossings that are within a few line-widths of the resonant frequency of the microwave cavity. The bottom panel of Fig. 7.7 shows how the coupling to these modes manifests in the bare cavity transmission when the cavity is

flooded with a large number of photons ($P_{\text{input}} \approx -60$ dBm) [141]. Even when the cavity is populated with many photons, and the qubit state no longer dispersively shifts the cavity resonance, the presence of these additional modes is still strongly imparted on the cavity spectrum as "notches" in the measured transmission.

Additional acoustic modes in the strongly piezoelectric lithium niobate substrate are a natural explanation for these additional resonances, which couple to the hybrid qubit-cavity system. In fact, periodically notched spectra, similar to the one shown in the bottom panel of Fig. 7.7, have been recently been observed in the transmission of microwave cavities coupled to high-overtone longitudinal phononic modes in quartz [208]. Additionally, high-overtone bulk acoustic resonators (HBARs), using a variety of piezoelectric materials, have been shown to strongly couple to superconducting qubits in quantum acoustics architectures [3, 28, 52, 59, 148, 149, 151, 209]. Furthermore, as we describe below, we use a combination of finite element modeling (FEM) and additional characterization measurements to verify the nature of these bulk acoustic modes, their polarization, as well as their coupling mechanism to the hybrid qubit-cavity system.

As shown in the COMSOL Multiphysics simulations presented in Fig. 7.8(a), the time-varying electric field within the microwave cavity will impinge on the large-scale aluminum antenna pads on the surface of the lithium niobate chip. These two pads function as an electric dipole and the mobile charges in these metallic pads screen the cavity electric field, locally polarizing the substrate. As a consequence of the piezoelectric effect, this polarization creates strain within the lithium niobate substrate. If the frequency of the time-varying electromagnetic cavity field is resonant with a natural mechanical mode imposed by the geometry of the substrate and the speed of sound in lithium niobate, the generated strain will excite acoustic oscillations that will resonate within the bulk of the material. In this

fashion, the dipole antenna on the lithium niobate chip enables the interaction between the cavity mode and bulk phonon modes in the substrate. Furthermore, since the resonant frequency of the cavity can be weakly flux-tuned via its dispersive interaction with the qubit, this device architecture allows us to measure the interaction between the cavity mode and acoustic modes over a frequency range larger than the cavity line-width. To determine the

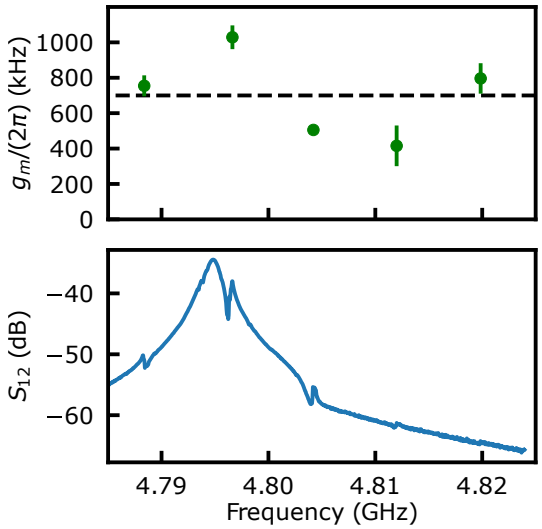

Figure 7.7: Top: Coupling strength, $g_m/(2\pi)$ between the microwave cavity and five overtone bulk mechanical modes. Bottom: Measurement of the cavity spectrum at large input power ($P_{\text{input}} \approx -60$ dBm) demonstrating that the transmission is independent of the qubit state as described in the main text. Coupling to the acoustic modes manifests as characteristic "notches" in the cavity transmission.

exact nature of the acoustic modes being excited by this dipole-coupling to the cavity field, we use COMSOL simulations to find the mechanical eigenmodes of the Y-cut lithium niobate substrate as well as their polarization [152]. These simulations reveal the existence of both longitudinal and transverse acoustic modes. In order to model the effect of the cavity electric field, we apply a time-varying voltage difference across the chip in the x-direction of the substrate in these simulations (see Fig. 7.8(a)). In the presence of this external electric field, the symmetry of the combined electromechanical system only supports mechanical modes that mirror the symmetry of the external electric field, and thus we find that only transversely

polarized mechanical modes can be excited (see Fig. 7.8(b) for the spatial structure of the $n = 5$ mode). In particular, the results of the simulations reveal a transverse mode having fundamental frequency $f_1 = 3.5784$ MHz propagating along the y-axis of the substrate. We note that the simulations enforce that the mechanical displacement field is equal along the two edges of the substrate parallel to the x-axis. The fundamental frequency of the transverse mode, and its harmonics, are related to the speed of bulk transverse sound in lithium niobate v_t and the thickness of the chip:

$$f_n = \frac{n v_t}{2t}, \tag{7.6}$$

where n indexes the harmonic number and $t = 500$ μm is the thickness of the substrate used in our experiments and simulations. The speed of transverse sound within the bulk lithium niobate is related to the material properties of the substrate via Hooke's Law:

$$C_{44} = \rho v_t^2, \tag{7.7}$$

where $C_{44} = 5.95 \times 10^{10}$ Pa is the appropriate elastic constant for transverse mechanical waves in Y-cut lithium niobate and $\rho = 4647$ kg/m^3 is the mass density of the material [210]. Eqn. 7.7 gives the speed of transversely polarized bulk sound as 3578 m/s, consistent with Ref. [211], and a corresponding free spectral range of $\Delta f_n = 3.578$ MHz between adjacent acoustic modes. When a spatially uniform external electric field (E_{ext}) is applied across the substrate, as is the case for the cavity field in the vicinity of the dipole antenna on the lithium niobate chip in our experiments, the piezoelectric coupling g_{em} is proportional to the overlap integral between the electric and strain fields [208]:

$$g_{\text{em}} \propto \int_V E_{\text{ext}} \; S(\vec{r}) \; \mathrm{d}V, \tag{7.8}$$

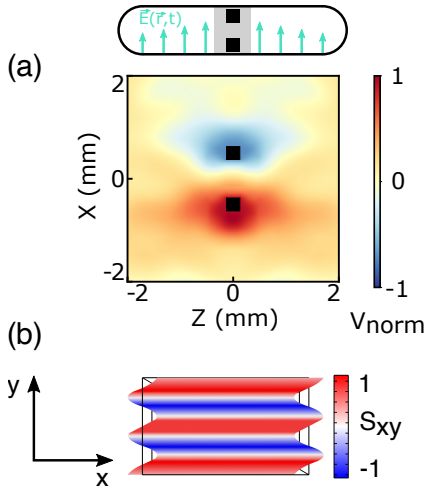

Figure 7.8: a) Top: Schematic indicating the orientation of the time-varying electric field of the 3D microwave cavity. Bottom: COMSOL simulation of the induced normalized voltage on the surface of the lithium niobate substrate when the system is driven at the fundamental frequency of the transverse mode $\omega/(2\pi) = 3.5784$ MHz. The black squares represent the antenna pads, and the profile of the induced voltage has a dipole spatial structure. (b) FEM simulation of the transverse strain S_{xy} associated with the 5^{th} harmonic of the transverse bulk acoustic mode.

where $S(\vec{r})$ is the spatially varying strain field within the chip and the integral is taken over the entire volume V. The y-dependence of the strain field for transverse phonons is given by $S(y) = S_0 \sin\left(\frac{2\pi y}{\lambda n}\right)$, where S_0 is the amplitude of the strain. For the n^{th} harmonic of the transverse mode having wavelength $\lambda_n = 2t/n$, Eqn. 7.8 predicts non-zero coupling for odd-indexed modes only. This implies that in our experiments the 3D microwave cavity electric field should couple only to every other transverse phonon mode, leading to an effective free spectral range $2 \times f_n \simeq 7.16$ MHz based on the fundamental frequency determined from the FEM simulations. This matches (to within 10%) the measured free spectral range determined from the spacing of adjacent notches in the microwave cavity transmission shown in Fig. 7.7. Based on the calculated free spectral range of the bulk acoustic modes and the cavity frequency, we can reliably excite bulk mechanical excitations with mode number $n \simeq 1339$ that couple to the qubit.

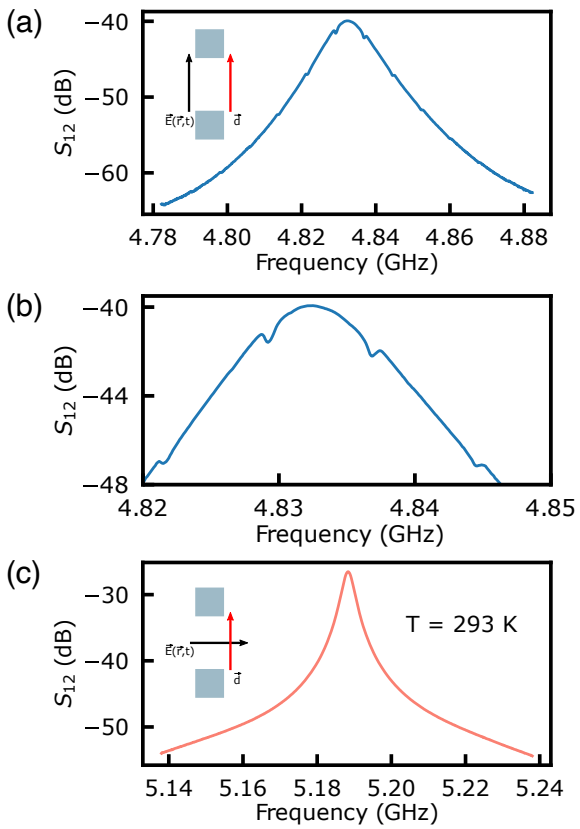

Figure 7.9: Room temperature characterization of the transverse acoustic modes. (a) When the dipole moment of the metallic pads ($\vec{d}$) is parallel to the cavity electric field, coupling is observed between the cavity mode and the acoustic modes of the substrate. (b) Zoomed in cavity transmission from (a) near the cavity resonance. The coupling to the bulk acoustic modes is apparent as "notches" in the cavity transmission. (c) When the $LiNbO_3$ substrate is oriented such that the dipole moment is perpendicular to the cavity field, no coupling between the two systems is observed. The shift in the cavity frequency between panels (a,b) and (c) arises from the large anisotropy of the lithium niobate dielectric tensor [210].

In addition to spectroscopy measurements at cryogenic temperatures, we also performed additional characterization experiments at room temperature to investigate these transverse bulk acoustic modes, and their coupling to the microwave cavity. In particular, to further elucidate the coupling of the cavity field to the dipole formed by the metallic antenna pads, we fabricated an additional device having only large antenna pads on a separate Y-cut lithium niobate chip and loaded it into a second 3D microwave cavity. As shown in Fig. 7.9(a,b) the appearance of the notches in the cavity transmission clearly persist even at room tempera-

ture, albeit with a reduced amplitude. These measurements serve to reinforce the conclusion that the 3D cavity enables a method for contact-less excitation of these high-overtone acoustic modes. Additionally, we find that when the sample is rotated by 90° in the cavity, the notches in the microwave transmission disappear indicating that the coupling to the transverse modes vanishes (see Fig. 7.9(c)). In this configuration the dipole moment of the device is perpendicular to the cavity electric field and cannot induce a polarization between the pads, nor the reciprocally generated transverse strain field via the piezoelectricity of the substrate. This rotation dependence is consistent with the conclusions we draw from the FEM simulations of the device and further verify that the dipole coupling between the pads and the cavity field are responsible for exciting the transverse modes of the lithium niobate chip. Finally, comparing Fig. 7.9(a) with Fig. 7.9(c) clearly shows that the microwave cavity line-width is significantly broadened when the lithium niobate chip is oriented such that the antenna pads are aligned to the cavity field. In particular, we find that in this configuration the cavity quality factor is decreased by a factor of approximately 3.75, from $Q \simeq 1500$ to $Q \simeq 400$, relative to the configuration in which the pads are orthogonal to the cavity field. To understand the origin of these additional loss, we tested bare lithium niobate chips having the same dimensions but without the metallic antenna pads. Unsurprisingly, in these additional control samples we do not observe any coupling between the the cavity field and bulk acoustic modes regardless of the orientation of the chip in the microwave cavity (i.e. no cavity notches are observed). Interestingly, however, we find that the cavity quality factor is $Q \simeq 1500$ regardless of the chip orientation, strongly indicating that the reduction in the cavity quality factor observed in Fig. 7.9(a,b) arises from the mechanical loss associated with the transverse phonon modes. Finally we note that the quality factor of the cavity in the low-temperature measurements presented in Fig. 7.7(b) is $Q \simeq 2500$ indicating a reduction

of the mechanical losses when the lithium niobate chip is cooled to cryogenic temperatures.

We have demonstrated the capacitive dipole coupling between a hybrid 3D cavity system and high-overtone transverse bulk acoustic modes in Y-cut lithium niobate. These transverse acoustic modes are excited by the microwave field of the 3D cavity and detected as absorption features in the cavity transmission. The coupling to the acoustic modes is found to be comparable to other losses in the hybrid system, reinforcing the importance of understanding the role of unintended mechanical modes in quantum acoustic systems proposed for quantum applications. Beyond quantum acoustics, we find that this contact-less method of acoustic excitation and detection in our devices persists to room temperature, highlighting the utility and versatility of 3D cavities for characterizing the frequency response and mechanical losses in piezoacoustic devices in general.

7.6 Conclusion

In conclusion, we have demonstrated the existence of additional phonon modes in our device and how they couple directly to the qubit or to the microwave cavity itself. In particular, we have demonstrated the Fano interference of surface acoustic wave phonons in a hybrid quantum acoustic device containing a resonantly confined SAW mode embedded in a continuum of surface phonons. This phononic interference is inferred from qubit-assisted spectroscopy of the SAW device and we find that it persists down to extremely low excitation number. The experimental results are in excellent agreement with the functional form of a Fano resonance and highlight the importance of phononic interference in quantum acoustic devices proposed for applications in quantum information processing. Additionally, we measure and characterize transversely polarized bulk phonons that strongly couple to the microwave cavity that

houses the hybrid quantum acoustics system. We are able to integrate room temperature measurements of these bulk phonons with FEM simulations to characterize the additional excitations within the system. This chapter highlights the importance of considering all possible types of phononic excitations to more completely characterize quantum acoustic systems.

Chapter 8

Vantablack Shielding of Superconducting Qubits

8.1 Introduction

This chapter describes a set of experiments not directly related to quantum acoustics. These experiments were directed at understanding a new material, Vantablack, as a radiation absorbing coating to improve coherence of cQED systems. Superconducting qubits are among the state of the art technologies being developed in the pursuit of a functional quantum computer [104, 212, 213], with current depolarization and dephasing coherence times for transmon-based processors exceeding 100 μs [214], and recent experiments employing heavy fluxonium [124] demonstrating coherence times up to 1 ms [126]. One of the primary sources of decoherence in modern superconducting processors is the presence of non-equilibrium quasiparticles (broken Cooper-pairs) in the in the superconducting electrodes that form the circuit [127, 215, 216]. It is well known that stray black-body infrared (IR) radiation, which has energy greater than the superconducting gap, can break Cooper pairs in the superconductor, increasing the density of non-equilibrium quasiparticles, and poisoning coherence [132, 217, 218]. Additionally, it has been found that effectively shielding the system from these IR photons improves in the internal quality factor of the superconducting res-

onators employed for qubit control and readout [219]. In order to further increase qubit coherence times it is important to continue to investigate new methods and materials for shielding superconducting qubits and resonators from unwanted sources of decoherence. In this chapter, we investigate the performance of a new IR shielding material: *Vantablack* [220]. Our preliminary results indicate that Vantablack has potential to yield performance beyond standard coatings when properly applied.

8.2 Experimental details

Vantablack is a coating composed of vertically aligned nanotube arrays, grown via a modified chemical vapor deposition process, and exclusively developed by Surrey NanoSystems Ltd [220]. It is one of the darkest substances known, reflecting less than 0.2% of light in the visible spectrum. These extraordinary absorbing characteristics extend into the infrared spectrum, where Vantablack reflects less than 0.5% of IR photons [221]. Vantablack is found in many light absorbing applications, including commercial thermal imaging systems [222] as well as beam dumps for high power optical experiments [223].

To investigate the performance of this shielding material in the context of superconducting qubit systems we measure the coherence properties of a single-junction transmon qubit housed in a three-dimensional (3D) microwave cavity [103]. In cQED experiments, such as the ones we perform, it is common to enclose the experimental setup in a shielding material that protects both the control/readout resonator and qubit from stray black-body radiation. In our experiments, this is achieved by housing the qubit and resonator in a copper cylinder coated internally with the shielding material, and then thermally anchoring the cylinder to the mixing chamber of a dilution refrigerator having a base temperature of $\simeq 10$ mK, which is

much less than the effective temperature associated with the qubit transition frequency (approximately 250 mK). To compare the performance of Vantablack to a standard epoxy-based coating, which serves as a control experiment, we cover the inside of two identical copper cylinders in either a standard IR coating or Vantablack as shown in Fig. 8.1a. The standard infrared absorbing coating we use for our control experiment is composed of a mixture of (by mass) 68% Stycast 2850FT epoxy, 5% Catalyst 24LV, 7% carbon lamp black, and 20% 175 μm diameter glass beads. This particular type of epoxy-based coating is often referred to as *Berkeley Black* [224] and has been used in previous microwave circuit experiments to produce systematic improvements in the quality factor of superconducting resonators [219]. Then, on two-separate cool-downs of the dilution refrigerator, we place the same microwave cavity and qubit into one of these two copper cylinders and measure the coherence properties of the qubit.

Both the control and readout of the qubit, which has a frequency $\omega_q/2\pi = 5.165$ GHz, are mediated via the electric field of the TE101 mode of the 3D electromagnetic resonator with frequency 6.936 GHz (see Fig 8.1b.) [117]. For a given measurement, microwave pulses of appropriate length and amplitude are used to manipulate the state of the qubit. After a specified amount of free-evolution, the state of the qubit is then inferred via measurement of the transmission through the microwave cavity, which is dispersively shifted by the presence of the qubit [10]. In particular, we employ a high-fidelity readout protocol based on the non-linearity of this interaction [141–143]. A more detailed description of the relevant microwave circuit and qubit measurement protocols can be found in Ref. [129].

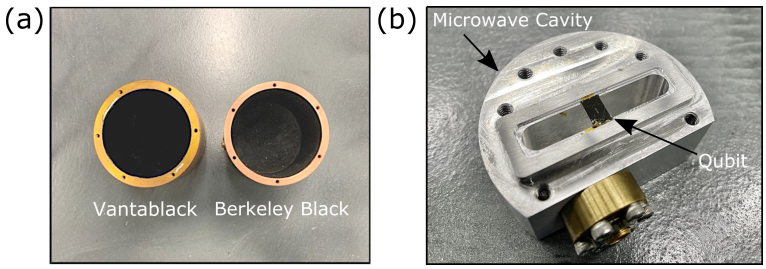

Figure 8.1: (a) Cylindrical copper housings containing the 3D microwave cavity and superconducting qubit. The interior of these cylinders is coated with either a Vantablack (left) or a Berkeley Black (right) coating. (b) Bottom half of the 3D microwave control/readout cavity and transmon qubit, which was fabricated on high resistivity silicon.

8.3 Results and discussion

To characterize the effectiveness of the coatings at mitigating loss, we measure the depolarization time T_1 and the dephasing (Ramsey) time T_2^* of the qubit in the copper housings covered in Berkeley Black and Vantablack. In Fig. 8.2 we show representative measurements of both T_1 and T_2^* for the qubit housed in the Vantablack coated shield as well as the accompanying microwave pulse sequences applied to perform these measurements. Because the measurement of the Ramsey decay time is a phase sensitive measurement, a detuning Δ between the drive frequency and ω_q will lead to a decaying sinusoid rather than a decaying exponential function. This allows us to extract the magnitude of the detuning between the drive frequency and the qubit frequency in addition to the dephasing time of the qubit.

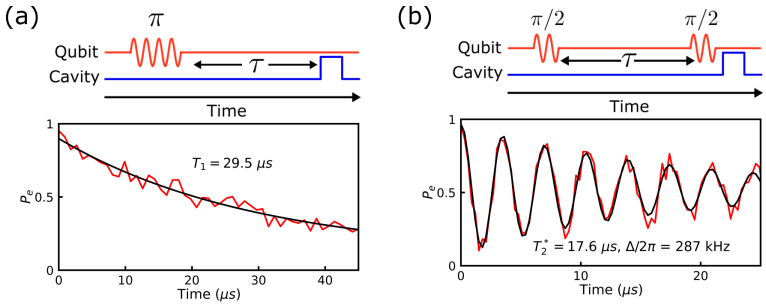

Figure 8.2: (a) Microwave pulse sequence to measure T_1 (top) along with a representative measurement (bottom). (b) Microwave pulse sequence to measure T_2^* (top) and a representative measurement (bottom). As described in the text, a detuning $\Delta/2\pi = 287$ kHz separated the drive frequency and ω_q in these measurements.

It is well known that qubit coherences can fluctuate over long timescales due to interactions with quantum two level systems [225–229] as well as stray radiation from sources such as cosmic rays [186, 230]. Therefore in order to quantify qubit decoherence, we perform repeated measurements of both T_1 and T_2^* to obtain sufficient statistics to understand the performance of the two coatings relative to one another. Specifically, we interleave T_1 and T_2^* measurements over a 16 hour period and each measurement contains 252 points in time with 100 averages at a repetition rate of 9 kHz. This allows us to extract T_1 and T_2^* at a rate of approximately $(5\text{ s})^{-1}$. From these measurements we extract the pure dephasing time of the qubit,

$$T_\phi = \left(\frac{1}{T_2^*} - \frac{1}{2T_1}\right)^{-1} \tag{8.1}$$

and compare the resulting distributions between the two experiments with different shielding materials. The measured probability distributions for both T_1 and T_ϕ for the qubit system shielded by Vantablack and Berkeley Black coatings are plotted in Fig. 8.3. In order to compare probability distributions of these coherence measurements, we divide each histogram bin by the total number of experiments to normalize the histograms to have area equal to one. The average values $\overline{T_1}$ and $\overline{T_\phi}$ obtained from each distribution are listed in Table 8.1 demonstrating a similar level of coherence in both experiments and indicate that Vantablack is a compatible coating with cQED experiments.

Coating	$\overline{T_1}$ (μs)	$\overline{T_\phi}$ (μs)	P_e(%)
Vantablack	22.9 ± 5.6	29.7 ± 14.9	3.2 ± 0.59
Berkeley Black	27.5 ± 8.3	45.9 ± 41.2	0.5 ± 0.17

Table 8.1: Averaged results from the qubit coherence distributions shown in Fig. 8.3 and their standard deviations. P_e represents the thermal population of the excited state of the qubit as described in the main text.

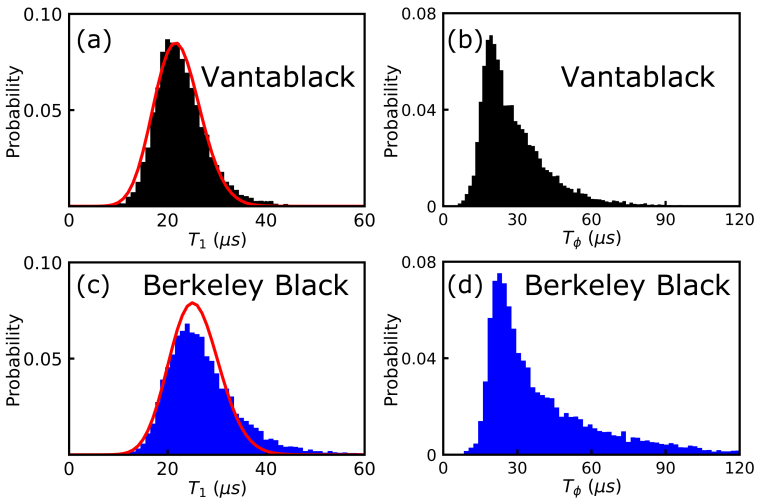

Figure 8.3: Probability distributions of both T_1, along with fits to Poisson distributions (red curves), and T_ϕ in either the Vantablack coating (a,b) or the Berkeley Black coating (c,d).

While there does not seem to be a large difference between $\overline{T_1}$ in either shielding environment, it is noteworthy that the average depolarization time in the Berkeley Black environment is slightly longer. Uncorrelated losses of qubit excitations will manifest as a Poissonian distribution in T_1 [231], which we find in both sets of measurements regardless of coating. Because the distribution of T_1 measurements is governed by Poisson statistics, a larger mean will also lead to a skewed distribution towards higher values of T_1, which is consistent with the slightly higher value observed in experiments using Berkeley Black as a coating.

In order to further investigate the differences in performance between these two coatings we measure the residual excited state population of the qubit using a method described in Refs. [127, 128], which can be interpreted as an effective qubit temperature. As shown in in final column of Table 8.1 we find that the qubit system housed in the Vantablack coating has a residual excited state population of 3.2% as compared to 0.5% in the Berkeley Black coating. This maps onto an effective qubit temperature of 72.6 mK (Vantablack) and 46.6 mK (Berkeley Black). Using the principle of detailed balance, we are able to calculated

the rate at which spurious excitations in the system drive the qubit from its ground to excited state,

$$P_g \Gamma_\uparrow = P_e \Gamma_\downarrow, \tag{8.2}$$

where P_g and P_e are the residual population of the qubit ground and excited states, respectively. $\Gamma_\downarrow = 1/\overline{T_1}$, and $\Gamma_\uparrow$ is the rate at which the qubit is driven from the ground to excited state. We find that in Vantablack, $\Gamma_\uparrow \simeq 1.4 \times 10^3/\text{s}$, and in the Berkeley Black coating, we find that $\Gamma_\uparrow \simeq 0.19 \times 10^3/\text{s}$. Two primary mechanisms may be responsible for the difference in spurious excitation rate between the two coatings. First, the qubit temperature between the two experiments could differ slightly, perhaps due to a relatively low thermal conductivity for Vantablack versus Berkeley Black at mK temperatures. In order to test such a hypothesis, more extensive studies of the thermal properties of Vantablack are necessary. Alternatively, and more interestingly, the density of stray photons present in the Vantablack shielded environment could be higher than in the housing coated in Berkeley Black, indicating that the performance of Vantablack is inferior to that of Berkeley Black. These preliminary measurements do not allow us to unambiguously disentangle these two possibilities and future experiments optimizing the Vantablack coating are needed to identify which may be causing the increased rate of qubit excitation.

In particular, although Vantablack has an extremely low reflectivity at wavelengths in the IR range, it is known that increasing the thickness and roughness of light-shielding coatings can further decrease the reflectivity of a coating. In particular, Ref. [224] reports a $\sim 30\%$ reduction in IR reflectance upon increasing the thickness of commercially available coating (Chemglaze Z306) from 25 μm to 100 μm. Vantablack is created as a relatively thin coating, with thickness ranging from 20 μm to 50 μm [221]. Assuming a similar scaling with thickness

would reduce the IR reflectance of Vantablack from 0.5% to 0.35%. For comparison Berkeley Black has a typical application thickness near 100 μm, or more, with the addition of glass beads which provide extra scattering sites for stray photons. This leads us to believe that the addition of extra materials into Vantablack that increase the scattering of stray photons may improve qubit performance in future experiments using Vantablack as a IR shielding material.

8.4 Conclusion

In conclusion, we have investigated of the utility of Vantablack as a novel shielding material on the coherence properties of a superconducting qubit system. We find that Vantablack does not significantly negatively impact the measured coherence properties of the qubit. It could, however, lead to a higher effective qubit temperature and therefore higher rate of spurious qubit excitation. However, future experiments are needed to more completely understand the potential of this material in improving the state-of-the-art. In particular, future experiments in which high-frequency microwave and IR radiation can be controllably injected are needed to systematically study qubit coherence as a function incident power [217]. Similarly, planar superconducting qubit geometries have a much smaller mode volume, and are much more sensitive to surface losses [117], and may respond more dramatically to changes in the IR shielding environment. Building upon the initial experiments reported here, these future experiments can advance the understand of Vantablack as an IR shielding material for cQED systems based in superconducting circuits.

APPENDIX

Appendix A

Flip-chip device assembly procedure

One of the primary technical accomplishments of this thesis was the integration of a "flip-chip" procedure to implement the capacitive coupling between the transmon qubit and the high-frequency SAW resonator (see Fig. 6.2). The fabrication of both the qubit and the SAW resonator follow standard nano-fabrication procedures (the details of which can be found in the Ph.D. thesis of Dr. Justin Lane in Ref. [122]). Once both the qubit and SAW resonator are fabricated, the next step needed to create a hybrid cQAD system is to implement the coupling between the two devices via a flip-chip procedure. This appendix describes how we adhere the two chips together spatially, allowing for the strong coupling between qubit and mechanical modes necessary for the primary results of this thesis.

Hard-baked resist spacers

When designing a quantum acoustics device, we want to specify some nominal coupling between the two chips. We choose to do this by fabricating spacers made of hard-baked photoresist on the chip containing the SAW wafer (we choose not to fabricate the spacers on the qubit chip to minimize the chance of accidentally destroying the Josephson junctions with extra fabrication steps). We spin-coat four individual layers of S1813 resist at a speed of 5000 RPM for 50 seconds on the wafer containing the SAW chip. With this spin speed, the nominal thickness of each layer is $\simeq 1.3$ μm, creating a total resist thickness of 5.2 μm.

Between each step of spin-coating, we bake the wafer on a hotplate at 110°C for 1 minute. We then expose the resist to UV light for 90 seconds using a standard mask aligner, and develop the exposed resist in 352-developer for $\simeq 45$ seconds. At this point, the chip should have a functioning SAW resonator as well as the pattern of developed S1813 resist nominally 5.2 μm thick. In order to make the resist robust for further fabrication steps, we then set the hotplate to 250°C and bake the sample for 90 minutes. This sufficiently hardens the resist so that it will not easily come off the sample even when exposed to solvents. At this point, the qubit and SAW chips are ready for the flip-chip procedure.

Flip-chip coupling

Our current flip-chip assembly procedure relies on the use of a custom-made mask (we refer to it as the "flip-chip mask") compatible with the mask aligner in the Keck Microfabrication facility (KMF) cleanroom. The mask consists of a plate with two small vacuum holes (see Fig. A.1). These holes are connected to the "ball lock" vacuum lines on the mask aligner by use of a vacuum tee. This allows us to vertically suspend a small chip (we use the chip containing the SAW resonator) upside down and align the antenna pads on the SAW chip with the antenna pads on the qubit chip. We use transparent wafers for the SAW chips (either double side polished lithium niobate or quartz), so that we can see *through* the SAW chip to the qubit chip underneath. Moving forward, it may be useful to fabricate the qubit chip on a transparent substrate (such as sapphire), so that either chip can be used as the "top chip". In order to make sure that the two chips actually stick together, we use a fine-tip needle to place two small drops of resist on the qubit chip (note: essentially no drop of resist is too small for this step, I've often noticed that drops too large in size can both cause a

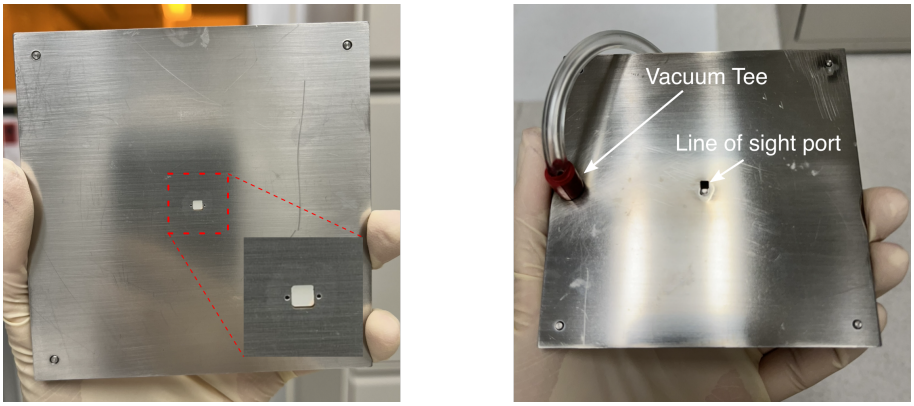

Figure A.1: Left: Bottom side of the flip-chip mask. The dimension of the mask is approximately 4 × 4 inches, which is compatible with our mask aligner. Inset: Zoomed in image of the line of sight port and the vacuum holes that allow us to suspend a substrate upside down. Right: Top side of the flip-chip mask. The vacuum tee that connects to the lines on the mask aligner is indicated on the left side of the image while the line of sight port is indicated at the center of the mask.

mess and cause the chips to be spaced very far apart from each other). Once the gluing resist has been placed on the qubit chip, we mount the qubit chip on the sample stage of the mask aligner. We then connect the flip-chip mask to the necessary vacuum lines and place the SAW chip on the flip-chip mask such that the sample is held to the mask via the custom vacuum ports (see Fig. A.1, left panel). We mount the flip-chip mask to the mask aligner (make sure to have the vacuum tee facing *towards you* when you mount the mask, otherwise the tee will interfere with the microscope attached to the mask aligner). We then adjust the bottom chip (the qubit chip) using the four axis control of the sample stage. Once the large antenna pads of the qubit and SAW chips are laterally aligned, we move the qubit chip vertically upwards until it makes good contact with the SAW chip (you can tell the contact is good by moving the qubit chip downwards, if the resist on the qubit chip is in contact with the SAW chip, it will bring the SAW chip down with it).

Once the qubit chip and SAW chips are stuck together, bring the newly formed hybrid system away from the flip-chip mask by moving the sample stage vertically downward. Re-

move the flip-chip mask from the mask aligner. At this point, I find it useful to let the resist "harden" by letting the hybrid system sit at room temperature for five minutes (we haven't systematically investigated whether this improves the reproducibility of the procedure, so this step may not be necessary).

The final step of the procedure is to bake the hybrid system so that the resist (acting as a glue) will harden, ensuring that the system is stuck together. We typically bake the system with the larger chip (the SAW chip) on the "bottom" of the stack at 110° for 5 minutes. Once the hybrid system has been taken off of the hotplate and cooled, it is ready to be mounted into a 3D cavity and tested in the cryostat.

BIBLIOGRAPHY

BIBLIOGRAPHY

[1] C. Kittel. *Introduction to Solid State Physics*. Wiley, 2004.

[2] E. E. Wollman, C. U. Lei, A. J. Weinstein, J. Suh, A. Kronwald, F. Marquardt, A. A. Clerk, and K. C. Schwab. Quantum squeezing of motion in a mechanical resonator. *Science*, 349(6251):952–955, 2015.

[3] Yiwen Chu, Prashanta Kharel, Taekwan Yoon, Luigi Frunzio, Peter T. Rakich, and Robert J. Schoelkopf. Creation and control of multi-phonon Fock states in a bulk acoustic-wave resonator. *Nature*, 563(7733):666–670, Nov 2018.

[4] K. J. Satzinger, Y. P. Zhong, H.-S. Chang, G. A. Peairs, A. Bienfait, Ming-Han Chou, A. Y. Cleland, C. R. Conner, É Dumur, J. Grebel, I. Gutierrez, B. H. November, R. G. Povey, S. J. Whiteley, D. D. Awschalom, D. I. Schuster, and A. N. Cleland. Quantum control of surface acoustic-wave phonons. *Nature*, 563(7733):661–665, Nov 2018.

[5] D.F. Walls and Gerard J. Milburn. *Quantisation of the Electromagnetic Field*, pages 7–27. Springer Berlin Heidelberg, Berlin, Heidelberg, 2008.

[6] Gershon Kurizki, Patrice Bertet, Yuimaru Kubo, Klaus Mølmer, David Petrosyan, Peter Rabl, and Jörg Schmiedmayer. Quantum technologies with hybrid systems. *Proceedings of the National Academy of Sciences*, 112(13):3866–3873, 2015.

[7] A. A. Clerk, K. W. Lehnert, P. Bertet, J. R. Petta, and Y. Nakamura. Hybrid quantum systems with circuit quantum electrodynamics. *Nature Physics*, 16(3):257–267, Mar 2020.

[8] Riccardo Manenti, Anton F Kockum, Andrew Patterson, Tanja Behrle, Joseph Rahamim, Giovanna Tancredi, Franco Nori, and Peter J Leek. Circuit quantum acoustodynamics with surface acoustic waves. *Nature Communications*, 8(1):975, 2017.

[9] Yiwen Chu and Simon Gröblacher. A perspective on hybrid quantum opto- and electromechanical systems. *Applied Physics Letters*, 117(15):150503, 2020.

[10] Alexandre Blais, Ren-Shou Huang, Andreas Wallraff, S. M. Girvin, and R. J. Schoelkopf. Cavity quantum electrodynamics for superconducting electrical circuits: An architecture for quantum computation. *Phys. Rev. A*, 69:062320, Jun 2004.

[11] Alexandre Blais, Arne L. Grimsmo, S. M. Girvin, and Andreas Wallraff. Circuit quantum electrodynamics. *Rev. Mod. Phys.*, 93:025005, May 2021.

[12] A. Wallraff, D. I. Schuster, A. Blais, L. Frunzio, R.-. S. Huang, J. Majer, S. Kumar, S. M. Girvin, and R. J. Schoelkopf. Strong coupling of a single photon to a superconducting qubit using circuit quantum electrodynamics. *Nature*, 431(7005):162–167, Sep 2004.

[13] Jay Gambetta, Alexandre Blais, D. I. Schuster, A. Wallraff, L. Frunzio, J. Majer, M. H. Devoret, S. M. Girvin, and R. J. Schoelkopf. Qubit-photon interactions in a cavity: Measurement-induced dephasing and number splitting. *Phys. Rev. A*, 74:042318, Oct 2006.

[14] Per Delsing, Andrew N Cleland, Martin J A Schuetz, Johannes Knörzer, Géza Giedke, J Ignacio Cirac, Kartik Srinivasan, Marcelo Wu, Krishna Coimbatore Balram, Christopher Bäuerle, Tristan Meunier, Christopher J B Ford, Paulo V Santos, Edgar Cerda-Méndez, Hailin Wang, Hubert J Krenner, Emeline D S Nysten, Matthias Weiß, Geoff R Nash, Laura Thevenard, Catherine Gourdon, Pauline Rovillain, Max Marangolo, Jean-Yves Duquesne, Gerhard Fischerauer, Werner Ruile, Alexander Reiner, Ben Paschke, Dmytro Denysenko, Dirk Volkmer, Achim Wixforth, Henrik Bruus, Martin Wiklund, Julien Reboud, Jonathan M Cooper, YongQing Fu, Manuel S Brugger, Florian Rehfeldt, and Christoph Westerhausen. The 2019 surface acoustic waves roadmap. *Journal of Physics D: Applied Physics*, 52(35):353001, jul 2019.

[15] J. M. Kitzman, J. R. Lane, C. Undershute, P. M. Harrington, N. R. Beysengulov, C. A. Mikolas, K. W. Murch, and J. Pollanen. Phononic bath engineering of a superconducting qubit. *Nature Communications*, 14(1):3910, Jul 2023.

[16] J. M. Kitzman, J. R. Lane, C. Undershute, N. R. Beysengulov, C. A. Mikolas, K. W. Murch, and J. Pollanen. Quantum acoustic Fano interference of surface phonons. *Phys. Rev. A*, 108:L010601, Jul 2023.

[17] J. Pollanen, J. P. Eisenstein, L. N. Pfeiffer, and K. W. West. Charge metastability and hysteresis in the quantum hall regime. *Phys. Rev. B*, 94:245440, Dec 2016.

[18] J. R. Lane, L. Zhang, M. A. Khasawneh, B. N. Zhou, E. A. Henriksen, and J. Pollanen. Flip-chip gate-tunable acoustoelectric effect in graphene. *Journal of Applied Physics*, 124(19):194302, 11 2018.

[19] H. Byeon, K. Nasyedkin, J. R. Lane, N. R. Beysengulov, L. Zhang, R. Loloee, and J. Pollanen. Piezoacoustics for precision control of electrons floating on helium. *Nature Communications*, 12(1):4150, Jul 2021.

[20] Connor T. Hann, Chang-Ling Zou, Yaxing Zhang, Yiwen Chu, Robert J. Schoelkopf, S. M. Girvin, and Liang Jiang. Hardware-efficient quantum random access memory with hybrid quantum acoustic systems. *Phys. Rev. Lett.*, 123:250501, Dec 2019.

[21] Marek Pechal, Patricio Arrangoiz-Arriola, and Amir H Safavi-Naeini. Superconducting circuit quantum computing with nanomechanical resonators as storage. *Quantum Science and Technology*, 4(1):015006, sep 2018.

[22] Atsushi Noguchi, Rekishu Yamazaki, Yutaka Tabuchi, and Yasunobu Nakamura. Qubit-assisted transduction for a detection of surface acoustic waves near the quantum limit. *Phys. Rev. Lett.*, 119:180505, Nov 2017.

[23] Aleksey N. Bolgar, Julia I. Zotova, Daniil D. Kirichenko, Ilia S. Besedin, Aleksander V. Semenov, Rais S. Shaikhaidarov, and Oleg V. Astafiev. Quantum regime of a two-dimensional phonon cavity. *Phys. Rev. Lett.*, 120:223603, May 2018.

[24] Audrey Bienfait, Kevin J Satzinger, YP Zhong, H-S Chang, M-H Chou, Chris R Conner, É Dumur, Joel Grebel, Gregory A Peairs, Rhys G Povey, et al. Phonon-mediated quantum state transfer and remote qubit entanglement. *Science*, 364(6438):368–371, 2019.

[25] É. Dumur, K. J. Satzinger, G. A. Peairs, M.-H. Chou, A. Bienfait, H.-S. Chang, C. R. Conner, J. Grebel, R. G. Povey, Y. P. Zhong, and A. N. Cleland. Quantum communication with itinerant surface acoustic wave phonons. *npj Quantum Information*, 7(1):173, Dec 2021.

[26] H. Qiao, É. Dumur, G. Andersson, H. Yan, M.-H. Chou, J. Grebel, C. R. Conner, Y. J. Joshi, J. M. Miller, R. G. Povey, X. Wu, and A. N. Cleland. Splitting phonons: Building a platform for linear mechanical quantum computing. *Science*, 380(6649):1030–1033, 2023.

[27] R. D. Delaney, M. D. Urmey, S. Mittal, B. M. Brubaker, J. M. Kindem, P. S. Burns, C. A. Regal, and K. W. Lehnert. Superconducting-qubit readout via low-backaction electro-optic transduction. *Nature*, 606(7914):489–493, Jun 2022.

[28] Yiwen Chu, Prashanta Kharel, William H. Renninger, Luke D. Burkhart, Luigi Frunzio, Peter T. Rakich, and Robert J. Schoelkopf. Quantum acoustics with superconducting qubits. *Science*, 358(6360):199–202, 2017.

[29] A. Bienfait, Y. P. Zhong, H.-S. Chang, M.-H. Chou, C. R. Conner, É. Dumur, J. Grebel, G. A. Peairs, R. G. Povey, K. J. Satzinger, and A. N. Cleland. Quantum erasure using entangled surface acoustic phonons. *Phys. Rev. X*, 10:021055, Jun 2020.

[30] É. Dumur, K. J. Satzinger, G. A. Peairs, Ming-Han Chou, A. Bienfait, H.-S. Chang, C. R. Conner, J. Grebel, R. G. Povey, Y. P. Zhong, and A. N. Cleland. Unidirectional distributed acoustic reflection transducers for quantum applications. *Applied Physics Letters*, 114(22):223501, 2019.

[31] Yoshiaki Tamura, Hirotaka Sakuma, Keisei Morita, Masato Suzuki, Yoshinori Yamamoto, Kensaku Shimada, Yuya Honma, Kazuyuki Sohma, Takashi Fujii, and Takemi Hasegawa. The first 0.14-db/km loss optical fiber and its impact on submarine transmission. *J. Lightwave Technol.*, 36(1):44–49, Jan 2018.

[32] Joerg Bochmann, Amit Vainsencher, David D. Awschalom, and Andrew N. Cleland. Nanomechanical coupling between microwave and optical photons. *Nature Physics*, 9(11):712–716, Nov 2013.

[33] Wentao Jiang, Christopher J. Sarabalis, Yanni D. Dahmani, Rishi N. Patel, Felix M. Mayor, Timothy P. McKenna, Raphaël Van Laer, and Amir H. Safavi-Naeini. Efficient bidirectional piezo-optomechanical transduction between microwave and optical frequency. *Nature Communications*, 11(1):1166, Mar 2020.

[34] Mohammad Mirhosseini, Alp Sipahigil, Mahmoud Kalaee, and Oskar Painter. Superconducting qubit to optical photon transduction. *Nature*, 588(7839):599–603, Dec 2020.

[35] Moritz Forsch, Robert Stockill, Andreas Wallucks, Igor Marinković, Claus Gärtner, Richard A. Norte, Frank van Otten, Andrea Fiore, Kartik Srinivasan, and Simon Gröblacher. Microwave-to-optics conversion using a mechanical oscillator in its quantum ground state. *Nature Physics*, 16(1):69–74, Jan 2020.

[36] Robert Stockill, Moritz Forsch, Frederick Hijazi, Grégoire Beaudoin, Konstantinos Pantzas, Isabelle Sagnes, Rémy Braive, and Simon Gröblacher. Ultra-low-noise microwave to optics conversion in gallium phosphide. *Nature Communications*, 13(1):6583, Nov 2022.

[37] R. W. Andrews, R. W. Peterson, T. P. Purdy, K. Cicak, R. W. Simmonds, C. A. Regal, and K. W. Lehnert. Bidirectional and efficient conversion between microwave and optical light. *Nature Physics*, 10(4):321–326, Apr 2014.

[38] A. P. Higginbotham, P. S. Burns, M. D. Urmey, R. W. Peterson, N. S. Kampel, B. M. Brubaker, G. Smith, K. W. Lehnert, and C. A. Regal. Harnessing electro-optic correlations in an efficient mechanical converter. *Nature Physics*, 14(10):1038–1042, Oct 2018.

[39] B. M. Brubaker, J. M. Kindem, M. D. Urmey, S. Mittal, R. D. Delaney, P. S. Burns, M. R. Vissers, K. W. Lehnert, and C. A. Regal. Optomechanical ground-state cooling in a continuous and efficient electro-optic transducer. *Phys. Rev. X*, 12:021062, Jun 2022.

[40] D. I. Schuster, A. A. Houck, J. A. Schreier, A. Wallraff, J. M. Gambetta, A. Blais, L. Frunzio, J. Majer, B. Johnson, M. H. Devoret, S. M. Girvin, and R. J. Schoelkopf. Resolving photon number states in a superconducting circuit. *Nature*, 445(7127):515–518, Feb 2007.

[41] Max Hofheinz, EM Weig, M Ansmann, Radoslaw C Bialczak, Erik Lucero, M Neeley, AD O'connell, H Wang, John M Martinis, and AN Cleland. Generation of Fock states in a superconducting quantum circuit. *Nature*, 454(7202):310–314, 2008.

[42] A. D. O'Connell, M. Hofheinz, M. Ansmann, Radoslaw C. Bialczak, M. Lenander, Erik Lucero, M. Neeley, D. Sank, H. Wang, M. Weides, J. Wenner, John M. Martinis, and A. N. Cleland. Quantum ground state and single-phonon control of a mechanical resonator. *Nature*, 464(7289):697–703, Apr 2010.

[43] Jasper Chan, T. P. Mayer Alegre, Amir H. Safavi-Naeini, Jeff T. Hill, Alex Krause, Simon Gröblacher, Markus Aspelmeyer, and Oskar Painter. Laser cooling of a nanomechanical oscillator into its quantum ground state. *Nature*, 478(7367):89–92, Oct 2011.

[44] J. D. Teufel, T. Donner, Dale Li, J. W. Harlow, M. S. Allman, K. Cicak, A. J. Sirois, J. D. Whittaker, K. W. Lehnert, and R. W. Simmonds. Sideband cooling of micromechanical motion to the quantum ground state. *Nature*, 475(7356):359–363, Jul 2011.

[45] Muhammad Tahir Naseem and Özgür E Müstecaplıoğlu. Ground-state cooling of mechanical resonators by quantum reservoir engineering. *Communications Physics*, 4(1):95, 2021.

[46] D. Cattiaux, I. Golokolenov, S. Kumar, M. Sillanpää, L. Mercier de Lépinay, R. R. Gazizulin, X. Zhou, A. D. Armour, O. Bourgeois, A. Fefferman, and E. Collin. A macroscopic object passively cooled into its quantum ground state of motion beyond single-mode cooling. *Nature Communications*, 12(1):6182, Oct 2021.

[47] E. Verhagen, S. Deléglise, S. Weis, A. Schliesser, and T. J. Kippenberg. Quantum-coherent coupling of a mechanical oscillator to an optical cavity mode. *Nature*, 482(7383):63–67, Feb 2012.

[48] Ralf Riedinger, Sungkun Hong, Richard A Norte, Joshua A Slater, Juying Shang, Alexander G Krause, Vikas Anant, Markus Aspelmeyer, and Simon Gröblacher. Non-

classical correlations between single photons and phonons from a mechanical oscillator. *Nature*, 530(7590):313–316, 2016.

[49] Patricio Arrangoiz-Arriola, E Alex Wollack, Zhaoyou Wang, Marek Pechal, Wentao Jiang, Timothy P McKenna, Jeremy D Witmer, Raphaël Van Laer, and Amir H Safavi-Naeini. Resolving the energy levels of a nanomechanical oscillator. *Nature*, 571(7766):537–540, 2019.

[50] E Alex Wollack, Agnetta Y Cleland, Rachel G Gruenke, Zhaoyou Wang, Patricio Arrangoiz-Arriola, and Amir H Safavi-Naeini. Quantum state preparation and tomography of entangled mechanical resonators. *Nature*, 604(7906):463–467, 2022.

[51] Pieter Kok, W. J. Munro, Kae Nemoto, T. C. Ralph, Jonathan P. Dowling, and G. J. Milburn. Linear optical quantum computing with photonic qubits. *Rev. Mod. Phys.*, 79:135–174, Jan 2007.

[52] Marius Bild, Matteo Fadel, Yu Yang, Uwe von Lüpke, Phillip Martin, Alessandro Bruno, and Yiwen Chu. Schrödinger cat states of a 16-microgram mechanical oscillator. *Science*, 380(6642):274–278, 2023.

[53] E.T. Jaynes and F.W. Cummings. Comparison of quantum and semiclassical radiation theories with application to the beam maser. *Proceedings of the IEEE*, 51(1):89–109, 1963.

[54] Frederick W Cummings. Reminiscing about thesis work with E T Jaynes at Stanford in the 1950s. *Journal of Physics B: Atomic, Molecular and Optical Physics*, 46(22):220202, 2013.

[55] Christopher Chamberland, Kyungjoo Noh, Patricio Arrangoiz-Arriola, Earl T. Campbell, Connor T. Hann, Joseph Iverson, Harald Putterman, Thomas C. Bohdanowicz, Steven T. Flammia, Andrew Keller, Gil Refael, John Preskill, Liang Jiang, Amir H. Safavi-Naeini, Oskar Painter, and Fernando G.S.L. Brandão. Building a fault-tolerant quantum computer using concatenated cat codes. *PRX Quantum*, 3:010329, Feb 2022.

[56] D. I. Schuster, A. Wallraff, A. Blais, L. Frunzio, R.-S. Huang, J. Majer, S. M. Girvin, and R. J. Schoelkopf. ac Stark shift and dephasing of a superconducting qubit strongly coupled to a cavity field. *Phys. Rev. Lett.*, 94:123602, Mar 2005.

[57] Lucas R Sletten, Bradley A Moores, Jeremie J Viennot, and Konrad W Lehnert. Resolving phonon Fock states in a multimode cavity with a double-slit qubit. *Physical Review X*, 9(2):021056, 2019.

[58] Austin G. Fowler, Matteo Mariantoni, John M. Martinis, and Andrew N. Cleland. Surface codes: Towards practical large-scale quantum computation. *Phys. Rev. A*, 86:032324, Sep 2012.

[59] Uwe von Lüpke, Yu Yang, Marius Bild, Laurent Michaud, Matteo Fadel, and Yiwen Chu. Parity measurement in the strong dispersive regime of circuit quantum acoustodynamics. *Nature Physics*, 18(7):794–799, 2022.

[60] U. Fano. Effects of configuration interaction on intensities and phase shifts. *Phys. Rev.*, 124:1866–1878, Dec 1961.

[61] Andrey E. Miroshnichenko, Sergej Flach, and Yuri S. Kivshar. Fano resonances in nanoscale structures. *Rev. Mod. Phys.*, 82:2257–2298, Aug 2010.

[62] P. W. Anderson, B. I. Halperin, and c. M. Varma. Anomalous low-temperature thermal properties of glasses and spin glasses. *The Philosophical Magazine: A Journal of Theoretical Experimental and Applied Physics*, 25(1):1–9, 1972.

[63] William A Phillips. Tunneling states in amorphous solids. *Journal of low temperature physics*, 7:351–360, 1972.

[64] Jürgen Lisenfeld, Clemens Müller, Jared H. Cole, Pavel Bushev, Alexander Lukashenko, Alexander Shnirman, and Alexey V. Ustinov. Rabi spectroscopy of a qubit-fluctuator system. *Phys. Rev. B*, 81:100511, Mar 2010.

[65] T. A. Palomaki, S. K. Dutta, R. M. Lewis, A. J. Przybysz, Hanhee Paik, B. K. Cooper, H. Kwon, J. R. Anderson, C. J. Lobb, F. C. Wellstood, and E. Tiesinga. Multilevel spectroscopy of two-level systems coupled to a dc squid phase qubit. *Phys. Rev. B*, 81:144503, Apr 2010.

[66] Grigorij J. Grabovskij, Torben Peichl, Jürgen Lisenfeld, Georg Weiss, and Alexey V. Ustinov. Strain tuning of individual atomic tunneling systems detected by a superconducting qubit. *Science*, 338(6104):232–234, 2012.

[67] N. R. Beysengulov, J. R. Lane, J. M. Kitzman, K. Nasyedkin, D. G. Rees, and J. Pollanen. Noise performance and thermalization of a single electron transistor using quantum fluids. *Journal of Low Temperature Physics*, 205(3):143–154, Nov 2021.

[68] Agnetta Y. Cleland, E. Alex Wollack, and Amir H. Safavi-Naeini. Studying phonon coherence with a quantum sensor, 2023.

[69] Richard P. Feynman. Simulating Physics with Computers. *International Journal of Theoretical Physics*, 21(6-7):467–488, Jun 1982.

[70] Andreas Trabesinger. Quantum simulation. *Nature Physics*, 8(4):263–263, Apr 2012.

[71] Ehud Altman, Kenneth R. Brown, Giuseppe Carleo, Lincoln D. Carr, Eugene Demler, Cheng Chin, Brian DeMarco, Sophia E. Economou, Mark A. Eriksson, Kai-Mei C. Fu, Markus Greiner, Kaden R.A. Hazzard, Randall G. Hulet, Alicia J. Kollár, Benjamin L. Lev, Mikhail D. Lukin, Ruichao Ma, Xiao Mi, Shashank Misra, Christopher Monroe, Kater Murch, Zaira Nazario, Kang-Kuen Ni, Andrew C. Potter, Pedram Roushan, Mark Saffman, Monika Schleier-Smith, Irfan Siddiqi, Raymond Simmonds, Meenakshi Singh, I.B. Spielman, Kristan Temme, David S. Weiss, Jelena Vučković, Vladan Vuletić, Jun Ye, and Martin Zwierlein. Quantum simulators: Architectures and opportunities. *PRX Quantum*, 2:017003, Feb 2021.

[72] G. Lindblad. On the generators of quantum dynamical semigroups. *Communications in Mathematical Physics*, 48(2):119–130, Jun 1976.

[73] Heinz-Peter Breuer, Elsi-Mari Laine, and Jyrki Piilo. Measure for the degree of non-Markovian behavior of quantum processes in open systems. *Phys. Rev. Lett.*, 103:210401, Nov 2009.

[74] Heinz-Peter Breuer, Elsi-Mari Laine, Jyrki Piilo, and Bassano Vacchini. Colloquium: Non-Markovian dynamics in open quantum systems. *Rev. Mod. Phys.*, 88:021002, Apr 2016.

[75] P. C. Cárdenas, M. Paternostro, and F. L. Semião. Non-Markovian qubit dynamics in a circuit-QED setup. *Phys. Rev. A*, 91:022122, Feb 2015.

[76] Jeffrey Marshall, Lorenzo Campos Venuti, and Paolo Zanardi. Noise suppression via generalized-Markovian processes. *Phys. Rev. A*, 96:052113, Nov 2017.

[77] Evangelos Vlachos, Haimeng Zhang, Vivek Maurya, Jeffrey Marshall, Tameem Albash, and E. M. Levenson-Falk. Master equation emulation and coherence preservation with classical control of a superconducting qubit. *Phys. Rev. A*, 106:062620, Dec 2022.

[78] Lingzhen Guo, Arne Grimsmo, Anton Frisk Kockum, Mikhail Pletyukhov, and Göran Johansson. Giant acoustic atom: A single quantum system with a deterministic time delay. *Phys. Rev. A*, 95:053821, May 2017.

[79] Gustav Andersson, Baladitya Suri, Lingzhen Guo, Thomas Aref, and Per Delsing. Non-exponential decay of a giant artificial atom. *Nature Physics*, 15(11):1123–1127, 2019.

[80] A. A. Clerk, M. H. Devoret, S. M. Girvin, Florian Marquardt, and R. J. Schoelkopf. Introduction to quantum noise, measurement, and amplification. *Rev. Mod. Phys.*, 82:1155–1208, Apr 2010.

[81] A. A. Houck, J. A. Schreier, B. R. Johnson, J. M. Chow, Jens Koch, J. M. Gambetta, D. I. Schuster, L. Frunzio, M. H. Devoret, S. M. Girvin, and R. J. Schoelkopf. Controlling the spontaneous emission of a superconducting transmon qubit. *Phys. Rev. Lett.*, 101:080502, Aug 2008.

[82] P. J. Leek, S. Filipp, P. Maurer, M. Baur, R. Bianchetti, J. M. Fink, M. Göppl, L. Steffen, and A. Wallraff. Using sideband transitions for two-qubit operations in superconducting circuits. *Phys. Rev. B*, 79:180511, May 2009.

[83] K. W. Murch, U. Vool, D. Zhou, S. J. Weber, S. M. Girvin, and I. Siddiqi. Cavity-assisted quantum bath engineering. *Phys. Rev. Lett.*, 109:183602, Oct 2012.

[84] S. Shankar, M. Hatridge, Z. Leghtas, K. M. Sliwa, A. Narla, U. Vool, S. M. Girvin, L. Frunzio, M. Mirrahimi, and M. H. Devoret. Autonomously stabilized entanglement between two superconducting quantum bits. *Nature*, 504(7480):419–422, Dec 2013.

[85] S. Hacohen-Gourgy, V. V. Ramasesh, C. De Grandi, I. Siddiqi, and S. M. Girvin. Cooling and autonomous feedback in a bose-hubbard chain with attractive interactions. *Phys. Rev. Lett.*, 115:240501, Dec 2015.

[86] M. E. Kimchi-Schwartz, L. Martin, E. Flurin, C. Aron, M. Kulkarni, H. E. Tureci, and I. Siddiqi. Stabilizing entanglement via symmetry-selective bath engineering in superconducting qubits. *Phys. Rev. Lett.*, 116:240503, Jun 2016.

[87] Yanbing Liu and Andrew A. Houck. Quantum electrodynamics near a photonic bandgap. *Nature Physics*, 13(1):48–52, Jan 2017.

[88] Yao Lu, S. Chakram, N. Leung, N. Earnest, R. K. Naik, Ziwen Huang, Peter Groszkowski, Eliot Kapit, Jens Koch, and David I. Schuster. Universal stabilization of a parametrically coupled qubit. *Phys. Rev. Lett.*, 119:150502, Oct 2017.

[89] P. M. Harrington, M. Naghiloo, D. Tan, and K. W. Murch. Bath engineering of a fluorescing artificial atom with a photonic crystal. *Phys. Rev. A*, 99:052126, May 2019.

[90] Patrick M. Harrington, Erich J. Mueller, and Kater W. Murch. Engineered dissipation for quantum information science. *Nature Reviews Physics*, 4(10):660–671, Oct 2022.

[91] M. Naghiloo, M. Abbasi, Yogesh N. Joglekar, and K. W. Murch. Quantum state tomography across the exceptional point in a single dissipative qubit. *Nature Physics*, 15(12):1232–1236, Dec 2019.

[92] John Gunderson, Jacob Muldoon, Kater W. Murch, and Yogesh N. Joglekar. Floquet exceptional contours in lindblad dynamics with time-periodic drive and dissipation. *Phys. Rev. A*, 103:023718, Feb 2021.

[93] Maryam Abbasi, Weijian Chen, Mahdi Naghiloo, Yogesh N. Joglekar, and Kater W. Murch. Topological quantum state control through exceptional-point proximity. *Phys. Rev. Lett.*, 128:160401, Apr 2022.

[94] Weijian Chen, Maryam Abbasi, Byung Ha, Serra Erdamar, Yogesh N. Joglekar, and Kater W. Murch. Decoherence-induced exceptional points in a dissipative superconducting qubit. *Phys. Rev. Lett.*, 128:110402, Mar 2022.

[95] Anton Frisk Kockum, Per Delsing, and Göran Johansson. Designing frequency-dependent relaxation rates and lamb shifts for a giant artificial atom. *Phys. Rev. A*, 90:013837, Jul 2014.

[96] Carl M. Bender and Stefan Boettcher. Real spectra in non-Hermitian Hamiltonians having $\mathcal{PT}$ symmetry. *Phys. Rev. Lett.*, 80:5243–5246, Jun 1998.

[97] S.E. Rasmussen, K.S. Christensen, S.P. Pedersen, L.B. Kristensen, T. Bækkegaard, N.J.S. Loft, and N.T. Zinner. Superconducting circuit companion—an introduction with worked examples. *PRX Quantum*, 2:040204, Dec 2021.

[98] B.D. Josephson. Possible new effects in superconductive tunnelling. *Physics Letters*, 1(7):251–253, 1962.

[99] B. D. Josephson. The discovery of tunnelling supercurrents. *Rev. Mod. Phys.*, 46:251–254, Apr 1974.

[100] M. Tinkham. *Introduction to Superconductivity*. Dover Books on Physics Series. Dover Publications, 2004.

[101] Yuriy Makhlin, Gerd Schön, and Alexander Shnirman. Quantum-state engineering with Josephson-junction devices. *Rev. Mod. Phys.*, 73:357–400, May 2001.

[102] Y. Nakamura, Yu. A. Pashkin, and J. S. Tsai. Coherent control of macroscopic quantum states in a single-cooper-pair box. *Nature*, 398(6730):786–788, Apr 1999.

[103] Jens Koch, Terri M. Yu, Jay Gambetta, A. A. Houck, D. I. Schuster, J. Majer, Alexandre Blais, M. H. Devoret, S. M. Girvin, and R. J. Schoelkopf. Charge-insensitive qubit design derived from the Cooper pair box. *Phys. Rev. A*, 76:042319, Oct 2007.

[104] Frank Arute, Kunal Arya, Ryan Babbush, Dave Bacon, Joseph C. Bardin, Rami Barends, Rupak Biswas, Sergio Boixo, Fernando G. S. L. Brandao, David A. Buell, Brian Burkett, Yu Chen, Zijun Chen, Ben Chiaro, Roberto Collins, William Courtney, Andrew Dunsworth, Edward Farhi, Brooks Foxen, Austin Fowler, Craig Gidney, Marissa Giustina, Rob Graff, Keith Guerin, Steve Habegger, Matthew P. Harrigan, Michael J. Hartmann, Alan Ho, Markus Hoffmann, Trent Huang, Travis S. Humble, Sergei V. Isakov, Evan Jeffrey, Zhang Jiang, Dvir Kafri, Kostyantyn Kechedzhi, Julian Kelly, Paul V. Klimov, Sergey Knysh, Alexander Korotkov, Fedor Kostritsa, David Landhuis, Mike Lindmark, Erik Lucero, Dmitry Lyakh, Salvatore Mandrà, Jarrod R. McClean, Matthew McEwen, Anthony Megrant, Xiao Mi, Kristel Michielsen, Masoud Mohseni, Josh Mutus, Ofer Naaman, Matthew Neeley, Charles Neill, Murphy Yuezhen Niu, Eric Ostby, Andre Petukhov, John C. Platt, Chris Quintana, Eleanor G. Rieffel, Pedram Roushan, Nicholas C. Rubin, Daniel Sank, Kevin J. Satzinger, Vadim Smelyanskiy, Kevin J. Sung, Matthew D. Trevithick, Amit Vainsencher, Benjamin Villalonga, Theodore White, Z. Jamie Yao, Ping Yeh, Adam Zalcman, Hartmut Neven, and John M. Martinis. Quantum supremacy using a programmable superconducting processor. *Nature*, 574(7779):505–510, Oct 2019.

[105] Google AI Quantum, Collaborators*†, Frank Arute, Kunal Arya, Ryan Babbush, Dave Bacon, Joseph C. Bardin, Rami Barends, Sergio Boixo, Michael Broughton, Bob B. Buckley, David A. Buell, Brian Burkett, Nicholas Bushnell, Yu Chen, Zijun Chen, Benjamin Chiaro, Roberto Collins, William Courtney, Sean Demura, Andrew Dunsworth, Edward Farhi, Austin Fowler, Brooks Foxen, Craig Gidney, Marissa Giustina, Rob Graff, Steve Habegger, Matthew P. Harrigan, Alan Ho, Sabrina Hong, Trent Huang, William J. Huggins, Lev Ioffe, Sergei V. Isakov, Evan Jeffrey, Zhang Jiang, Cody Jones, Dvir Kafri, Kostyantyn Kechedzhi, Julian Kelly, Seon Kim, Paul V. Klimov, Alexander Korotkov, Fedor Kostritsa, David Landhuis, Pavel Laptev, Mike Lindmark, Erik Lucero, Orion Martin, John M. Martinis, Jarrod R. McClean, Matt McEwen, Anthony Megrant, Xiao Mi, Masoud Mohseni, Wojciech Mruczkiewicz, Josh Mutus, Ofer Naaman, Matthew Neeley, Charles Neill, Hartmut Neven, Murphy Yuezhen Niu, Thomas E. O'Brien, Eric Ostby, Andre Petukhov, Harald Putterman, Chris Quintana, Pedram Roushan, Nicholas C. Rubin, Daniel Sank, Kevin J. Satzinger, Vadim Smelyanskiy, Doug Strain, Kevin J. Sung, Marco Szalay, Tyler Y. Takeshita, Amit Vainsencher, Theodore White, Nathan Wiebe, Z. Jamie Yao, Ping Yeh, and Adam Zalcman. Hartree-fock on a superconducting qubit quantum computer. *Science*, 369(6507):1084–1089, 2020.

[106] K. J. Satzinger, Y.-J Liu, A. Smith, C. Knapp, M. Newman, C. Jones, Z. Chen, C. Quintana, X. Mi, A. Dunsworth, C. Gidney, I. Aleiner, F. Arute, K. Arya, J. Atalaya, R. Babbush, J. C. Bardin, R. Barends, J. Basso, A. Bengtsson, A. Bilmes, M. Broughton, B. B. Buckley, D. A. Buell, B. Burkett, N. Bushnell, B. Chiaro, R. Collins, W. Courtney, S. Demura, A. R. Derk, D. Eppens, C. Erickson, L. Faoro, E. Farhi, A. G. Fowler, B. Foxen, M. Giustina, A. Greene, J. A. Gross, M. P. Harrigan, S. D. Harrington, J. Hilton, S. Hong, T. Huang, W. J. Huggins, L. B. Ioffe, S. V. Isakov, E. Jeffrey, Z. Jiang, D. Kafri, K. Kechedzhi, T. Khattar, S. Kim, P. V. Klimov, A. N. Korotkov, F. Kostritsa, D. Landhuis, P. Laptev, A. Locharla, E. Lucero, O. Martin, J. R. McClean, M. McEwen, K. C. Miao, M. Mohseni, S. Montazeri, W. Mruczkiewicz, J. Mutus, O. Naaman, M. Neeley, C. Neill, M. Y. Niu, T. E. O'Brien, A. Opremcak, B. Pató, A. Petukhov, N. C. Rubin, D. Sank, V. Shvarts, D. Strain, M. Szalay, B. Villalonga, T. C. White, Z. Yao, P. Yeh, J. Yoo, A. Zalcman, H. Neven, S. Boixo, A. Megrant, Y. Chen, J. Kelly, V. Smelyanskiy, A. Kitaev, M. Knap, F. Pollmann, and P. Roushan. Realizing topologically ordered states on a quantum processor. *Science*, 374(6572):1237–1241, 2021.

[107] Matthew P. Harrigan, Kevin J. Sung, Matthew Neeley, Kevin J. Satzinger, Frank Arute, Kunal Arya, Juan Atalaya, Joseph C. Bardin, Rami Barends, Sergio Boixo, Michael Broughton, Bob B. Buckley, David A. Buell, Brian Burkett, Nicholas Bushnell, Yu Chen, Zijun Chen, Ben Chiaro, Roberto Collins, William Courtney, Sean Demura, Andrew Dunsworth, Daniel Eppens, Austin Fowler, Brooks Foxen, Craig Gidney, Marissa Giustina, Rob Graff, Steve Habegger, Alan Ho, Sabrina Hong, Trent Huang, L. B. Ioffe, Sergei V. Isakov, Evan Jeffrey, Zhang Jiang, Cody Jones, Dvir Kafri, Kostyantyn Kechedzhi, Julian Kelly, Seon Kim, Paul V. Klimov, Alexander N. Korotkov, Fedor Kostritsa, David Landhuis, Pavel Laptev, Mike Lindmark, Martin Leib, Orion Martin, John M. Martinis, Jarrod R. McClean, Matt McEwen, Anthony Megrant, Xiao Mi, Masoud Mohseni, Wojciech Mruczkiewicz, Josh Mutus, Ofer Naaman, Charles Neill, Florian Neukart, Murphy Yuezhen Niu, Thomas E. O'Brien, Bryan O'Gorman, Eric Ostby, Andre Petukhov, Harald Putterman, Chris Quintana, Pedram Roushan, Nicholas C. Rubin, Daniel Sank, Andrea Skolik, Vadim Smelyanskiy, Doug Strain, Michael Streif, Marco Szalay, Amit Vainsencher, Theodore White, Z. Jamie Yao, Ping Yeh, Adam Zalcman, Leo Zhou, Hartmut Neven, Dave Bacon, Erik Lucero, Edward Farhi, and Ryan Babbush. Quantum approximate optimization of non-planar graph problems on a planar superconducting processor. *Nature Physics*, 17(3):332–336, Mar 2021.

[108] Youngseok Kim, Andrew Eddins, Sajant Anand, Ken Xuan Wei, Ewout van den Berg, Sami Rosenblatt, Hasan Nayfeh, Yantao Wu, Michael Zaletel, Kristan Temme, and Abhinav Kandala. Evidence for the utility of quantum computing before fault tolerance. *Nature*, 618(7965):500–505, Jun 2023.

[109] M. H. Devoret. *Quantum Fluctuations in Electrical Circuits*, chapter 10. Elsevier Science, 1997.

[110] W. C. Smith, A. Kou, X. Xiao, U. Vool, and M. H. Devoret. Superconducting circuit protected by two-cooper-pair tunneling. *npj Quantum Information*, 6(1):8, Jan 2020.

[111] W. C. Smith, M. Villiers, A. Marquet, J. Palomo, M. R. Delbecq, T. Kontos, P. Campagne-Ibarcq, B. Douçot, and Z. Leghtas. Magnifying quantum phase fluctuations with cooper-pair pairing. *Phys. Rev. X*, 12:021002, Apr 2022.

[112] H J Kimble. Strong interactions of single atoms and photons in cavity QED. *Physica Scripta*, 1998(T76):127, Jan 1998.

[113] David Issac Schuster. *Circuit Quantum Electrodynamics*. PhD thesis, Yale University, 2007.

[114] Daniel Thomas Sank. *Fast, Accurate State Measurement in Superconducting Qubits*. PhD thesis, University of California Santa Barbara, 2014.

[115] Vinay Ramasesh. *Quantum Simulation with Superconducting Circuits*. PhD thesis, University of California, Berkeley, 2019.

[116] Akash V Dixit. *Searching for Dark Matter with Superconducting Qubits*. PhD thesis, The University of Chicago, 2021.

[117] Hanhee Paik, D. I. Schuster, Lev S. Bishop, G. Kirchmair, G. Catelani, A. P. Sears, B. R. Johnson, M. J. Reagor, L. Frunzio, L. I. Glazman, S. M. Girvin, M. H. Devoret, and R. J. Schoelkopf. Observation of high coherence in Josephson junction qubits measured in a three-dimensional circuit QED architecture. *Phys. Rev. Lett.*, 107:240501, Dec 2011.

[118] David J. Griffiths. *Introduction to Electrodynamics*. Cambridge University Press, 4 edition, 2017.

[119] A. P. Sears, A. Petrenko, G. Catelani, L. Sun, Hanhee Paik, G. Kirchmair, L. Frunzio, L. I. Glazman, S. M. Girvin, and R. J. Schoelkopf. Photon shot noise dephasing in the strong-dispersive limit of circuit QED. *Phys. Rev. B*, 86:180504, Nov 2012.

[120] Simon E. Nigg, Hanhee Paik, Brian Vlastakis, Gerhard Kirchmair, S. Shankar, Luigi Frunzio, M. H. Devoret, R. J. Schoelkopf, and S. M. Girvin. Black-box superconducting circuit quantization. *Phys. Rev. Lett.*, 108:240502, Jun 2012.

[121] Roy J. Glauber. Coherent and incoherent states of the radiation field. *Phys. Rev.*, 131:2766–2788, Sep 1963.

[122] Justin R Lane. *Integrating Superconducting Qubits with Quantum Fluids and Surface Acoustic Wave Devices*. PhD thesis, Michigan State University, 2021.

[123] Vladimir E. Manucharyan, Jens Koch, Leonid I. Glazman, and Michel H. Devoret. Fluxonium: Single Cooper-pair circuit free of charge offsets. *Science*, 326(5949):113–116, 2009.

[124] Helin Zhang, Srivatsan Chakram, Tanay Roy, Nathan Earnest, Yao Lu, Ziwen Huang, D. K. Weiss, Jens Koch, and David I. Schuster. Universal fast-flux control of a coherent, low-frequency qubit. *Phys. Rev. X*, 11:011010, Jan 2021.

[125] Haonan Xiong, Quentin Ficheux, Aaron Somoroff, Long B. Nguyen, Ebru Dogan, Dario Rosenstock, Chen Wang, Konstantin N. Nesterov, Maxim G. Vavilov, and Vladimir E. Manucharyan. Arbitrary controlled-phase gate on fluxonium qubits using differential ac Stark shifts. *Phys. Rev. Res.*, 4:023040, Apr 2022.

[126] Aaron Somoroff, Quentin Ficheux, Raymond A. Mencia, Haonan Xiong, Roman Kuzmin, and Vladimir E. Manucharyan. Millisecond coherence in a superconducting qubit. *Phys. Rev. Lett.*, 130:267001, Jun 2023.

[127] X. Y. Jin, A. Kamal, A. P. Sears, T. Gudmundsen, D. Hover, J. Miloshi, R. Slattery, F. Yan, J. Yoder, T. P. Orlando, S. Gustavsson, and W. D. Oliver. Thermal and residual excited-state population in a 3D transmon qubit. *Phys. Rev. Lett.*, 114:240501, Jun 2015.

[128] K. Geerlings, Z. Leghtas, I. M. Pop, S. Shankar, L. Frunzio, R. J. Schoelkopf, M. Mirrahimi, and M. H. Devoret. Demonstrating a driven reset protocol for a superconducting qubit. *Phys. Rev. Lett.*, 110:120501, Mar 2013.

[129] J. R. Lane, D. Tan, N. R. Beysengulov, K. Nasyedkin, E. Brook, L. Zhang, T. Stefanski, H. Byeon, K. W. Murch, and J. Pollanen. Integrating superfluids with superconducting qubit systems. *Phys. Rev. A*, 101:012336, Jan 2020.

[130] J. M. Kitzman, J. R. Lane, T. Stefanski, N. R. Beysengulov, D. Tan, K. W. Murch, and J. Pollanen. Vantablack shielding of superconducting qubit systems. *Journal of Low Temperature Physics*, 208(5):467–474, Sep 2022.

[131] Fei Yan, Dan Campbell, Philip Krantz, Morten Kjaergaard, David Kim, Jonilyn L. Yoder, David Hover, Adam Sears, Andrew J. Kerman, Terry P. Orlando, Simon Gustavsson, and William D. Oliver. Distinguishing coherent and thermal photon noise in a circuit quantum electrodynamical system. *Phys. Rev. Lett.*, 120:260504, Jun 2018.

[132] K. Serniak, S. Diamond, M. Hays, V. Fatemi, S. Shankar, L. Frunzio, R.J. Schoelkopf, and M.H. Devoret. Direct dispersive monitoring of charge parity in offset-charge-sensitive transmons. *Phys. Rev. Applied*, 12:014052, Jul 2019.

[133] D F Santavicca and D E Prober. Impedance-matched low-pass stripline filters. *Measurement Science and Technology*, 19(8):087001, jun 2008.

[134] Benjamin J. Chapman, Eric I. Rosenthal, Joseph Kerckhoff, Bradley A. Moores, Leila R. Vale, J. A. B. Mates, Gene C. Hilton, Kevin Lalumière, Alexandre Blais, and K. W. Lehnert. Widely tunable on-chip microwave circulator for superconducting quantum circuits. *Phys. Rev. X*, 7:041043, Nov 2017.

[135] Yi Zhuang, Chandrashekhar Gaikwad, Daria Kowsari, Kater Murch, and Aravind Nagulu. Superconducting non-reciprocity based on time-modulated coupled-resonator systems. *arXiv preprint arXiv:2307.01853*, 2023.

[136] M. A. Castellanos-Beltran, K. D. Irwin, G. C. Hilton, L. R. Vale, and K. W. Lehnert. Amplification and squeezing of quantum noise with a tunable josephson metamaterial. *Nature Physics*, 4(12):929–931, Dec 2008.

[137] T. Yamamoto, K. Inomata, M. Watanabe, K. Matsuba, T. Miyazaki, W. D. Oliver, Y. Nakamura, and J. S. Tsai. Flux-driven Josephson parametric amplifier. *Applied Physics Letters*, 93(4):042510, 07 2008.

[138] N. Roch, E. Flurin, F. Nguyen, P. Morfin, P. Campagne-Ibarcq, M. H. Devoret, and B. Huard. Widely tunable, nondegenerate three-wave mixing microwave device operating near the quantum limit. *Phys. Rev. Lett.*, 108:147701, Apr 2012.

[139] C. Macklin, K. O'Brien, D. Hover, M. E. Schwartz, V. Bolkhovsky, X. Zhang, W. D. Oliver, and I. Siddiqi. A near–quantum-limited josephson traveling-wave parametric amplifier. *Science*, 350(6258):307–310, 2015.

[140] A. B. Zorin. Josephson traveling-wave parametric amplifier with three-wave mixing. *Phys. Rev. Appl.*, 6:034006, Sep 2016.

[141] M. D. Reed, L. DiCarlo, B. R. Johnson, L. Sun, D. I. Schuster, L. Frunzio, and R. J. Schoelkopf. High-fidelity readout in circuit quantum electrodynamics using the Jaynes-Cummings nonlinearity. *Phys. Rev. Lett.*, 105:173601, Oct 2010.

[142] Lev S. Bishop, Eran Ginossar, and S. M. Girvin. Response of the strongly driven Jaynes-Cummings oscillator. *Phys. Rev. Lett.*, 105:100505, Sep 2010.

[143] Maxime Boissonneault, J. M. Gambetta, and Alexandre Blais. Improved superconducting qubit readout by qubit-induced nonlinearities. *Phys. Rev. Lett.*, 105:100504, Sep 2010.

[144] D.J. Griffiths and P.D.J. Griffiths. *Introduction to Quantum Mechanics*. Pearson international edition. Pearson Prentice Hall, 2005.

[145] E. Fukushima. *Experimental Pulse NMR: A Nuts and Bolts Approach*. CRC Press, 2018.

[146] P. Krantz, M. Kjaergaard, F. Yan, T. P. Orlando, S. Gustavsson, and W. D. Oliver. A quantum engineer's guide to superconducting qubits. *Applied Physics Reviews*, 6(2):021318, 06 2019.

[147] Leandro Stefanazzi, Kenneth Treptow, Neal Wilcer, Chris Stoughton, Collin Bradford, Sho Uemura, Silvia Zorzetti, Salvatore Montella, Gustavo Cancelo, Sara Sussman, Andrew Houck, Shefali Saxena, Horacio Arnaldi, Ankur Agrawal, Helin Zhang, Chunyang Ding, and David I. Schuster. The QICK (Quantum Instrumentation Control Kit): Readout and control for qubits and detectors. *Review of Scientific Instruments*, 93(4):044709, 04 2022.

[148] Mikael Kervinen, Ilkka Rissanen, and Mika Sillanpää. Interfacing planar superconducting qubits with high overtone bulk acoustic phonons. *Phys. Rev. B*, 97:205443, May 2018.

[149] Mikael Kervinen, Jhon E. Ramírez-Muñoz, Alpo Välimaa, and Mika A. Sillanpää. Landau-zener-stückelberg interference in a multimode electromechanical system in the quantum regime. *Phys. Rev. Lett.*, 123:240401, Dec 2019.

[150] M.-H. Chou, É. Dumur, Y. P. Zhong, G. A. Peairs, A. Bienfait, H.-S. Chang, C. R. Conner, J. Grebel, R. G. Povey, K. J. Satzinger, and A. N. Cleland. Measurements of a quantum bulk acoustic resonator using a superconducting qubit. *Applied Physics Letters*, 117(25), 12 2020. 254001.

[151] Uwe von Lüpke, Ines C. Rodrigues, Yu Yang, Matteo Fadel, and Yiwen Chu. Engineering phonon-phonon interactions in multimode circuit quantum acousto-dynamics, 2023.

[152] Hugo Banderier, Maxwell Drimmer, and Yiwen Chu. Unified simulation methods for quantum acoustic devices, 2023.

[153] Martin V. Gustafsson, Thomas Aref, Anton Frisk Kockum, Maria K. Ekström, Göran Johansson, and Per Delsing. Propagating phonons coupled to an artificial atom. *Science*, 346(6206):207–211, 2014.

[154] Bradley A. Moores, Lucas R. Sletten, Jeremie J. Viennot, and K. W. Lehnert. Cavity quantum acoustic device in the multimode strong coupling regime. *Phys. Rev. Lett.*, 120:227701, May 2018.

[155] Aleksey N. Bolgar, Daniil D. Kirichenko, Rais. S. Shaikhaidarov, Shtefan V. Sanduleanu, Alexander V. Semenov, Aleksey Yu. Dmitriev, and Oleg V. Astafiev. A phononic crystal coupled to a transmission line via an artificial atom. *Communications Physics*, 3(1):207, Nov 2020.

[156] Jeremy D. Witmer, Joseph A. Valery, Patricio Arrangoiz-Arriola, Christopher J. Sarabalis, Jeff T. Hill, and Amir H. Safavi-Naeini. High-q photonic resonators and electro-optic coupling using silicon-on-lithium-niobate. *Scientific Reports*, 7(1):46313, Apr 2017.

[157] Patricio Arrangoiz-Arriola, E. Alex Wollack, Marek Pechal, Jeremy D. Witmer, Jeff T. Hill, and Amir H. Safavi-Naeini. Coupling a superconducting quantum circuit to a phononic crystal defect cavity. *Phys. Rev. X*, 8:031007, Jul 2018.

[158] Nathan R. A. Lee, Yudan Guo, Agnetta Y. Cleland, E. Alex Wollack, Rachel G. Gruenke, Takuma Makihara, Zhaoyou Wang, Taha Rajabzadeh, Wentao Jiang, Felix M. Mayor, Patricio Arrangoiz-Arriola, Christopher J. Sarabalis, and Amir H. Safavi-Naeini. Strong dispersive coupling between a mechanical resonator and a fluxonium superconducting qubit, 2023.

[159] D. P. Morgan. *Surface Acoustic Wave Devices*. Elsevier Ltd., 2nd edition, 2005.

[160] Kevin Joseph Satzinger. *Quantum control of surface acoustic wave phonons*. PhD thesis, University of California Santa Barbara, 2018.

[161] Lucas Sletten. *Quantum Acoustics with Multimode Surface Acoustic Wave Cavities*. PhD thesis, University of Colorado, 2021.

[162] Daniel Royer and Eugene Dieulesaint. *Elastic waves in solids I: Free and guided propagation*. Springer Science & Business Media, 1999.

[163] Andrew N. Cleland. *Elasticity Relations*, pages 175–190. Springer Berlin Heidelberg, Berlin, Heidelberg, 2003.

[164] L.D. Landau, E.M. Lifshitz, A.M. Kosevich, and L.P. Pitaevskii. *Theory of Elasticity: Volume 7*. Course of theoretical physics. Elsevier Science, 1986.

[165] Lord Rayleigh. On waves propagated along the plane surface of an elastic solid. *Proceedings of the London Mathematical Society*, s1-17(1):4–11, 1885.

[166] Andrew N. Cleland. *Properties of the Phonon Gas*, pages 87–144. Springer Berlin Heidelberg, Berlin, Heidelberg, 2003.

[167] C. Campbell. *Surface Acoustic Wave Devices for Mobile and Wireless Communications, Four-Volume Set*. Applications of Modern Acoustics. Elsevier Science, 1998.

[168] D.M. Pozar. *Microwave Engineering*. Wiley, 2005.

[169] Thomas Aref, Per Delsing, Maria K. Ekström, Anton Frisk Kockum, Martin V. Gustafsson, Göran Johansson, Peter J. Leek, Einar Magnusson, and Riccardo Manenti. *Quantum Acoustics with Surface Acoustic Waves*, pages 217–244. Springer International Publishing, Cham, 2016.

[170] C. Dunnrowicz, F. Sandy, and T. Parker. Reflection of surfaces waves from periodic discontinuities. In *1976 Ultrasonics Symposium*, pages 386–390, 1976.

[171] Heinz-Peter Breuer and Francesco Petruccione. *The Theory of Open Quantum Systems*. Oxford University Press, 01 2007.

[172] Lev S. Bishop. *Circuit Quantum Electrodynamics*. PhD thesis, Yale University, 2010.

[173] Patrick Michael Harrington. *Measurement, Dissipation, and Quantum Control with Superconducting Circuits*. PhD thesis, Washington University in St. Louis, 2020.

[174] Daniel Paz. *Critical Properties of the Driven-Dissipative Ising Model*. PhD thesis, Michigan State University, 2023.

[175] Carlos Alexandre Brasil, Felipe Fernandes Fanchini, and Reginaldo de Jesus Napolitano. A simple derivation of the Lindblad equation. *Revista Brasileira de Ensino de Física*, 35(1):01–09, 2013.

[176] Alto Osada, Rekishu Yamazaki, and Atsushi Noguchi. *Wavefunction and Notations in Quantum Mechanics*, pages 25–72. Springer Nature Singapore, Singapore, 2022.

[177] Max Born. Quantenmechanik der stoßvorgänge. *Zeitschrift für Physik*, 38(11):803–827, Nov 1926.

[178] Daniel Manzano. A short introduction to the Lindblad master equation. *AIP Advances*, 10(2), 02 2020. 025106.

[179] J.R. Johansson, P.D. Nation, and Franco Nori. Qutip 2: A python framework for the dynamics of open quantum systems. *Computer Physics Communications*, 184(4):1234–1240, 2013.

[180] J. I. Cirac and P. Zoller. Quantum computations with cold trapped ions. *Phys. Rev. Lett.*, 74:4091–4094, May 1995.

[181] J. I. Cirac and P. Zoller. A scalable quantum computer with ions in an array of microtraps. *Nature*, 404(6778):579–581, Apr 2000.

[182] Shi-Liang Zhu, C. Monroe, and L.-M. Duan. Trapped ion quantum computation with transverse phonon modes. *Phys. Rev. Lett.*, 97:050505, Aug 2006.

[183] C. V. Shank. Physics of dye lasers. *Rev. Mod. Phys.*, 47:649–657, Jul 1975.

[184] R. Hanson, O. Gywat, and D. D. Awschalom. Room-temperature manipulation and decoherence of a single spin in diamond. *Phys. Rev. B*, 74:161203, Oct 2006.

[185] William F. Koehl, Bob B. Buckley, F. Joseph Heremans, Greg Calusine, and David D. Awschalom. Room temperature coherent control of defect spin qubits in silicon carbide. *Nature*, 479(7371):84–87, Nov 2011.

[186] C. D. Wilen, S. Abdullah, N. A. Kurinsky, C. Stanford, L. Cardani, G. D'Imperio, C. Tomei, L. Faoro, L. B. Ioffe, C. H. Liu, A. Opremcak, B. G. Christensen, J. L. DuBois, and R. McDermott. Correlated charge noise and relaxation errors in superconducting qubits. *Nature*, 594(7863):369–373, Jun 2021.

[187] Matt McEwen, Lara Faoro, Kunal Arya, Andrew Dunsworth, Trent Huang, Seon Kim, Brian Burkett, Austin Fowler, Frank Arute, Joseph C. Bardin, Andreas Bengtsson, Alexander Bilmes, Bob B. Buckley, Nicholas Bushnell, Zijun Chen, Roberto Collins, Sean Demura, Alan R. Derk, Catherine Erickson, Marissa Giustina, Sean D. Harrington, Sabrina Hong, Evan Jeffrey, Julian Kelly, Paul V. Klimov, Fedor Kostritsa, Pavel Laptev, Aditya Locharla, Xiao Mi, Kevin C. Miao, Shirin Montazeri, Josh Mutus, Ofer Naaman, Matthew Neeley, Charles Neill, Alex Opremcak, Chris Quintana, Nicholas Redd, Pedram Roushan, Daniel Sank, Kevin J. Satzinger, Vladimir Shvarts, Theodore

White, Z. Jamie Yao, Ping Yeh, Juhwan Yoo, Yu Chen, Vadim Smelyanskiy, John M. Martinis, Hartmut Neven, Anthony Megrant, Lev Ioffe, and Rami Barends. Resolving catastrophic error bursts from cosmic rays in large arrays of superconducting qubits. *Nature Physics*, 18(1):107–111, Jan 2022.

[188] Arno Bargerbos, Lukas Johannes Splitthoff, Marta Pita-Vidal, Jaap J. Wesdorp, Yu Liu, Peter Krogstrup, Leo P. Kouwenhoven, Christian Kraglund Andersen, and Lukas Grünhaupt. Mitigation of quasiparticle loss in superconducting qubits by phonon scattering. *Phys. Rev. Appl.*, 19:024014, Feb 2023.

[189] Gustav Andersson, Maria K. Ekström, and Per Delsing. Electromagnetically induced acoustic transparency with a superconducting circuit. *Phys. Rev. Lett.*, 124:240402, Jun 2020.

[190] M. D. LaHaye, J. Suh, P. M. Echternach, K. C. Schwab, and M. L. Roukes. Nanomechanical measurements of a superconducting qubit. *Nature*, 459(7249):960–964, Jun 2009.

[191] J.-M. Pirkkalainen, S. U. Cho, Jian Li, G. S. Paraoanu, P. J. Hakonen, and M. A. Sillanpää. Hybrid circuit cavity quantum electrodynamics with a micromechanical resonator. *Nature*, 494(7436):211–215, Feb 2013.

[192] A. P. Reed, K. H. Mayer, J. D. Teufel, L. D. Burkhart, W. Pfaff, M. Reagor, L. Sletten, X. Ma, R. J. Schoelkopf, E. Knill, and K. W. Lehnert. Faithful conversion of propagating quantum information to mechanical motion. *Nature Physics*, 13(12):1163–1167, Dec 2017.

[193] B. R. Mollow. Power spectrum of light scattered by two-level systems. *Phys. Rev.*, 188:1969–1975, Dec 1969.

[194] M. Baur, S. Filipp, R. Bianchetti, J. M. Fink, M. Göppl, L. Steffen, P. J. Leek, A. Blais, and A. Wallraff. Measurement of Autler-Townes and Mollow transitions in a strongly driven superconducting qubit. *Phys. Rev. Lett.*, 102:243602, Jun 2009.

[195] D. M. Toyli, A. W. Eddins, S. Boutin, S. Puri, D. Hover, V. Bolkhovsky, W. D. Oliver, A. Blais, and I. Siddiqi. Resonance fluorescence from an artificial atom in squeezed vacuum. *Phys. Rev. X*, 6:031004, Jul 2016.

[196] Joe Kitzman, Justin Lane, Camryn Undershute, Patrick Harrington, Niyaz Beysengulov, Camille Mikolas, Kater Murch, and Johannes Pollanen. Phononic bath engineering of a superconducting qubit, https://doi.org/10.5281/zenodo.8043749, June 2023.

[197] Clemens Müller, Jared H Cole, and Jürgen Lisenfeld. Towards understanding two-level-systems in amorphous solids: insights from quantum circuits. *Reports on Progress in Physics*, 82(12):124501, Oct 2019.

[198] Ettore Majorana. Sulla formazione dello ione molecolare di He. *Nuovo Cimento*, 8:22, 1931.

[199] Christian Ott, Andreas Kaldun, Philipp Raith, Kristina Meyer, Martin Laux, Jörg Evers, Christoph H. Keitel, Chris H. Greene, and Thomas Pfeifer. Lorentz meets fano in spectral line shapes: A universal phase and its laser control. *Science*, 340(6133):716–720, 2013.

[200] Y.-N. Lv, A.-W. Liu, Y. Tan, C.-L. Hu, T.-P. Hua, X.-B. Zou, Y. R. Sun, C.-L. Zou, G.-C. Guo, and S.-M. Hu. Fano-like resonance due to interference with distant transitions. *Phys. Rev. Lett.*, 129:163201, Oct 2022.

[201] Michael I. Tribelsky, Sergej Flach, Andrey E. Miroshnichenko, Andrey V. Gorbach, and Yuri S. Kivshar. Light scattering by a finite obstacle and fano resonances. *Phys. Rev. Lett.*, 100:043903, Jan 2008.

[202] Wenyu Zhao and Yongyuan Jiang. Experimental demonstration of sharp fano resonance within binary gold nanodisk array through lattice coupling effects. *Opt. Lett.*, 40(1):93–96, Jan 2015.

[203] Kensuke Kobayashi, Hisashi Aikawa, Akira Sano, Shingo Katsumoto, and Yasuhiro Iye. Fano resonance in a quantum wire with a side-coupled quantum dot. *Phys. Rev. B*, 70:035319, Jul 2004.

[204] A. C. Johnson, C. M. Marcus, M. P. Hanson, and A. C. Gossard. Coulomb-modified fano resonance in a one-lead quantum dot. *Phys. Rev. Lett.*, 93:106803, Sep 2004.

[205] Masatomi Iizawa, Satoshi Kosugi, Fumihiro Koike, and Yoshiro Azuma. The quantum and classical fano parameter q. *Physica Scripta*, 96(5):055401, feb 2021.

[206] Gan Zhai, Yizhou Xin, Cameron J. Kopas, Ella Lachman, Mark Field, Josh Y. Mutus, Katarina Cicak, José Aumentado, Zuhawn Sung, and W. P. Halperin. Contactless excitation of acoustic resonance in insulating wafers. *Applied Physics Letters*, 121(14):142201, 2022.

[207] K. J. Satzinger, C. R. Conner, A. Bienfait, H.-S. Chang, Ming-Han Chou, A. Y. Cleland, É. Dumur, J. Grebel, G. A. Peairs, R. G. Povey, S. J. Whiteley, Y. P. Zhong,

D. D. Awschalom, D. I. Schuster, and A. N. Cleland. Simple non-galvanic flip-chip integration method for hybrid quantum systems. *Applied Physics Letters*, 114(17):173501, 2019.

[208] Taekwan Yoon, David Mason, Vijay Jain, Yiwen Chu, Prashanta Kharel, William H. Renninger, Liam Collins, Luigi Frunzio, Robert J. Schoelkopf, and Peter T. Rakich. Simultaneous brillouin and piezoelectric coupling to a high-frequency bulk acoustic resonator. *Optica*, 10(1):110–117, Jan 2023.

[209] Wayne Crump, Alpo Välimaa, and Mika A. Sillanpää. Coupling high-overtone bulk acoustic wave resonators via superconducting qubits, 2023.

[210] Shahrokh Ahmadi, Farid Hassani, Can E. Korman, Mohammad Ziaur Rahaman, and Mona E. Zaghloul. Characterization of multi- and single-layer structure saw sensor [gas sensor]. *Proceedings of IEEE Sensors, 2004.*, pages 1129–1132 vol.3, 2004.

[211] Vincent Laude, Mikaël Wilm, Sarah Benchabane, and Abdelkrim Khelif. Full band gap for surface acoustic waves in a piezoelectric phononic crystal. *Phys. Rev. E*, 71:036607, Mar 2005.

[212] Abhinav Kandala, Kristan Temme, Antonio D. Córcoles, Antonio Mezzacapo, Jerry M. Chow, and Jay M. Gambetta. Error mitigation extends the computational reach of a noisy quantum processor. *Nature*, 567(7749):491–495, Mar 2019.

[213] Morten Kjaergaard, Mollie E. Schwartz, Jochen Braumüller, Philip Krantz, Joel I.-J. Wang, Simon Gustavsson, and William D. Oliver. Superconducting qubits: Current state of play. *Annual Review of Condensed Matter Physics*, 11(1):369–395, 2020.

[214] Sihao Huang, Benjamin Lienhard, Greg Calusine, Antti Vepsäläinen, Jochen Braumüller, David K. Kim, Alexander J. Melville, Bethany M. Niedzielski, Jonilyn L. Yoder, Bharath Kannan, Terry P. Orlando, Simon Gustavsson, and William D. Oliver. Microwave package design for superconducting quantum processors. *PRX Quantum*, 2:020306, Apr 2021.

[215] R. M. Lutchyn, L. I. Glazman, and A. I. Larkin. Kinetics of the superconducting charge qubit in the presence of a quasiparticle. *Phys. Rev. B*, 74:064515, Aug 2006.

[216] John M. Martinis, M. Ansmann, and J. Aumentado. Energy decay in superconducting Josephson-junction qubits from nonequilibrium quasiparticle excitations. *Phys. Rev. Lett.*, 103:097002, Aug 2009.

[217] R. Barends, J. Wenner, M. Lenander, Y. Chen, R. C. Bialczak, J. Kelly, E. Lucero, P. O'Malley, M. Mariantoni, D. Sank, H. Wang, T. C. White, Y. Yin, J. Zhao, A. N. Cleland, John M. Martinis, and J. J. A. Baselmans. Minimizing quasiparticle generation from stray infrared light in superconducting quantum circuits. *Applied Physics Letters*, 99(11):113507, 2011.

[218] Antonio D. Córcoles, Jerry M. Chow, Jay M. Gambetta, Chad Rigetti, J. R. Rozen, George A. Keefe, Mary Beth Rothwell, Mark B. Ketchen, and M. Steffen. Protecting superconducting qubits from radiation. *Applied Physics Letters*, 99(18):181906, 2011.

[219] J M Kreikebaum, A Dove, W Livingston, E Kim, and I Siddiqi. Optimization of infrared and magnetic shielding of superconducting TiN and al coplanar microwave resonators. *Superconductor Science and Technology*, 29(10):104002, aug 2016.

[220] *Surrey NanoSystems Ltd.* www.surreynanosystems.com.

[221] *Vantablack Data Sheet.* https://www.surreynanosystems.com/assets/media/vantablack-vb-a4-data-brochure-2016.pdf. Surrey NanoSystems.

[222] Arnold Adams, Fred Nicol, Steve McHugh, John Moore, Gregory Matis, and Gabriel A. Amparan. Vantablack properties in commercial thermal infrared imaging systems. In Gerald C. Holst and Keith A. Krapels, editors, *Infrared Imaging Systems: Design, Analysis, Modeling, and Testing XXX*, volume 11001, pages 329 – 339. International Society for Optics and Photonics, SPIE, 2019.

[223] Praveen K. Velpula, Daniel Kramer, Michal Ďurák, and Bedřich Rus. Femtosecond laser damage resistance of beam dump materials for high-peak power laser systems. *Optical Engineering*, 59(5):1 – 9, 2020.

[224] M. J. Persky. Review of black surfaces for space-borne infrared systems. *Review of Scientific Instruments*, 70(5):2193–2217, 1999.

[225] Alexander Shnirman, Gerd Schön, Ivar Martin, and Yuriy Makhlin. Low- and high-frequency noise from coherent two-level systems. *Phys. Rev. Lett.*, 94:127002, Apr 2005.

[226] P. V. Klimov, J. Kelly, Z. Chen, M. Neeley, A. Megrant, B. Burkett, R. Barends, K. Arya, B. Chiaro, Yu Chen, A. Dunsworth, A. Fowler, B. Foxen, C. Gidney, M. Giustina, R. Graff, T. Huang, E. Jeffrey, Erik Lucero, J. Y. Mutus, O. Naaman, C. Neill, C. Quintana, P. Roushan, Daniel Sank, A. Vainsencher, J. Wenner, T. C. White, S. Boixo, R. Babbush, V. N. Smelyanskiy, H. Neven, and John M. Martinis.

Fluctuations of energy-relaxation times in superconducting qubits. *Phys. Rev. Lett.*, 121:090502, Aug 2018.

[227] Jonathan J. Burnett, Andreas Bengtsson, Marco Scigliuzzo, David Niepce, Marina Kudra, Per Delsing, and Jonas Bylander. Decoherence benchmarking of superconducting qubits. *npj Quantum Information*, 5(1):54, Jun 2019.

[228] Steffen Schlör, Jürgen Lisenfeld, Clemens Müller, Alexander Bilmes, Andre Schneider, David P. Pappas, Alexey V. Ustinov, and Martin Weides. Correlating decoherence in transmon qubits: Low frequency noise by single fluctuators. *Phys. Rev. Lett.*, 123:190502, Nov 2019.

[229] Clemens Müller, Jürgen Lisenfeld, Alexander Shnirman, and Stefano Poletto. Interacting two-level defects as sources of fluctuating high-frequency noise in superconducting circuits. *Phys. Rev. B*, 92:035442, Jul 2015.

[230] Antti P. Vepsäläinen, Amir H. Karamlou, John L. Orrell, Akshunna S. Dogra, Ben Loer, Francisca Vasconcelos, David K. Kim, Alexander J. Melville, Bethany M. Niedzielski, Jonilyn L. Yoder, Simon Gustavsson, Joseph A. Formaggio, Brent A. VanDevender, and William D. Oliver. Impact of ionizing radiation on superconducting qubit coherence. *Nature*, 584(7822):551–556, Aug 2020.

[231] U. Vool, I. M. Pop, K. Sliwa, B. Abdo, C. Wang, T. Brecht, Y. Y. Gao, S. Shankar, M. Hatridge, G. Catelani, M. Mirrahimi, L. Frunzio, R. J. Schoelkopf, L. I. Glazman, and M. H. Devoret. Non-Poissonian quantum jumps of a fluxonium qubit due to quasiparticle excitations. *Phys. Rev. Lett.*, 113:247001, Dec 2014.